BISMUTH – BASED OXIDE SEMICONDUCTORS: MILD SYNTHESIS AND PRACTICAL APPLICATIONS

by

HARI KRISHNA TIMMAJI

Presented to the Faculty of the Graduate School of

The University of Texas at Arlington in Partial Fulfillment

of the Requirements

for the Degree of

DOCTOR OF PHILOSOPHY

THE UNIVERSITY OF TEXAS AT ARLINGTON

December 2011

ACKNOWLEDGEMENTS

With great pleasure and gratitude, I express my sincere thanks to my research advisor Professor Krishnan Rajeshwar for his continuous guidance and encouragement throughout my research work.

I extend my sincere thanks and gratitude to my committee members, Professors Purnendu (Sandy) Dasgupta, James Grover, Melanie Sattler, and Richard (Xiyun) Guan for their valuable guidance and advice.

My special thanks go to Professor Norma Tacconi for her immense patience with me, moral support, help, and valuable discussions throughout my research. I also thank all the past and present members of our research group for their contributions to my research.

I especially thank my parents Sri. Vedanta Chary and Smt. Anooradha, my sister Bindu, my brother-in-law Krishna, and my niece Laasya, for providing me their unending support and encouragement throughout my career and life. I thank Dr. Devi Majumdar, for her suggestions in writing this dissertation, her constant support, and trust in me. I also acknowledge my friends, Srinivas Prabakar and Karthik Shastry, for being great roommates and for sharing my ups and downs during my time at UTA.

Finally, I thank the Department of Earth & Environmental Sciences, and the Department of Chemistry, at University of Texas at Arlington, for giving me an opportunity to follow my dream and for extending financial support for this dissertation study.

October 17, 2011

ABSTRACT

BISMUTH – BASED OXIDE SEMICONDUCTORS: MILD SYNTHESIS AND PRACTICAL APPLICATIONS

Hari Krishna Timmaji, PhD

The University of Texas at Arlington, 2011

Supervising Professor: Krishnan Rajeshwar

In this dissertation study, bismuth based oxide semiconductors were prepared using 'mild' synthesis techniques – electrodepostion and solution combustion synthesis. Potential environmental remediation and solar energy applications of the prepared oxides were evaluated.

Bismuth vanadate ($BiVO_4$) was prepared by electrodeposition and solution combustion synthesis. A two step electrosynthesis strategy was developed and demonstrated for the first time. In the first step, a Bi film was first electrodeposited on a Pt substrate from an acidic $BiCl_3$ medium. Then, this film was anodically stripped in a medium containing hydrolyzed vanadium precursor, to generate Bi^{3+}, and subsequent $BiVO_4$ formation by in situ precipitation. The photoelectrochemical data were consistent with the in situ formation of n-type semiconductor films.

In the solution combustion synthesis procedure, $BiVO_4$ powders were prepared using bismuth nitrate pentahydrate as the bismuth precursor and either vanadium chloride or vanadium oxysulfate as the vanadium precursor. Urea, glycine, or citric acid was used as the fuel. The effect of the vanadium precursor on the photocatalytic activity of combustion synthesized $BiVO_4$ was evaluated in this study. Methyl orange was used as a probe to test the photocatalytic attributes of the combustion synthesized (CS) samples, and benchmarked against a commercial bismuth vanadate sample. The CS samples showed superior activity to the commercial benchmark sample, and samples derived from vanadium chloride were superior to vanadium oxysulfate counterparts. The photoelectrochemical properties of the various CS samples were also studied and these samples were shown to be useful both for environmental photocatalytic remediation and water photooxidation applications.

Silver bismuth tungstate ($AgBiW_2O_8$) nanoparticles were prepared for the first time by solution combustion synthesis by using silver nitrate, bismuth nitrate, sodium tungstate as precursors for Ag, Bi, and W respectively and urea as the fuel. The photocatalytic activity of these nanoparticles was superior to a sample prepared by solid-state synthesis. The combustion-synthesized particles were subsequently modified with Pt catalyst islands using a photodepostion technique and then used for the photo-generation of syngas ($CO + H_2$). Formic acid was used in these experiments for in situ generation of CO_2 and its subsequent reduction to CO. In the absence of Pt modification, H_2 was not obtained. These results were compared with those obtained with acetic acid in place of formic acid, and finally the mechanistic pathways for syngas and methane photogeneration are presented.

TABLE OF CONTENTS

LIST OF ILLUSTRATIONS

LIST OF TABLES

CHAPTER 1

INTRODUCTION

1.1 Oxide Semiconductors

Oxide semiconductors have attracted much attention in the past decades due to their various properties, which include optical, electrical, magnetic, mechanical and catalytic / photocatalytic properties, to name a few. They are attractive candidates for solar energy applications, such as photovoltaic, photoelectrochemical and photocatalytic remediation.[1,2] To select a material suitable for all the above applications is however a difficult task and no one material is ideal for more than one of the above applications.[2] Listed below are some of the desirable properties of the oxide semiconductors that determine their use in solar energy applications.[2]

- optical energy gap (favorable to have absorbance in the visible region of the solar spectrum)
- electronic properties (higher lifetime of charge carriers and effective charge separation)
- relevant positions of the conduction and valence band edges with respect to the reduction potentials of the substrate of interest
- generation of highly reducing and oxidizing species at the semiconductor / medium interface
- chemically inert and stable over wide pH range
- photochemical stability in aqueous solutions

It is difficult for any one semiconductor oxide to fulfill all the above requirements, which would make it an ideal material. The most widely studied oxide semiconductor is TiO_2, which sparked worldwide interest in these materials for solar energy applications.[2] TiO_2 has been studied for degradation of organics from air and water, bacterial disinfection, water splitting, odor control, cancer treatment, etc.[3] A major limitation of TiO_2 is its band gap value (~3.0 – 3.2 eV) which restricts its absorption in the UV region of the solar spectrum (~4% of the solar spectrum), with very little or no absorption in the visible region (~50% of the solar spectrum). Figure 1.1 shows the spectral distribution of the solar flux. Improving the activity of TiO_2 towards visible light, and/or developing other oxide semiconductors with visible light activity would enhance the pertinence of these materials towards solar energy conversion and environmental remediation applications.[2]

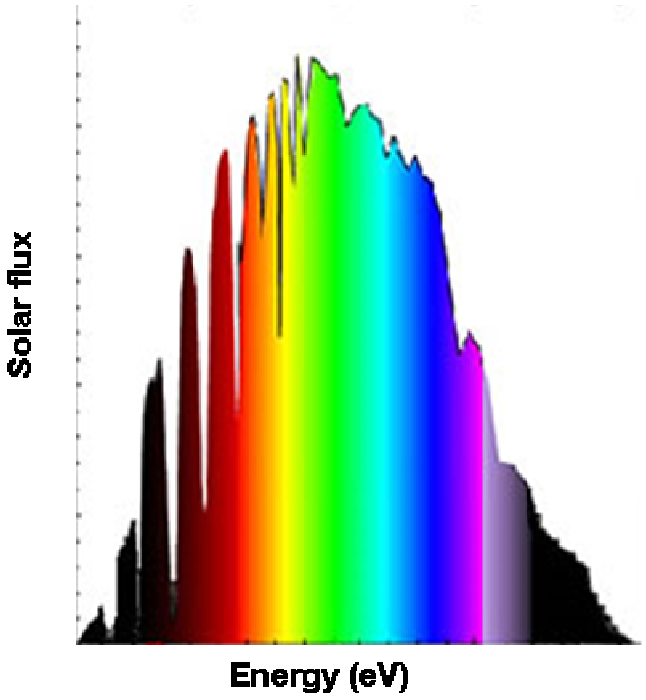

Figure 1.1 Spectral distribution of solar photon flux.[4]

Compared to other non oxide semiconductors such as gallium arsenide (GaAs), indium phosphide (InP), cadmium telluride (CdTe), cadmium selenide (CdSe) etc., the advantages of using oxide semiconductors are that their component elements are more in abundance, are non-toxic, are more stable in aqueous media, and their optical and electronic properties can be improved by doping.[2] Before proceeding further, it would be useful to consider some insights into the electronic band structure of semiconductors, the concept of band gap, and some crucial aspects of photocatalysis.

1.1.1 Electronic Band Structure of Solids

In isolated atoms, the electrons are present in specific energy levels. In solids, the atoms are compacted, due to which the orbitals are so closely spaced that they are essentially present as continuous bands, rather than individual energy levels. The filled bonding orbitals constitute the valence band (VB) and the vacant antibonding orbitals constitute the conduction band (CB). The gap between the valence and conduction bands is known as the band gap (E_g), measured in the units of electron volts. A schematic description of the electronic energy structure for solids is shown in below in Figure 1.2.[5]

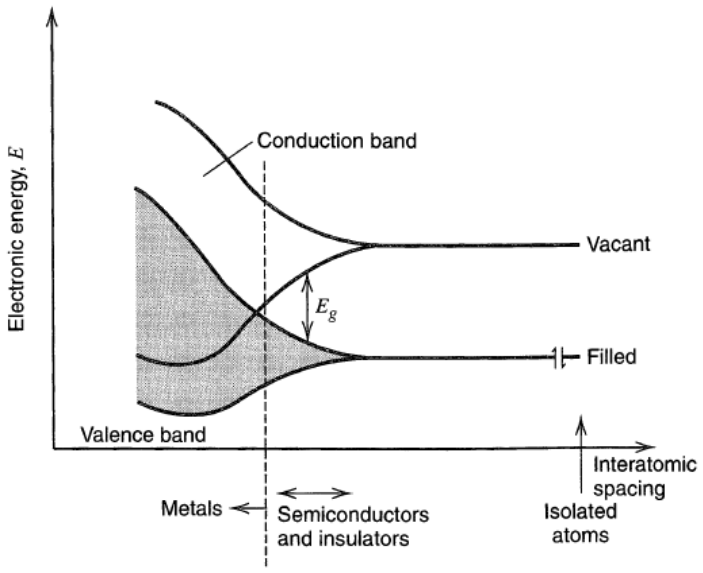

Figure 1.2 Electronic energy structure for solids.

In metals, the band gap is very small, and the valence and conduction bands are overlapping. An electron can move from one level to another with only small energy of activation. In the case of non metals or insulators, the band gap is very large and it requires large energy to move an electron from the valence band to the conduction band, which is not useful from a practical point of view.[5] In the case of semiconductors, the band gap is not too large, and excitation of the electrons by suitable energy causes them to move from the valence band to the conduction band, thereby facilitating conduction of electricity. The excitation could be caused by thermal energy or light energy.[5]

1.1.2 Photocatalysis

Photocatalysis can be defined as a catalytic process where the reaction occurs due to the electron – hole pairs (e^- – h^+) photogenerated on the surface of the semiconductor material irradiated by light of suitable energy.[3] From a thermodynamic sense, some authors differentiate between 'photocatalytic' and 'photosynthetic' reactions based on the ΔG values of the reactions. The reactions with $\Delta G < 0$ (e.g., oxidation of organic compounds) are termed as 'photocatalytic' reactions, whereas the reactions with $\Delta G > 0$ (e.g., water splitting reactions) are termed as 'photosynthetic' reactions.[1,6]

When a semiconductor is excited with photons of energy ≥ than the band gap, the electrons from the valence band move to the conduction band (e^-_{CB}), leaving a positively charged space in the valence band, which is termed as a 'hole' (h^+_{VB}). The electron – hole pairs then migrate to the surface of the semiconductor particle and can take part in subsequent redox reactions. A schematic of the photocatalysis process is shown in Figure 1.3 below.

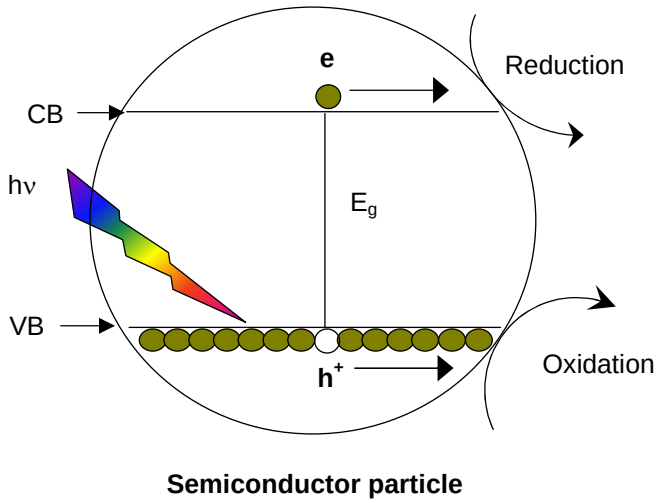

Figure 1.3 Schematic diagram of photocatalysis on the semiconductor particle.

The photogenerated charge carriers can undergo (i) recombination in the bulk of the semiconductor or through trap sites on the surface, and release heat and/or luminescence (ii) charge transfer by reacting with electron acceptor or donor species and resulting in subsequent redox reactions.[1,3,6] Figure 1.4 is a schematic of the different recombination and charge transfer processes on the semiconductor particle.

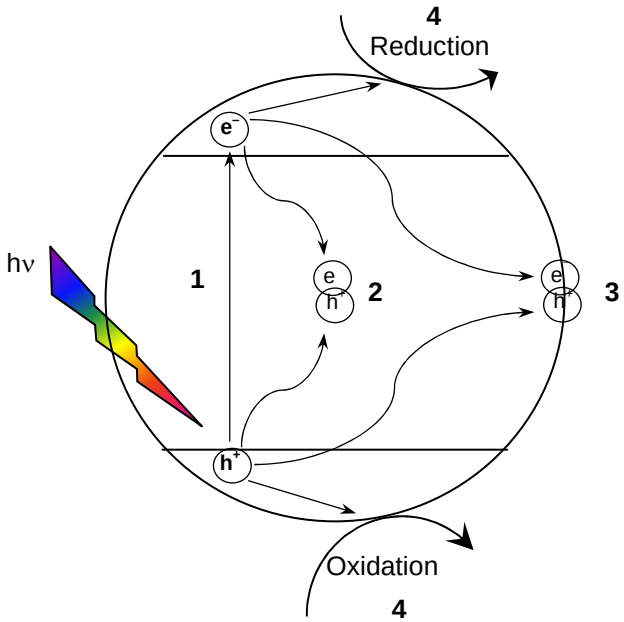

Figure 1.4 Schematic representation of the recombination and redox processes on the semiconductor particle. 1 = charge carrier generation; 2 = bulk recombination; 3 = surface recombination; 4 = charge transfer.

The photocatalytic efficiency depends on the number of charge carriers taking part in the reaction, and on the effective separation of the photogenerated electron – hole pairs. The equations given below describe the photocatalysis reaction mechanism occurring on a semiconductor particle.[6]

Charge carrier generation

$$SC + h\nu \rightarrow h^{+}_{vb} + e^{-}_{cb} \qquad (1.1)$$

Charge carrier trapping

$$h^+_{vb} + SC\text{-}OH \rightarrow SC\text{-}OH^{\bullet+} \quad (1.2)$$

$$e^-_{cb} + SC - OH \rightarrow SC - OH / e^-_{tr} \quad (1.3)$$

Bulk recombination

$$h^+_{vb} + e^-_{cb} \rightarrow SC + heat \quad (1.4)$$

Surface recombination

$$e^-_{cb} + SC - OH^{\bullet+} \rightarrow SC - OH \quad (1.5)$$

$$h^+_{vb} + SC - OH / e^-_{tr} \rightarrow SC - OH \quad (1.6)$$

Charge transfer

$$SC - OH^{\bullet+} + \mathrm{Re}\, d \rightarrow SC - OH + \mathrm{Re}\, d^{\bullet+} \quad (1.7)$$

$$SC - OH / e^-_{tr} + Ox \rightarrow SC - OH + Ox^{\bullet-} \quad (1.8)$$

where SC represents the semiconductor, e^-_{cb} is the photogenerated conduction band electron, h^+_{vb} is the photogenerated valence band hole, *SC–OH*$^{\bullet+}$ is the surface trapped hole, (surface bound hydroxyl radical), *SC–OH/* e^-_{tr} is the surface trapped electron, *Red* is an electron donor, *Ox* is an electron acceptor.[6]

Another important aspect in the photocatalysis process is the position of the conduction and valence band edges of the semiconductor with respect to the reduction potentials of the substrate of interest. Charge transfer occurs when the redox potential of the electron acceptor species is more positive than the conduction band edge of the semiconductor, and the redox potential of the electron donor species is more negative than the valence band edge.[1,3,6] Figure 1.5 shows the band edge positions of some semiconductors in relation to the redox potentials for water splitting.[7]

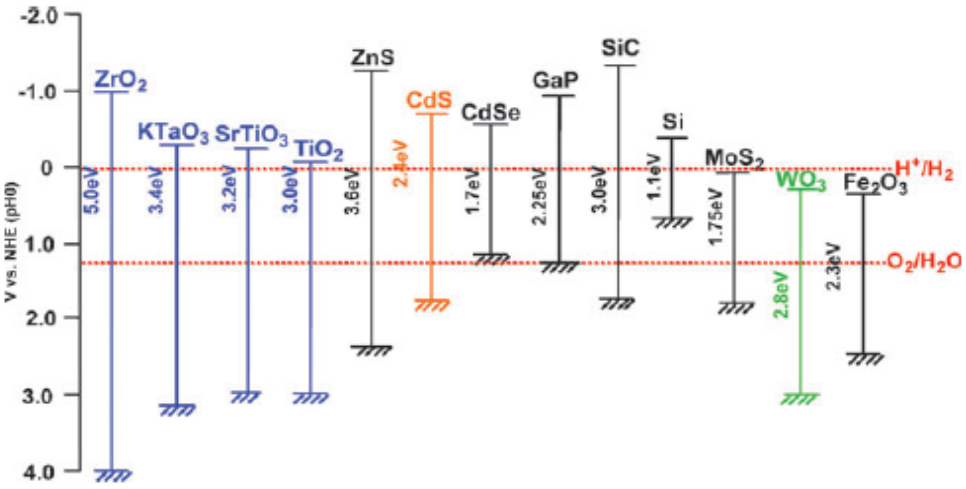

Figure 1.5 Band edge positions of semiconductors.

From the above discussion, we can observe that there are a variety of semiconductor materials which have potential for photocatalytic applications.

Other factors which influence the photocatalytic performance of the semiconductors are surface area and particle size. In particles with larger surface area and smaller size (nanosize), the charge carriers can reach the surface faster and with relative ease compared to larger size particles, thereby reducing the recombination rate and enhancing the photoactivity.

1.2 Energy Payback Time and Mild Synthesis of Inorganic Semiconductors

Oxide semiconductors are generally prepared by high temperature processes (e.g. solid state reactions), which in addition to requiring high temperatures for synthesis, are also time consuming. In this processes the energy payback time is very long. Energy payback time is defined as the time required to recover the energy used to prepare a material.[2] Since the solid state routes of synthesis require high temperatures and long reaction times, the energy input is significantly higher for these processes. This has resulted in developing 'mild' synthesis (low temperature) routes to prepare the materials, some of which include sol–gel, sonochemical, chemical bath deposition and electrochemical methods.

Methods such as sol–gel and chemical bath deposition normally involve the initial preparation of a precursor gel, and subsequent decomposition of the precursor gel at elevated temperatures to form the oxide.[8] These techniques require low temperatures of preparation, result in better mixing of the reactants as the reactants are in liquid / colloidal states, result in better purity of the products, and can be carried out under ambient conditions. Since the methods can be used under low temperature and ambient conditions, the energy input for these processes is significantly reduced when compared to solid state ceramic routes of synthesis, which require high temperatures and long reaction times.

As with any preparation technique, product morphology and formation depends on factors such as pH, temperature, solution composition and concentration. By controlling these factors, products of desired morphology can be obtained.

However, some of the drawbacks of these processes include high raw material cost, use of organic solutions, requirement of additional calcination steps for solvent removal and improving product crystallinity, long processing times, particle agglomeration, careful control of the process parameters, etc. Though the energy input is significantly lower, longer reaction times are still required for product formation.

In this respect, combustion synthesis process is a time – and energy – efficient process of preparing nanomaterials. This study focuses on preparing oxide semiconductors using 'mild' synthesis routes, namely electrodeposition and combustion synthesis. A brief background on these techniques is described in the following sections.

1.3 Electrodeposition of Inorganic Oxide Semiconductors

Electrodeposition or electrochemical deposition is a relatively inexpensive and simple technology with well known industrial range applications for metal and metal alloy deposition, which range from large area surface treatments (i.e. zinc electroplating) to most advanced electronic industries (copper deposition on chips, magnetic heads, etc.).[9] The low cost, relatively low temperature, soft processing and comparatively low material demand make this technology

attractive in terms of commercialization. Beginning with Si,[9] a variety of non oxide (group III–V, II–IV compounds) and oxide semiconductors (oxides of Ni, Cu, Zn, Fe, Mn, Ti, W etc) have been prepared by electrodeposition with applications extending to transistors, piezoelectric devices, gas sensors, electrocatalysis, solar water splitting, environmental remediation etc.[10] In addition to the binary oxides, mixed oxides and metal/oxide nanocomposites have also been prepared using this technique.[10]

The basic technique involves an electrolysis step wherein a substance from a solution is deposited onto the surface of an electrode under the influence of an electric field. When an electric current is passed between two or more electrodes separated in an electrolyte solution, film deposition occurs at the electrode – electrolyte interface (known as the electrical double layer), which has a high potential gradient of around 10^5 V/cm.[11]

Electrodeposition can be achieved under galvanostatic (current controlled) or potentiostatic (potential controlled) modes. The precursors are mostly in the solution (dissolved form) and the process can be both cathodic and anodic. In cathodic electrodeposition, the metal is deposited at the cathode by passing current in a solution of a metal salt via reduction of a dissolved metal ion followed by dehydration of the initially deposited hydroxide. Anodic electrodeposition involves the oxidation of a metal or a transition metal cation (in solution form) followed by its chemical reaction with water to form the corresponding oxide layer on the electrode surface. [10,11]

A basic electrodeposition setup contains the following

(i) Working electrode (WE): the substrate for the film to be formed

(ii) Counter electrode (CE): an inert material (Pt or Au) which helps in film synthesis

(iii) Reference electrode (RE): to measure the potential of the WE

(iv) Electrolyte solution (bath solution): contains the supporting electrolyte, the electroactive species, and any additives.

Some of the advantages of electrodeposition are [11]

(i) It is a low temperature technique limited by the boiling point of the electrolyte. Higher deposition conditions can be carried out using molten salt electrolytes.

(ii) It is basically a reduction/oxidation reaction wherein the reducing or oxidizing power can be varied and selected by fine tuning of the cell potential (or current).

(iii) Variation in the bath composition can lead to changes in the film composition.

(iv) Experiments are simple to perform, and high quality products can be obtained at low cost.

However, the process also suffers from some disadvantages, which are outlined below[11]

(i) The process can be performed only on conducting substrates.

(ii) Since the experiments are carried out under ambient conditions, the products are often amorphous and poorly ordered, making structural determination difficult. An additional annealing step needs to be done to improve crystallinity and achieve better stoichiometry.

The product composition, morphology spatial orientation can be tuned by controlling the growth parameters such as pH, solution bath composition, current density, potential, temperature, annealing conditions, etc., By fine tuning the desired conditions, nanostructures of oxides can be formed in the desired growth direction. In addition, dopants can also be incorporated into the host oxide matrix, which reduces the band gap of the semiconductors. This is particularly useful in the case of semiconductors with applications in photovoltaic and solar photocatalytic devices, where it is possible to enhance the visible light activity of t hese materials by doping. With the advances and improvements in the ability to control the deposition process at an atomic scale, and the ability to demonstrate epitaxial growth in some cases, there has been a great deal of progress in electrodeposition techniques.[10]

The nature of the solvent also affects the size and composition of the materials prepared. Any solvent with an electrochemical window exceeding that of the dissolved species would be suitable for experiments. In other words, the dissolved species should be more easily oxidized or

reduced than the solvent used. Aqueous solvents have limitations in these aspects as they have relatively narrow electrochemical windows in which to operate. Tendency to liberate H_2 molecule during electrolysis, low thermal stability, evaporation are some other limitations of aqueous solvents.[12] These limitations can be overcome by using of non-aqueous electrolytes (molten salts and ionic liquids). The advantages of non-aqueous electrolytes include non-volatility, non-flammablity in most cases, less toxicity, good solvents for both organic and inorganic materials, use over a wide temperature range, and in addition exhibit good electrical conductivity and have wide electrochemical windows. These aspects are making the use of non-aqueous electrolytes increasingly important. [12]

The ability for preparing a wide range of materials with this technique, combined with the excellent photoelectrochemical and photocatalytic properties of $BiVO_4$ prompted us to study the feasibility of preparing $BiVO_4$ photoelectrodes by electrochemical deposition. A two step procedure electrosynthesis strategy for preparing $BiVO_4$ electrodes on a Pt substrate was developed and demonstrated in the current work. To the best of our knowledge, this was the first report on the two step electrosynthesis strategy for preparing $BiVO_4$. The $BiVO_4$ films were investigated for water photooxidation studies. The aim of this technique was to develop a simple, proof-of-concept study for preparing oxide semiconductors for potential photoelectrochemical applications.

Before discussing further on the preparation of the oxide semiconductors, let us briefly consider some important photoelectrochemical concepts of semiconductors.

1.3.1 Photoelectrochemical Concepts[5]

When an electrode is irradiated with light of suitable energy, it absorbs the light and results in the production of a current (photocurrent). This property of electrodes is the basis of photoelectrochemical measurements. Information about the nature of the electrode–solution interface, the energetics and kinetics of the process can be obtained from studying the dependence of the photocurrent on wavelength, solution composition, electrode potential etc.

Practical applications of photoelectrochemical processes include studying the efficiency of conversion of light energy to electrical and chemical energy.

As mentioned earlier, the electronic properties of solids can be explained in terms of the band model, wherein the closely spaced molecular orbitals are described as forming continuous bands comprising of the filled valence band (VB) and the empty conduction band (CB). The gap between the conduction and the valence band is the band gap, measured in units of electron volts.

Excitation (thermal or photo induced) of electrons from VB to CB causes the conduction of current. With semiconductors with a large band gap, excitation alone is not sufficient to move the electrons to the CB. In such cases, substituting donor or acceptor atoms (dopants) into the semiconductor lattice can be done to induce conduction. The dopant atoms create a new energy level in the band gap, depending on the characteristics of the dopant. If a donor atom is substituted into the lattice, a new level is formed just below the CB level, and the material is an *n* – type semiconductor, with the CB electrons contributing majorly to the electrical conductivity of the material. In the case of an acceptor atom substitution, the new level is formed just above the VB, and the material is a *p* – type semiconductor, with the VB holes being the majority current carriers. Figure 1.6 shows a schematic of the two types of semiconductors.

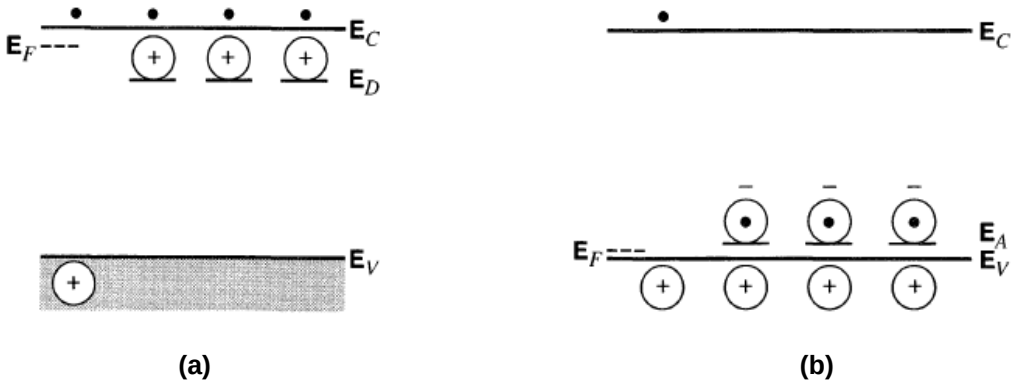

Figure 1.6 Representation of (a) *n* – type and (b) *p* – type semiconductors.
E_C is the conduction band energy level, E_V is the valence band energy level, E_F is the Fermi level of the semiconductor, E_D and E_A are the energy levels created by the donor and acceptor dopants, respectively.

An important concept in semiconductor electrodes is the Fermi level (E_F), which is defined as the energy where the probability of a level being occupied by an electron (at 0 K) is ½. For an intrinsic semiconductor, E_F is approximately in between the VB and CB. In a doped semiconductor, the location of E_F depends on the doping level. For *n* – type semiconductors, E_F lies slightly below the CB, whereas for *p* – type semiconductors, E_F lies slightly above the VB.

What happens at the semiconductor / electrolyte interface when the semiconductor is in contact with the solution? When a semiconductor is in contact with the solution, the electrochemical potential of the two phases must be the same to attain electrostatic equilibrium (their Fermi levels must be equal). The electrochemical potential of the solution phase depends on the redox potential of the solution, and that of the semiconductor depends on its E_F. Equilibrium is attained by charge transfer between the phases. In the case of an *n* – type semiconductor, E_F of the semiconductor is above that in the solution, and electrons flow from the semiconductor to the solution. The excess charge does not reside at the electrode surface, but extends into the electrode in a region known as *space-charge region.* The resulting electric field in this region affects the electrochemical potential of the electrons.

For an *n* – type semiconductor, the *space-charge region* comprises of positive charges due to depletion of electrons (depletion layer). Only the band energies in this region are different from the energies in the bulk of the semiconductor, whereas the band positions remain the same. Due to the positive charge in the space-charge region, the band edges are bent upwards (band bending) due to the energy difference between the space-charge region and the bulk of the semiconductor. In the case of a *p* – type semiconductor, the *space-charge region* consists of excess negative charge and the bands are bent downwards. (Figure 1.7)

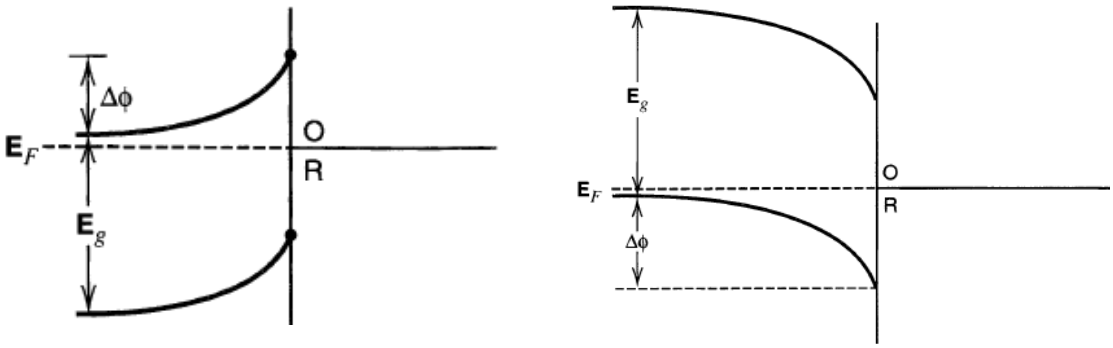

(a) **(b)**

Figure 1.7 Band bending for (a) *n* – type and (b) *p* – type semiconductors in an electrolyte solution.

Excess electrons in the space-charge region move towards the bulk of the semiconductor, and excess holes move towards the interface. The potential at which no excess charge exists in the semiconductor is the point of zero charge (E_Z), also known as flat band potential (E_{fb}), since the bands are not bent due to the absence of electric field and space-charge regions.

Applying a potential to a semiconductor electrode affects the charge transfer ability across the interface. When the potential is more negative than E_{fb} (for *n* – type), electrons accumulate at the semiconductor surface (accumulation layer). Then, the semiconductor behaves like a metal electrode.

When a *n* – type semiconductor in a solution is irradiated with light of energy greater than E_g photons are absorbed and electron – hole pairs are created. Electron – hole pairs in the bulk of the semiconductor recombine with evolution of heat. Those present in the space-charge region are separated and result in current generation. The electrons move from the semiconductor to the external circuit, while the holes move to the surface and oxidize the species in solution, resulting in photo-oxidations, and generating *photoanodic* current. An illustration of this phenomenon is explained in Figure 1.8 below.

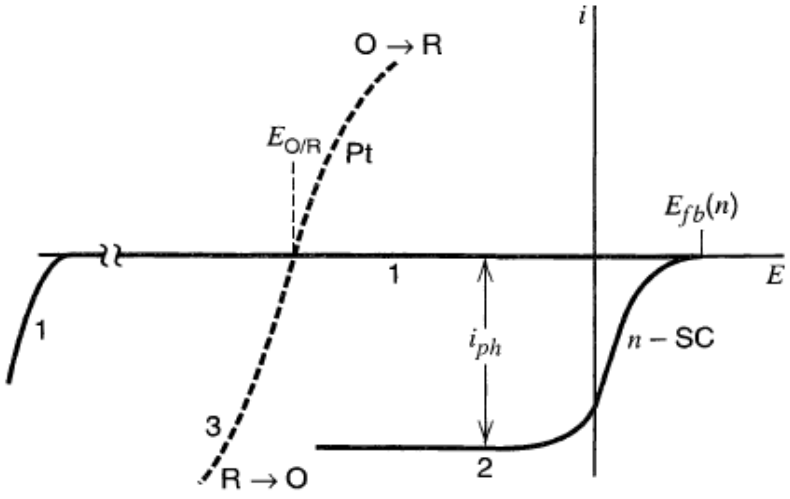

Figure 1.8 Current-potential curves for a solution containing couple O/R. for an *n*-type semiconductor in the dark (**1**) and under irradiation (**2**). The dotted line (**3**) is the *i-E* curve at a platinum electrode

In the dark, there is no current flow at potentials more positive than E_{fb} due to the absence of holes in the semiconductor to accept electrons from the reduced species with redox potential in the band gap region (curve 1). Under irradiation, there is flow of current (photoanodic current) as long as the potential of the electrode is more positive than E_{fb} (curve 2). The photo-oxidation occurs at less positive potentials than that required for an inert metal electrode (curve 3) since light irradiation assists the oxidation process. Similarly, irradiation of a *p* – type semiconductor results in a *photocathodic* current flow and promotes photo-reduction reactions.

Another method of synthesis of oxide semiconductors used in the current work was combustion synthesis, which is described in the following section.

1.4 Combustion Synthesis of Oxide Semiconductors

Combustion synthesis (CS) is a time- and energy- efficient process, also called as self propagating high temperature synthesis (SHS). The method was pioneered by Merzhanov, a Russian scientist, and has been used to prepare a variety of technologically useful oxide and non oxide materials such as refractories, dielectrics, sensors, semiconductors, phosphors, etc.[13]

Traditionally used in the preparation of ceramics, the ease and simplicity of the method has made it an important technique for preparing nanomaterials with applications in microtechnology, biotechnology, surface coatings, energy, and environment.[2,13,14]

In a typical combustion synthesis reaction, stoichiometric amounts of a precursor and an organic fuel are mixed, ignited, and brought to combustion. The advantage of the method is that once the exothermic reaction mixture is ignited by an external source, a rapid, self- sustaining, high temperature reaction wave propagates through the reaction mixture resulting in the formation of the final products.[14,15]. Typical ignition times for the process are of the order of a few seconds, and the reaction velocities range from 0.1 to 10 cm/s. Very high temperatures (> 1000° C) are reached within a few seconds.[15] Figure 1.9 below shows a representative temperature – time profile for a CS reaction. [16]

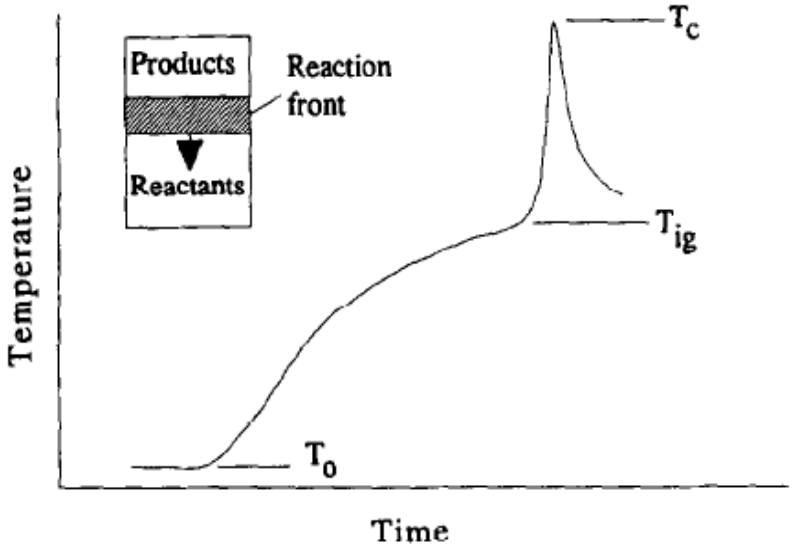

Figure 1.9 Schematic representation of the temperature – time profile in a CS reaction. T_C is the combustion temperature (maximum temperature), T_{ig} is the ignition temperature, T_O is the onset temperature of the combustion reaction.

The exothermicity of the reaction is used by the reactants to form products, making the process self-sustaining. No further energy input is required once the reaction mixture is ignited.

This property of reaching very high reaction temperatures within very short times makes the process both time– and energy– efficient.

The conventional SHS technique is also known as solid state SHS. In this process, the initial reaction mixture is in the form a powder pellet, which is ignited by an external source. Since the reaction mixture is in solid form, and due to the high reaction temperatures occurring within a short period of time, it is difficult to synthesize nanosized particles with a high surface area using this method. The typical range of the product size obtained by this method is in the order of 10 – 100µm.[15] A variety of refractory compounds like borides, silicides, nitrides and carbides are synthesized by this technique.[14,15,17]

An improvement in the conventional SHS process is known as the solution combustion synthesis (SCS). In this process variant, the initial reaction mixture is in the form of a solution containing stoichiometric ratios of the oxidizer and fuel, which is uniformly heated by an external source.[15] Since the reaction mixture is in liquid phase, this technique enables the reactants to mix at a molecular level, resulting in nanosized product particles with uniform composition.[15] The reaction proceeds with the evolution of large amount of gases, which inhibit the sintering of the product and favor formation of nanosized particles.[14,15] The SCS reaction is classified into volume combustion mode or self propagating mode, depending on the chemical nature of the reaction mixture and the process conditions. The high reaction temperatures result in pure and crystalline products.[14] Depending on the nature of the fuel, the combustion reaction is either smoldering, flaming or explosive,[13,14] enabling the synthesis of nanosized compounds of desired morphology.[14] This process has been used to prepare a variety of compounds ranging from ceramics, binary and complex oxides, perovskites, etc., in addition to refractory compounds.[17] Doping of trace amounts of rare earth metals can also be achieved in compounds synthesized by SCS.[14]

The characteristics of the combustion synthesis process outlined above make it an effective technique for synthesis of oxide nanoparticulate materials. An example of the CS reaction is given below using glycine as fuel.[15]

$$M_x(NO_3)_x + \left(\frac{5}{9}x\Phi\right)CH_2NH_2COOH + \frac{5}{4}x(\Phi-1)O_2 \rightarrow M_xO_{x/2}(s) + \frac{10}{9}x\Phi CO_2(g) + \frac{25}{18}\Phi H_2O(g) + x\left(\frac{\frac{5}{9}\Phi+1}{2}\right)N_2(g)$$

An important step in the CS reactions is the calculation of the stoichiometric ratio, known as the oxidizer to fuel (O/F) ratio, or the equivalence ratio, denoted by Φ. Due to the high exothermic nature of the reaction, concepts from propellant chemistry are used to study the nature of the reactions, and to calculate the O/F ratio. The ratio is expressed in the equation below.[18]

$$\Phi = \frac{\Sigma \text{Coefficients of oxidizing elements} \times \text{Valency}}{(-1)\Sigma \text{Coefficients of reducing elements} \times \text{Valency}} \quad (1.9)$$

The mixture is stoichiometric when Φ = 1, fuel lean when Φ < 1 and fuel rich when Φ > 1. Maximum energy is released when Φ = 1, which is the ideal case for combustion. In calculating the Φ values, the valencies of the elements are considered as follows: C has a valency of +4, H has a valency of +1, the metal cations M^{2+}, M^{3+}, M^{4+}, have valencies of +2, +3 and +4, respectively. Oxygen has an oxidizing valency of −2, and nitrogen is considered to have zero valency.[18] The ratio Φ = 1 was used for preparing the compounds throughout our study.

1.5 Oxide Semiconductors and Photocatalysis

Considering the advantages of the 'mild' synthesis methods – electrodeposition and combustion synthesis, the present study focused on preparing bismuth vanadate ($BiVO_4$) and silver bismuth tungstate ($AgBiW_2O_8$) by solution combustion synthesis. In addition, $BiVO_4$ was also prepared using a two step electrosynthesis technique. These oxide semiconductors were further characterized and tested for their photocatalytic activity under visible light irradiation.

1.5.1 Bismuth Vanadate ($BiVO_4$)

Bismuth vanadate ($BiVO_4$) is interesting from a variety of perspectives, including its ferroelastic behavior, acousto–optical and ion conductive properties. Yellow pigments based on $BiVO_4$ are also environmentally–attractive "green" substitutes for lead, chromium, and cadmium

based paints especially from an ecotoxicological perspective and high performance (good gloss and hiding power).[19] $BiVO_4$ has been extensively studied, especially over the past decade, for its visible light photoactivity and water splitting applications, and has been shown to degrade organic pollutants and photogenerate O_2 by splitting water. The most relevant aspects of $BiVO_4$ to the current research work are its excellent photoelectrochemical and photocatalytic properties for applications in solar water splitting [20] and environmental remediation.[21]

Bismuth vanadate exists in three polymorphic forms, monoclinic phase (distorted scheelite, clinobisvanite), tetragonal phase (tetragonal scheelite, dreyerite) and orthorhombic phase (tetragonal zircon, pucherite).[22,23] The orthorhombic phase occurs naturally as the pucherite mineral. The tetragonal zircon – type structure can be formed by low temperature laboratory synthesis, while high temperature synthesis produces the monoclinic form. The monoclinic form undergoes a reversible transition to the tetragonal scheelite form on heating above 255℃. The tetragonal form also transforms irreversibly to the monoclinic form on mechanical treatment (e.g., grinding with an agate mortar and pestle).[24]

Among the three polymorphs, monoclinic $BiVO_4$ is known to exhibit the best photocatalytic activity under visible light irradiation. The reason for this is explained from the electronic band structure of $BiVO_4$. Generally, the valence bands in metal oxides are derived from O 2p orbitals, and the conduction bands derived from the metal s or d orbitals. In monoclinic $BiVO_4$, the valence band comprises of hybrid Bi 6s and O 2p orbitals, which causes an upward dispersion of the valence band at the zone boundary.[25] However, a direct energy band gap is maintained and the conduction band minimum is lowered due to coupling between V 3d, O 2p and Bi 6p. Symmetric electron and hole masses result from these interactions, which facilitate efficient charge carrier separation.[25]

Figure 1.10 depicts the unit cell structure of monoclinic $BiVO_4$. The basic unit structure of monoclinic $BiVO_4$ consists of a VO_4 tetrahedron and a BiO_8 polyhedron. Four oxygen atoms surround the V site, and eight oxygen atoms surround the Bi site.[25] The VO_4 tetrahedron is connected to the BiO_8 by sharing an apex oxygen atom. The Bi and the V atoms are arranged

alternately along the crystallographic axis, making monoclinic $BiVO_4$ exhibit the characteristics of a layered structure. [25]

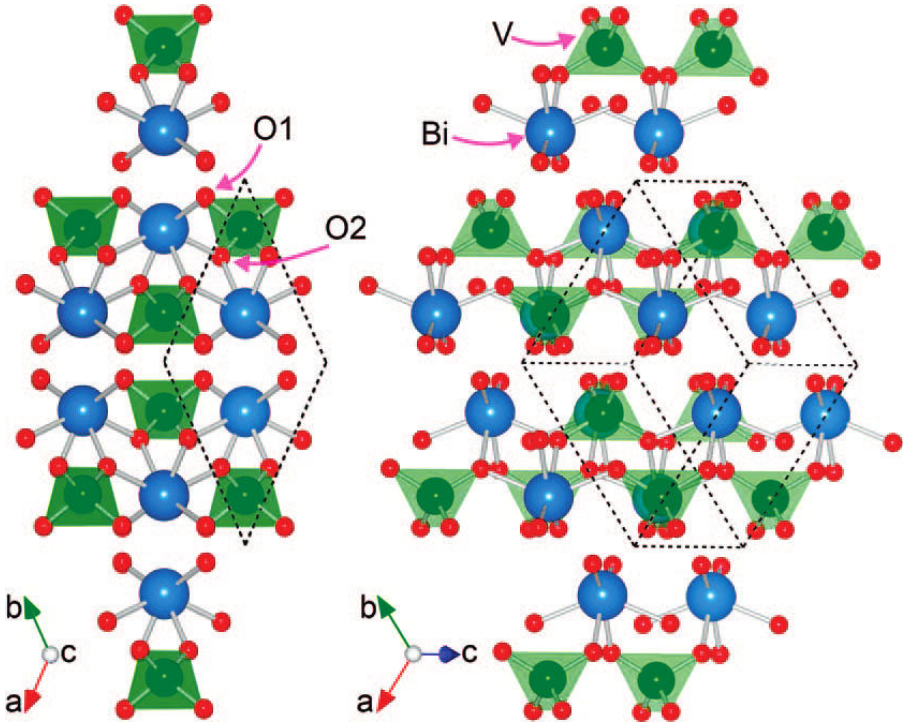

Figure 1.10 Crystal structure of $BiVO_4$.
Dashed black lines indicate the base centered monoclinic primitive cell.
Color notation; blue = bismuth; red = oxygen; green = vanadium tetrahedra.

Four types of bond lengths are present for the Bi – O bond, and two types for V – O bond, and are shown in table 1.1.[26] The different types of bond lengths indicate that both the VO_4 and BiO_8 polyhedra are slightly distorted. [26] This distortion enhances the lone pair impact of the Bi 6s states, and disperses the VB upwards resulting in a reduced band gap. As a result, the electrons can be excited by visible light. The band structure diagram is shown in Figure 1.11.[27]

Table 1.1 Bond lengths of $BiVO_4$

Crystal system	Bond length (Å)	
	Bi – O	V – O
Monoclinic	2.354 × 2	1.69 × 2
	2.372 × 2	1.77 × 2
	2.516 × 2	
	2.628 × 2	1.72 × 4
Tetragonal	2.453 × 2	
	2.499 × 2	

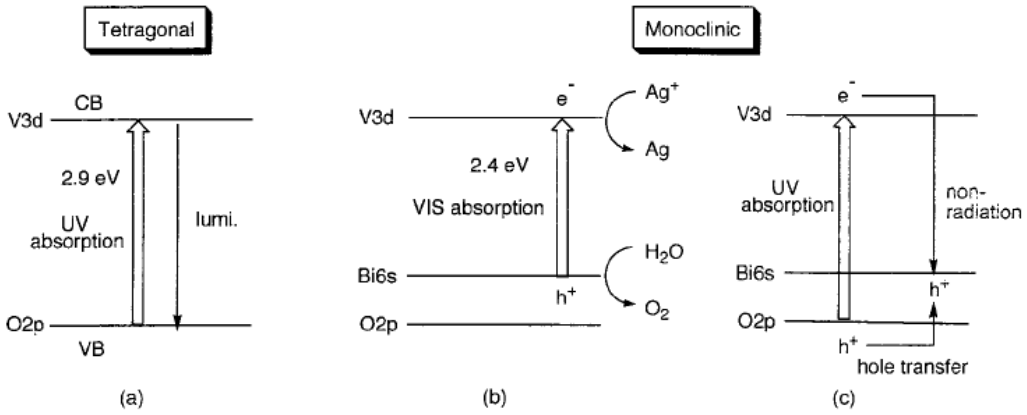

Figure 1.11 Band structures of $BiVO_4$.

In view of the band structure, extensive studies have been carried out on $BiVO_4$ for its visible light photoactivity, especially in the last decade, and a wide range of methods have been developed for preparing it.[24-71] These methods include solution co-precipitation,[28] solid-state calcinations,[28] various solution-phase preparation strategies,[27] hydrothermal synthesis (with or without surfactant),[31] metallo-organic deposition,[41] sol–gel synthesis,[34] flame pyrolysis,[49] sonochemical/ultrasound-assisted procedures,[37] and electrodeposition.[71] Composites of $BiVO_4$ also have been prepared with V_2O_5,[72] WO_3,[52] polyaniline,[61] and carbon.[73]

The current research examined the influence of vanadium precursors on the photocatalytic attributes of $BiVO_4$. One major finding from these studies was that the

photocatalytic activity depended on the choice of precursor. There are other published reports on the combustion synthesis of $BiVO_4$[48,74] or its composites.[72] The present study differs from these published reports in some specific important attributes. For example, in the present study, the Φ ratio was maintained at unity, in comparison to a prior study where the Φ ratio was varied (>1)[48]. This study shows for the first time that use of vanadium chloride (instead of oxysulfate) affords better-quality $BiVO_4$ samples, which is corroborated by the thermal analysis data.[75]

1.5.2 Silver Bismuth Tungstate ($AgBiW_2O_8$)

As mentioned earlier in section 1.1, it is difficult to select an *ideal* semiconductor oxide material for fulfilling both the energy and environment applications. Research aimed at developing oxide semiconductors for the above applications has increased tremendously within the past decades, and new ternary and quaternary complex oxides have emerged for their photocatalytic ability. One such group of complex oxides belonging to the $ABi(MO_4)_2$ system, (where A = Na, Ag; and M = Mo, W), have been studied for their promising photocatalytic activity for organic degradation and H_2 generation. [76-78] Compounds composed of both Ag^+ and Bi^{3+} ions exhibited band gap narrowing, which was attributed to a synergetic effect of the Ag^+ and Bi^{3+} ions and a hybrid valence band formed from Ag 4d, Bi 6s and O 2p orbitals.[79,80]

Particularly among these oxides, there are very few studies on the preparation and photocatalytic attributes of $AgBiW_2O_8$. In one study, the compound was prepared by a high-temperature (973 K for 18 h) solid state reaction from the corresponding metal oxide mixture and studied for its photocatalytic ability to generate H_2 from an aqueous solution of CH_3OH.[76] Of the three related oxides ($Bi_2W_2O_9$, Ag_2WO_4, and $AgBiW_2O_8$) examined in this study, $AgBiW_2O_8$ exhibited the highest photo-activity for H_2 evolution.[76] This is the only study we are aware of where Ag and Bi are present intrinsic (in a single phase) in the compound. More recently, molybdates belonging to the class to the class $ABi(MoO_4)_2$ (A = Na, Ag) and tungstates belonging to the class $ABi(WO_4)_2$ (A = Na) have been studied for the effect of chemical composition and electronic structure on the photodegradation of 2 – propanol.[77,78] Other studies on Ag based oxides have focused on preparing Bi_2WO_6 'superstructures' and then modifying the structure with

Ag by using a deposition precipitation procedure,[81] or preparing other oxides of Ag ($AgAlO_2$, $AgCrO_2$, and Ag_2CrO_4)[82] and correlating the effect of crystal structure and electronic properties on their photocatalytic properties.

Previous researchers have identified a monoclinic scheelite structure with space group *I 2/m* (No 12) for this compound.[76] Based on the density of states (DOS) studies, it was speculated that the conduction band of $AgBiW_2O_8$ comprised of Bi 6s, Ag 4d and O 2p orbitals. The study compared three oxides Ag_2WO_4, $Bi_2W_2O_9$ and $AgBiW_2O_8$ and, it was speculated that the conduction band bottom in $AgBiW_2O_8$ is more raised, due to the hybridization and the effect of the weaker crystal field surrounding the W atoms. In addition, it was also shown that the valence band shifted upwards due to hybridization of the Bi 6s, Ag 4d and O 2p orbitals. A schematic of the band structures of the different W based oxides is shown below in Figure 1.12.[76]

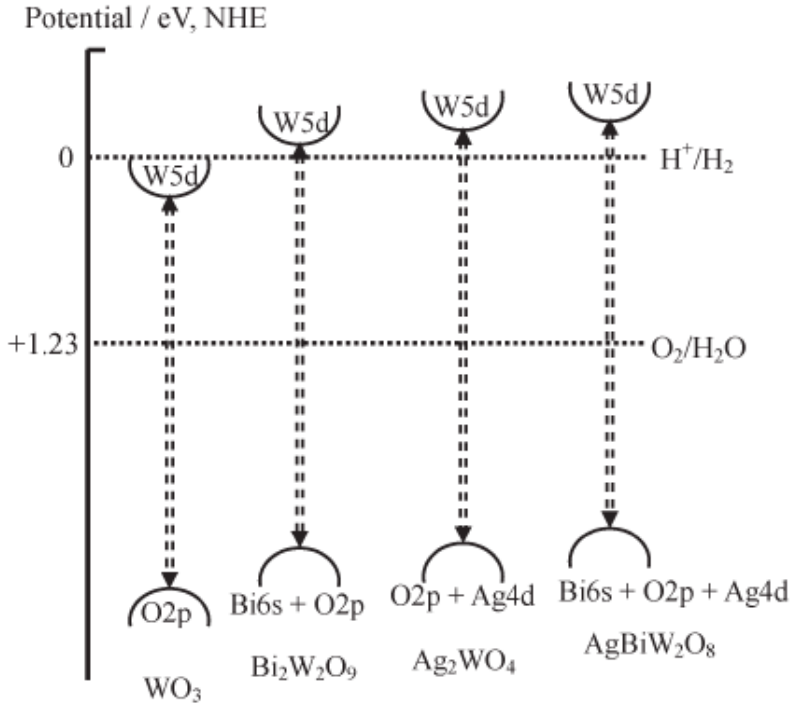

Figure 1.12 Band structures of W based oxides.

In this present study, silver bismuth tungstate ($AgBiW_2O_8$) was prepared by combustion synthesis and its photocatalytic properties were examined.

Given the ability of tungstates to photogenerate H_2,[79] and the limited information on $AgBiW_2O_8$ and its photocatalytic attributes, another objective of this study was to demonstrate proof-of-concept for the application of the combustion synthesized $AgBiW_2O_8$ powder for the photocatalytic generation of syngas. Syngas is a gas mixture that contains varying amounts of CO and H_2. Common examples of producing syngas include the steam reforming of methane or liquid hydrocarbons, and the gasification of coal or biomass. Thermally mild (i.e., low temperature) alternatives for producing this transportable chemical fuel mixture obviously would be significant from an energy perspective. Value is even further added if the production process can be driven via a renewable solar energy source from a source greenhouse gas material such as CO_2.[83] Thus, a second innovative aspect of this study is to show that Pt-modified $AgBiW_2O_8$ can generate syngas under mild conditions involving only bandgap irradiation of the photocatalyst particle suspensions. Literature precedence for the photogeneration of syngas in homogeneous solutions containing noble metal complexes is duly noted.[84,85]

The focus of the study is on preparing oxide semiconductors by combustion synthesis process. The superior activity of the CS prepared oxides is established by comparing the photocatalytic activity of the CS powders against the corresponding commercial / solid state synthesized benchmark samples. The influence of combustion precursors is addressed for the first time. A proof-of-concept application for photogeneration of syngas is described in this research. The experimental details, results and conclusions are described in the following sections of the study.

CHAPTER 2

EXPERIMENTAL

2.1 Bismuth Vanadate ($BiVO_4$)

For the solution combustion synthesis process, bismuth nitrate pentahydrate, $Bi(NO_3)_3.5H_2O$ (Alfa Aesar, 99% pure), was used as the precursor for bismuth, and vanadium (III) chloride, VCl_3 (Alfa Aesar, 99% metals basis), or vanadium oxysulfate, $VOSO_4$ (Alfa Aesar, 99.9% metals basis) were used as precursors for vanadium. Urea, glycine, or citric acid was used as fuel. All chemicals were used as received. Double-distilled water (Corning Megapure) was used to prepare all solutions. A commercial sample of $BiVO_4$ (Alfa Aesar, 99.9% metals basis) was used as a reference material for benchmarking the characteristics of the combustion-synthesized (CS) powders.

2.1.1 Solution Combustion Synthesis of $BiVO_4$

Stochiometric mixtures of the oxide precursor and fuel were taken in a ceramic crucible and homogenized in 0.1 M HNO_3 medium. The acid serves to dissolve $Bi(NO_3)_3$ so that the precursor species are homogeneously dispersed. The solution was then transferred to a furnace pre-heated at 150 ℃ and left for 4-5 min. When the solution gets dehydrated, spontaneous combustion sets in and a foamy mass is obtained.[14] The CS samples were then taken out, finely ground in an agate mortar and pestle, and then thermally annealed at 600 ℃ for 30 min to ensure removal of trace organic combustion products from the powder surface and to improve crystallinity. Figure 2.1 shows a flow chart of the solution combustion synthesis procedure developed in this study.

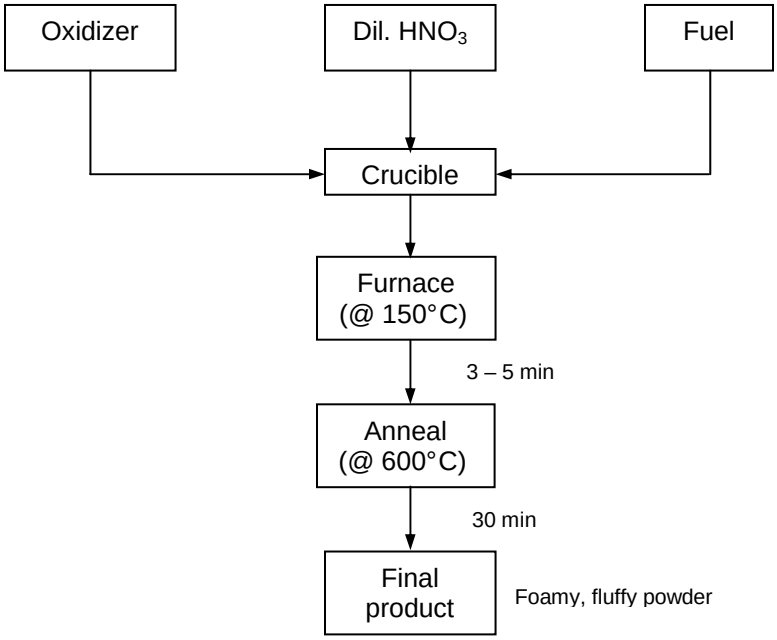

Figure 2.1 Flow chart of combustion synthesis procedure.

2.2 Silver Bismuth Tungstate ($AgBiW_2O_8$)

Silver nitrate, $AgNO_3$ (Fischer Scientific) bismuth nitrate pentahydrate, $Bi(NO_3)_3.5H_2O$ (Alfa Aesar, 99% pure), sodium tungsten oxide dihydrate, $Na_2WO_4.2H_2O$, (Alfa Aesar ACS 99.0–101.0%) were used as precursors for silver, bismuth and tungsten respectively, for solution combustion synthesis. Urea was used as fuel. All chemicals were used as received. Double-distilled water (Corning Megapure) was used to prepare all solutions. The photocatalytic activity of the combustion synthesized powders was compared against $AgBiW_2O_8$ prepared by solid state reaction, as outlined in the work of Tang and Ye.[76]

2.2.1 Solution Combustion Synthesis of $AgBiW_2O_8$

Stoichiometric mixtures of the sliver nitrate and bismuth nitrate were taken in a ceramic crucible and homogenized in 0.1 M HNO_3 medium, to enable dissolution of $Bi(NO_3)_3$ and homogenous dispersion of the precursor species. Stoichiometric mixtures of the tungsten precursor and the fuel were taken in a beaker, homogenized in water, and transferred to the crucible with the bismuth and silver precursor mixture. A white suspension was formed when the two solutions were mixed. The crucible was then placed in a furnace pre-heated at 150 ℃ and left for 4-5 min. The solution got dehydrated, and spontaneous combustion set in with the release of large amount of fumes, resulting in the formation of a pale yellow flaky powder as the final product. The sample was then taken out, finely ground in an agate mortar and pestle, washed several times with distilled water to remove any impurities, and finally dried overnight in an oven at 80 ℃. The combustion synthesized and the solid st ate synthesized samples are referred to as SCS–$AgBiW_2O_8$ and SCS–$AgBiW_2O_8$, respectively, throughout this work.

2.2.2 Platinum (Pt) Photodeposition on SCS – $AgBiW_2O_8$

For the photogeneration of syngas (CO + H_2) from formic acid and methane from acetic acid using the SCS-$AgBiW_2O_8$ photocatalyst, the SCS-$AgBiW_2O_8$ nanoparticles were pre-modified with Pt catalyst islands using a photodeposition procedure.[86] The required amount of SCS-$AgBiW_2O_8$ powder was dispersed in 50 ml water and the suspension was transferred to a 500 ml photoreactor, to which 13.5 ml of HCOOH (96%) and the the Pt precursor (K_2PtCl_6) were added. The Pt dose on the samples was 1 % (m/m basis). This reaction mixture was irradiated for 30 min under constant N_2 bubbling to ensure proper dispersion of the mixture and bring about the photodeposition of Pt onto the SCS-$AgBiW_2O_8$ particles. The resultant powder photocatalyst was filtered, dried overnight at 70° C and then finely ground before using it for the photocatalysis experiments.

2.3 Sample Characterization

Characterization of the combustion synthesized oxides was carried out using various analytical techniques. The characterization techniques, along with concise background information for each method are presented below.

2.3.1 Thermogravimetric Analysis (TGA)[87]

Thermogravimetric Analysis (TGA) measures the amount and rate of change in the weight of a material as a function of temperature or time in a controlled atmosphere. The thermal stability of a material and the fraction of its volatile components can be found out from the changes in mass occurring when the material is heated. In most cases, measurements are performed in an oxidative atmosphere (air or O_2 and inert gas mixtures) with a linear temperature ramp, and the change in mass is recorded as a function of increasing sample temperature. TGA measurements can give us information on the thermal and oxidative stability of a material, composition of multi-component systems, decomposition kinetics, moisture content etc. Materials exhibiting weight loss or gain due to decomposition, oxidation or dehydration can be characterized by TGA.

2.3.2 Differential Scanning Calorimetry (DSC)[87]

Differential scanning calorimetry (DSC) is a thermal analysis technique which measures the heat flow associated with transitions in materials as a function of temperature and time in a controlled atmosphere. The heat flow difference between the sample and a reference are recorded as they are subjected to a temperature program. Quantitative and qualitative information about the physical and chemical changes that include endothermic/exothermic processes or changes in heat capacity can be obtained from DSC measurements. DSC can give information regarding the glass transition temperatures, melting & boiling points, crystallization time & temperature, percent crystallinity, heats of fusion and reaction, specific heat, oxidative stability, reaction kinetics, purity, thermal stability, etc.

For the combustion synthesized oxides, the TGA and DSC analyses of the precursor mixtures were carried out using a TA Instruments Model Q600 instrument. The precursor mixtures were placed in an open ceramic crucible in flowing air/N_2 mixture (oxidative atmosphere), under a linear temperature ramp rate of 15 ℃/min.

2.3.3 X-Ray Diffraction (XRD)[87,88]

X-Ray diffraction (XRD) is a technique for estimating the crystal structure of a sample. XRD can be used to estimate the crystal structure of both single crystals and powder samples. A typical diffraction pattern contains a plot of the measured intensity against the diffraction angle (Bragg angle). In the case of powder samples, XRD analysis can provide information on the purity of the powder sample, and also identify the crystal structure of an unknown material. The basic principle of X – ray diffraction is as follows: When the sample is hit by an X – ray beam, the X – ray photons collide with the electrons in the sample and deflect away from the direction of the incident beam. The diffracted beams interfere with each other and the resultant intensity distribution is affected by the interaction. When there is constructive interference from the diffracted beams, a peak is observed and the intensity of the peak is measured against the diffraction angle. The positions of the peaks and intensities are used to identify the structure or phase of the sample.

The angle where the peak is formed is governed by Bragg's law, which gives the relation between the diffraction angle and the interplanar spacing between the atoms.

$$n\lambda = 2d\sin\theta \qquad (2.1)$$

where n is an integer, λ is the wavelength of the X-ray beam, d is the interplanar spacing between the atoms and θ is the diffraction angle (Bragg angle)

A powder diffraction pattern can give us information on the phase composition of the material (qualitative analysis), lattice parameters and Bragg reflection indices (quantitative analysis).

Powder X-ray diffraction (XRD) for the combustion synthesized samples was performed on a Siemens D-500 diffractometer using CuKα radiation. Diffractograms used a 2θ step size and dwell time of 0.02° and 1.25 s respectively. F urther analyses of the XRD patterns used the Philips X-pert Highscore software.

2.3.4 Diffuse Reflectance Spectroscopy (DFR)[89,90]

Diffuse reflectance spectroscopy is a technique to estimate the absorption properties of materials. For semiconductors, the absorption coefficient and band gap values can be estimated using DFR spectroscopy measurements. The band gap energies (E_g) for the various samples were calculated by plotting the values of $(\alpha h\nu)^n$ vs the photon energy ($h\nu$), [89,90] where α (also denoted as k) is the absorption coefficient.[89] The value of n in the relation depends on the type of transitions involved, n = 2 for a direct transition and n = ½ for an indirect transition.[89] The relation between the absorption coefficient and the reflectance of the sample is calculated from the Kubelka – Munk function, [90]

$$f(R) = \frac{(1 - R)^2}{2R} = \frac{k}{s} \qquad (2.2)$$

f(R) = Kubelka–Munk function; R = absolute reflectance of the sample; k (or α) = absorption coefficient; and s = scattering coefficient.

The percent reflectance (%R) values obtained from the diffuse reflectance measurements were converted to reflectance (R) values using the equation

$$\log\left(\frac{1}{R}\right) = 2 - \log_{10}(\%R) \qquad (2.3)$$

The band gap values are estimated from a plot of $[f(R).h\nu]^n$ vs $h\nu$[90]

For the combustion synthesized powder samples, the diffuse reflectance spectra of the were obtained on a Perkin–Elmer Lambda 35 spectrophotometer equipped with an integrating sphere. The band gap values were estimated from the plot of the Kubelka – Munk function versus the photon energy.[90]

2.3.5 X – Ray Photoelectron Spectroscopy (XPS)[87]

X – ray photoelectron spectroscopy (XPS), or electron spectroscopy for chemical applications (ESCA), is a non destructive spectroscopic technique for studying the surface of solids. It can be used to study the surface of any solid and can detect all elements (~ at 0.1 atomic percent abundance) except hydrogen.

In XPS, when a sample is placed in the path of x-rays of known energy, all the electrons with binding energies less than the energy of the x- rays are ejected, with a kinetic energy dependent on the incident X- ray and the binding energy of the atomic orbital. The kinetic energies of these photoelectrons are measured by an energy analyzer in a high resolution electron spectrometer to determine the concentrations of the elements present**.** The binding energy is indicative of a specific element and a particular structural feature of electron distribution. The relation between the binding energy and the kinetic energy is given by the following equation

$$E_b = h\nu - E_{kin} - \phi \qquad (2.4)$$

E_b is the binding energy of the electron, E_{kin} is the kinetic energy of the electron, $h\nu$ is the energy of the exciting radiation and Φ is the spectrometer work function (constant for a given analyzer).

The ability of this technique to study surfaces enables its use to study heterogeneous catalysts, polymers and polymer adhesion problems, metals, alloys and semiconductors.

2.3.6 Raman Spectroscopy[87]

Raman spectroscopy is a technique used to determine the molecular structures and compositions of organic and inorganic materials. Low frequency modes such as vibrational and rotational modes of a system can be studied using Raman spectroscopy. It relies on the interactions of inelastic scattering (Raman scattering) of monochromatic radiation with the sample. When a beam of monochromatic radiation passes through a sample and interacts with the electron cloud of the sample, the molecules in the sample undergo vibrations upon excitation from the ground state to a virtual energy state. Upon relaxation, the molecule emits a photon and returns to a different vibrational or rotational state.

When the molecule accepts energy from the incident scattered radiation, it is excited into a higher vibrational energy state (Stokes shift). If the molecule releases energy to the incident radiation, it returns to its ground vibrational state (anti Stokes shift). The difference between the incident and the Raman scattered radiation results in the vibrational spectrum of interest.

Raman spectra of the CS $BiVO_4$ samples, their precursor materials, and relevant commercial samples ($BiVO_4$,V_2O_5, Bi_2O_3) were recorded with a Horiba Jobin Yvon ARAMIS instrument using an excitation wavelength of 633 nm and a grating with 600 lines/mm. The slit width was set at 100 μm, the time exposure was typically 1 s, and 15 scans were averaged for each spectrum.

2.4 Photocatalysis Experiments

The photocatalytic activity of the CS samples and the commercial benchmark sample was assessed by using the photodegradation of methyl orange (MO) as a probe.[91] The reactor vessel[92] consisted of an inner and an outer cylindrical glass vessel. The light source (450 W tungsten-halogen lamp) was placed in the inner vessel, which had a provision for water circulation to maintain a uniform reactor temperature, and also to filter off infrared radiation. The light intensity (as measured on a radiometer/photometer @500 nm) was 0.14 μW/cm^2 when a glass inner vessel was used and was 0.33 μW/cm^2 when the inner vessel was made of quartz. The photocatalytic assessment was made with the glass inner vessel such that the UV portion of the lamp output was filtered out. The outer reaction vessel was equipped with a stirrer and ports for sample aliquot withdrawal. A gas inlet connection was also provided for continually purging the suspension and preventing it from settling. Figure 2.2 shows a schematic diagram of the photocatalysis reactor setup.

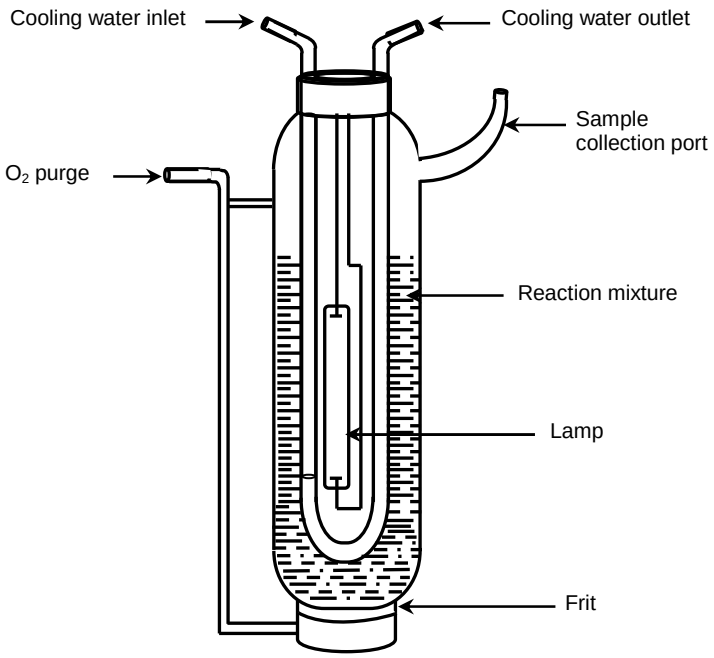

Figure 2.2 Schematic diagram of the photocatalysis reactor setup.

An aqueous suspension of 250 ml of 50 μM methyl orange solution and the CS powder photocatalyst (dose: 2 g/L) was taken in the photocatalytic reactor. The pH of the MO solution was adjusted in the range 3.0 – 3.2, as it was found from initial experiments that the optimum pH for the photocatalytic reaction is around 3.0. This result is also in agreement with previous studies on heterogeneous photocatalytic MO degradation.[47] Preliminary runs were made to assess the influence of purge gas (N_2 or O_2) on the MO degradation rate and it was found that O_2 purge better facilitated the photocatalytic reaction. Blank runs were performed under identical experimental conditions without the photocatalyst.

The reaction mixture was initially stirred in the dark for 30 min to attain adsorption equilibrium.[93] After 30 min, the light was turned on and sample aliquots were drawn out at periodic intervals (in this case, every 1 h). The samples were centrifuged, and filtered using a 0.45 μ membrane filter to remove any powder photocatalyst from the solution. The extent of MO degradation was estimated by measuring the absorbance of the solution at an analytical

wavelength of 502 nm, using an Agilent 8453 UV-visible spectrophotometer instrument. Figure 2.3 shows a representative time course of MO degradation (monitored via spectrophotometric measurement of MO light absorption) for combustion synthesized $BiVO_4$ powder.

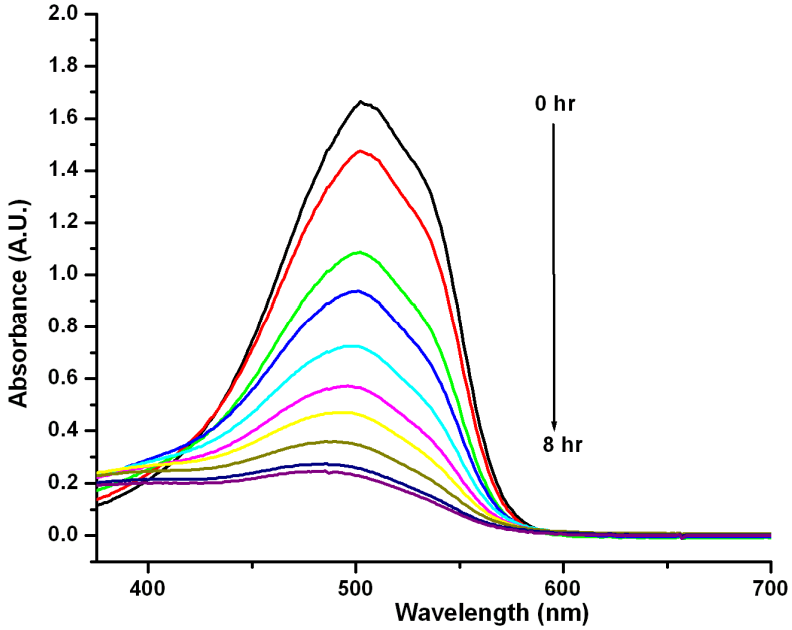

Figure 2.3 Time course of absorbance spectra showing photocatalytic degradation of methyl orange in a suspension containing CS sample, BV3.

For the photocatalysis runs with formic acid and acetic acid, the reaction mixture consisted of 0.5 g of Pt-modified SCS-$AgBiW_2O_8$ in 200 mL of 0.1 M carboxylic acid solutions saturated with N_2. The photoreactor was sealed and gas analysis was performed in a gas chromatograph equipped with a Shin Carbon column and a thermal conductivity detector, using an isothermal program at 70℃. The instrument was initially optimized for detection of CO, CH_4, CO_2, H_2 and O_2.

2.5 DFT Methodology

The electronic band structure of $AgBiW_2O_8$ was obtained using DFT calculations, which were carried out by Dr. Muhammad Huda and his group at the Physics Department at UTA, as a part of another collaboration work. The methodology and the results have been described in this present work in order to enable a better understanding of the band structure of $AgBiW_2O_8$. Given below is a description of the methodology used for calculating the band structure.

The electronic structure calculations were performed using the generalized gradient approximation (PBE-GGA functional), [94,95] by using DFT as implemented in the Vienna *ab initio* simulation package (VASP)[96,97] code and the standard frozen-core projector augmented-wave (PAW)[98,99] method. The density-of-states (DOS) plots were generated with the tetrahedron method.[100] The ion positions and volumes were always relaxed without any symmetry constraint to allow the internal geometry and the shape of the lattice to change freely and until the force on each of the ion was 0.01 eV/Å or less. For visualization of the crystal structures, Crystal Maker software was used.

2.6 Photoelectrochemistry

A single compartment, three-electrode cell set-up was used for the photoelectrochemistry [4] experiments. A platinum coil served as a counter electrode and a saturated Ag/AgCl electrode was used as a reference electrode. Working electrodes consisted of $BiVO_4$ films (CS samples and the commercial reference) coated on stainless steel foils (0.6 cm^2) by electrophoretic deposition (EPD). EPD was performed from alcoholic suspensions (45 mg in 3 mL of isopropanol) by applying an electric field of 20 V/cm between two parallel stainless steel electrodes for 15 min. The coated electrodes were annealed at 80°C for 30 min. Coated electrodes were weighed before and after being subjected to EPD to determine the amount of $BiVO_4$ in each film. Figure 2.4 shows a schematic setup of the photoelectrochemistry experiment setup. The PEC measurements used a full spectrum solar simulator (300W Oriel Solar

Simulator, Newport/Oriel instruments) whose output was manually interrupted to examine both the "dark" current and photocurrent behavior as a function of time. The photocurrent experiments were performed in 0.1M Na_2SO_4 supporting electrolyte. The photocatalysis experiments and the photoelectrochemical [4] measurements were carried out at ambient temperature.

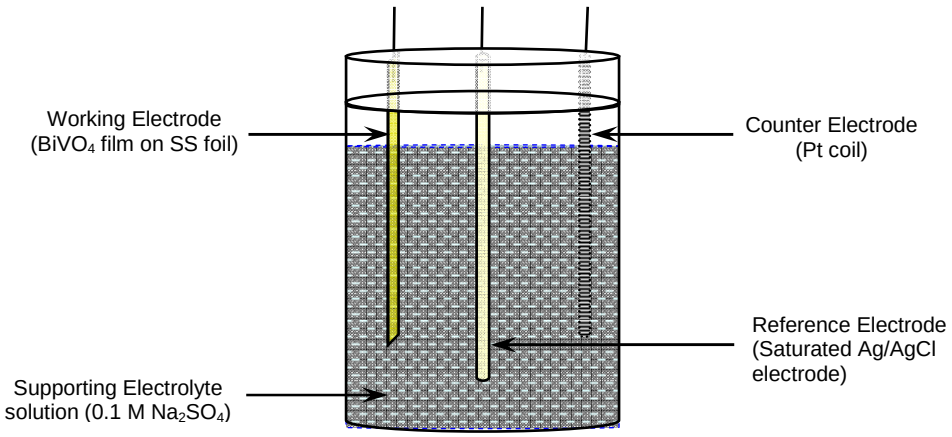

Figure 2.4 Schematic diagram of the photoelectrochemistry experiment setup.

2.7 Electrosynthesis of $BiVO_4$ Electrodes

The electrosynthesis procedure involved preparing the $BiVO_4$ electrodes supported on a Pt substrate. The procedure comprised of two steps: in the first step, a Bi film was electrodeposited on the substrate from an acidic $BiCl_3$ medium. In the second step, the film was transferred to a medium containing hydrolyzed vanadium precursor, and was anodically stripped to generate Bi^{3+}. In situ precipitation then yielded $BiVO_4$ on the substrate.

Bismuth chloride, $BiCl_3$ (Alfa Aesar 98% pure) was used as the precursor for bismuth. Ammonium vanadate, NH_4VO_3 (Alfa Aesar, 99% metals basis), was used as vanadium precursor. All chemicals were from commercial sources and used as received. Deaerated (ultrapure N_2-purge) and double-distilled water (Corning Megapure) was used to prepare all solutions.

A single compartment, three-electrode cell setup was used for the electrodeposition and photoelectrochemical experiments. A platinum disk working electrode (Bioanalytical Systems, 0.02 cm^2 geometric area) was polished to a mirror finish with alumina slurry (Buehler) and cleaned in an ultrasonic bath before use. A platinum coil served as a counter electrode and an Ag/AgCl/saturated KCl electrode was used as a reference. Photocurrents were measured with the full output of a 100 W tungsten halogen lamp. The details of the setup for the acquisition of photoaction spectra are given elsewhere,[86] as is a description of the instrumentation for scanning electron microscopy (SEM) [also equipped with an energy-dispersive X-ray analysis (EDX) probe] and X–ray photoelectron spectroscopy (XPS).[101] A "benchmark film" of commercial $BiVO_4$ (Alfa Aesar, 99.9% metals basis) was prepared on a stainless steel substrate (0.6 cm^2) by electrophoretic deposition at 20 V/cm from an alcoholic suspension (45 mg in 3 mL of isopropanol) for 15 min. The coated film was then subjected to thermal annealing at 80℃ for 30 min.

CHAPTER 3

RESULTS AND DISCUSSION

3.1 Solution Combustion Synthesis of $BiVO_4$

As mentioned in the introduction section, combustion synthesis involves heating a reaction mixture, which comprises of an oxidizing agent (metal salt) and a reducing agent (fuel) in stoichiometric quantities. The ratio of the oxidizer – fuel (O/F ratio, denoted by Φ) is based on rocket propellant theory, which shows that the maximum energy is released when the O/F ratio is unity.[18]

3.1.1 Fuel Precursor Combinations and Thermal Analyses

The precursor – fuel combinations included in this study are described in Table 3.1. Two sets of CS samples were prepared: one set with VCl_3 and another with $VOSO_4$ as the oxide precursor for vanadium. Three different fuels, urea, glycine and citric acid were used in the sample preparation. The different combinations of precursors and fuels are listed below in Table 3.1.

Table 3.1 $BiVO_4$ samples prepared from different precursors and fuels

Sample	Precursor	Fuel	Band gap (eV)
BV1	$(BiNO_3)_3.5H_2O + VCl_3$	Urea	2.17 ± 0.01
BV2		Glycine	2.22 ± 0.01
BV3		Citric acid	2.23 ± 0.01
BV4	$BiNO_3)_3.5H_2O + VOSO_4$	Urea	2.34 ± 0.01
BV5		Glycine	2.39 ± 0.01
BV6		Citric acid	2.44 ± 0.01
$BiVO_4$ (ref)			2.36 ± 0.01

Figure 3.1 contains a representative photograph of the CS $BiVO_4$ at three stages in the solution combustion synthesis process.

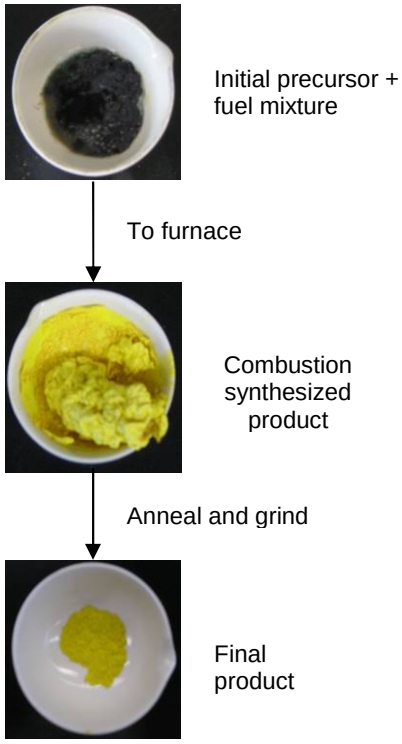

Figure 3.1 Different stages of the $BiVO_4$ combustion synthesis process.

The final CS product was yellow in color, as seen from Figure 3.1, and its visual appearance is similar to the material synthesized by other methods (Refs. 20, 29, 31). Initial experiments were performed by varying the Bi:V mole ratio in the precursor mixture, and it was found that a ratio of 1:1 was optimal for monoclinic $BiVO_4$ formation. This finding is in accord with those of previous authors using solution synthesis procedures.[27]

The details of the combustion synthesis process can be better understood from the thermal analysis of the precursor mixtures. Figure 3.2 contains the TGA profiles of the CS sample precursors. Thermal analyses offer useful insights into the combustion synthesis details. Figure 3.2 contains TGA profiles of precursor mixtures for the six CS samples. Broadly 2 – 3

regimes of mass loss can be seen depending on the choice of fuel. The first mass loss step (~ 40 % mass loss) occurs between 100℃ and 150℃; ass igned to the loss of water from the mixed metal salts and the fuel. A second mass loss regime (~ 15 – 25 % mass loss) occurs over a rather wide temperature span (ranging from 250 – 300℃ to ~ 475℃) depending on whether the fuel is urea or glycine / citric acid respectively. This regime originates from a combination of fuel decomposition [especially urea which is least stable[48]] and metal salt decomposition processes. A third regime (accounting for another ~ 15 % mass loss) occurs at temperatures > 500℃ only for the case where urea is the fuel (Figure 3.3). This step corresponds to the loss of residual organic carbon from the matrix.

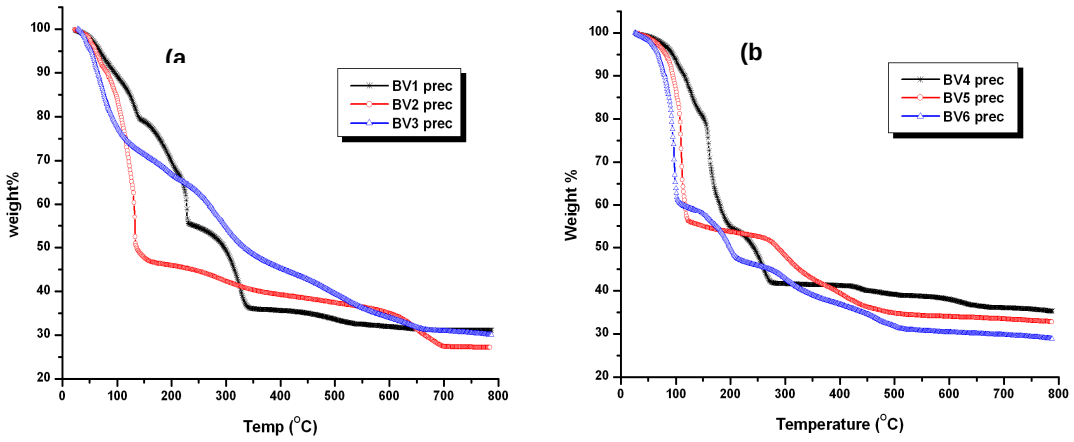

Figure 3.2 TGA data of the CS precursor mixtures.

The “cleanest” TGA profile is observed for the BV2 precursor with glycine as the fuel. This trend also mirrored the visual appearance of the CS product obtained in the three cases. The final product was fluffy and flaky with urea or citric acid as the fuel whereas in the case of glycine, the CS product was a fine powder.

Figure 3.3 contains DSC profiles of the precursor mixtures for the six samples considered in Figure 3.2 above. These profiles are complex showing both endothermic and exothermic peaks. The exothermic signals correspond to oxidative decomposition of the fuel plus combustion of the precursor mixture and these mainly correspond to the second regime in the

TGA mass loss profiles (Figure. 3.2). The endothermic DSC peaks are assignable to loss of water from the matrix along with other thermal decomposition steps.

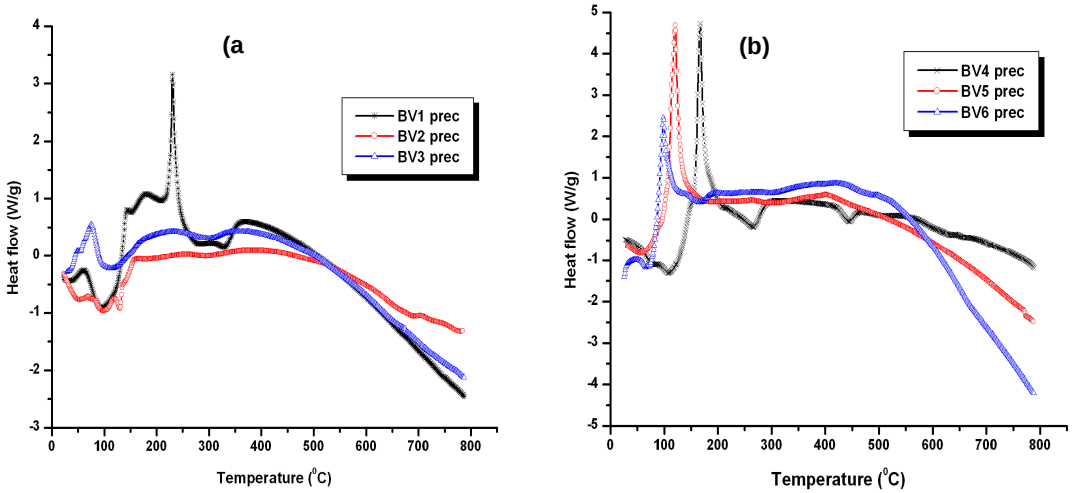

Figure 3.3. DSC data of the CS precursor mixtures.

3.1.2 Influence of Vanadium Precursor

Generally speaking, the CS products derived from vanadium chloride as precursor were better in terms of lower energy band gap values and photocatalytic activity as elaborated further in the subsequent sections. The reason for this can be seen in the TGA profiles for the two V precursors shown in Figure 3.2. Clearly the chloride salt is less refractory relative to the oxysulfate counterpart and its thermal decomposition also has a “cleaner” profile. Concomitantly the more facile decomposition of the chloride salt simultaneously promotes the parallel formation of V_2O_5, (from the XRD and Raman spectroscopy data below) that is beneficial from a practical application standpoint of $BiVO_4$. The differences in the product morphology for the two precursors, evident from the TEM data presented in Figure 3.6, also can be rationalized on the basis of the thermal behavior shown in Figure 3.2.

3.1.3 Sample Characterization

Monoclinic form of $BiVO_4$ was obtained using the Bi:V mole ratio of 1:1, and keeping the O/F ratio also at 1. As mentioned above, the samples were annealed at 600℃ to improve the crystallinity of the sample and also to remove residual carbon and other impurities. The annealing step was optimized with the aim to promote conversion to the photocatalytically active monoclinic phase of $BiVO_4$. In this regard, it is noteworthy that the photocatalytic activity of a related compound such as Bi_2MoO_6 prepared by a reflux method was reported to be dependent on the annealing temperature and the resulting crystallinity was an important factor for the photocatalytic activity.[102] Figure 3.4 shows the XRD images for a representative sample (BV3) before and after the annealing step. The characteristic signature of the monoclinic form is evident from the XRD data only after annealing.

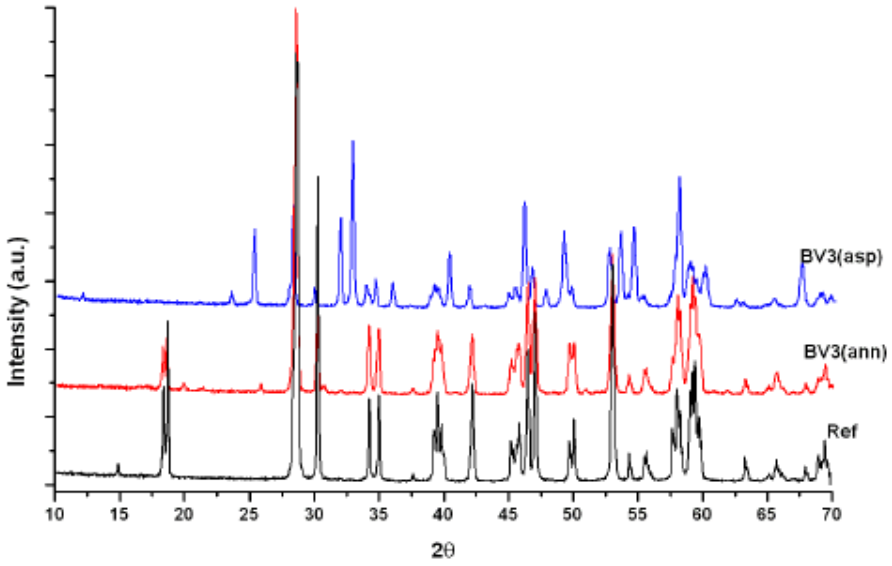

Figure 3.4 XRD data of sample BV3before and after annealing.

Figure 3.5 contains powder XRD patterns for six optimized CS products compared in each case with the commercial benchmark sample. Evidence of the monoclinic form is seen from the characteristic splitting of the diffraction peak signals at 2θ values of 18.5°, 35° and 47.5°. [54] When VCl_3 was used as the precursor, traces of V_2O_5 as diagnosed by the peaks labeled with * in Figure 3.5 (a) were also seen. Elemental analyses was carried out on the samples and yielded a 3.7 % level of oxide by mass. Small amounts of the tetragonal zircon phase were also observed, diagnosed by peaks labeled with ♦ in Figure 3.5 (b) when $VOSO_4$ was used as the vanadium precursor.

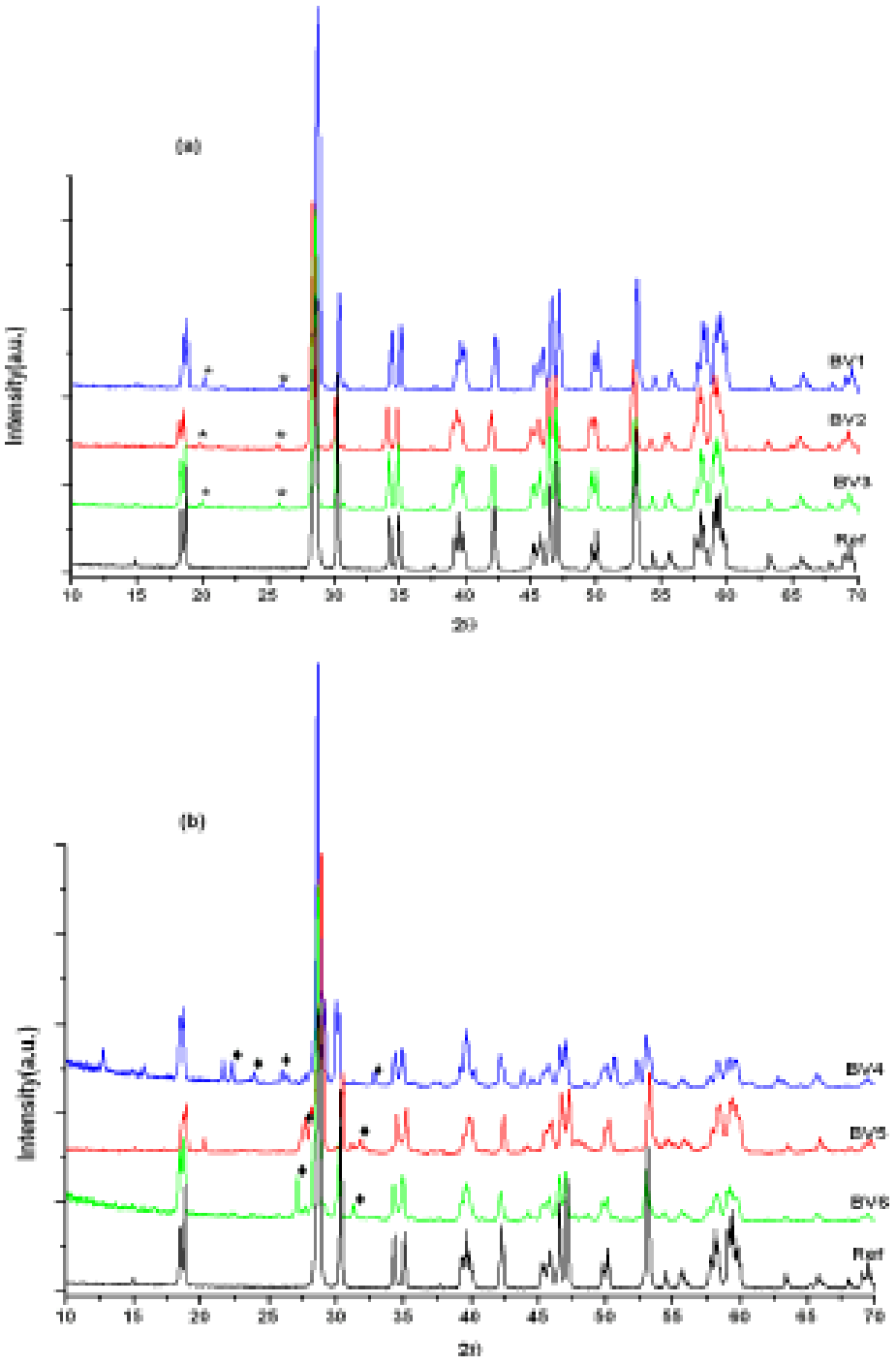

Figure 3.5 XRD spectra of the CS samples along with the reference. Peaks due to V_2O_5 are denoted by an * and $BiVO_4$ (pucherite form) are denoted by ♦.

The average particle size, estimated from the XRD peaks using the Scherrer equation,[88] yielded a value of ~ 34 nm for the CS samples while the particle size was about three times larger (~ 94 nm) in the commercial sample.

$$D = \frac{K \lambda}{\beta \cos \theta} \qquad (3.1)$$

D is the particle size, K is a constant (0.89), λ is the CuK_α wavelength (1.5405 Å), β is the full width at half maximum (FWHM) in radians of a selected diffraction peak and θ is the diffraction angle.

In principle, the crystal size estimation by Scherrer equation can only be applied to well crystallized samples, otherwise the XRD peak broadening might just reflect low crystallinity instead of nanosized entities.[103] Therefore, TEM images of CS $BiVO_4$ samples prepared from the two vanadium precursors were additionally acquired and are compared in Figure 3.6 : BV2 (frames a1, a2) from VCl_3 vs. BV4 (frames b1, b2) from $VOSO_4$. The CS $BiVO_4$ samples from VCl_3 are seen to be nanocrystalline showing aggregates of elongated crystals suggesting monoclinic phase, and in accord with their typical monoclinic XRD patterns [Figure 3.5 (a)], while samples from $VOSO_4$ shows smaller but mainly round nanocrystalline particles, their nanocrystallinity detected by lattice fringes appearing in some of them (Figure 3.6, frames b1, b2).

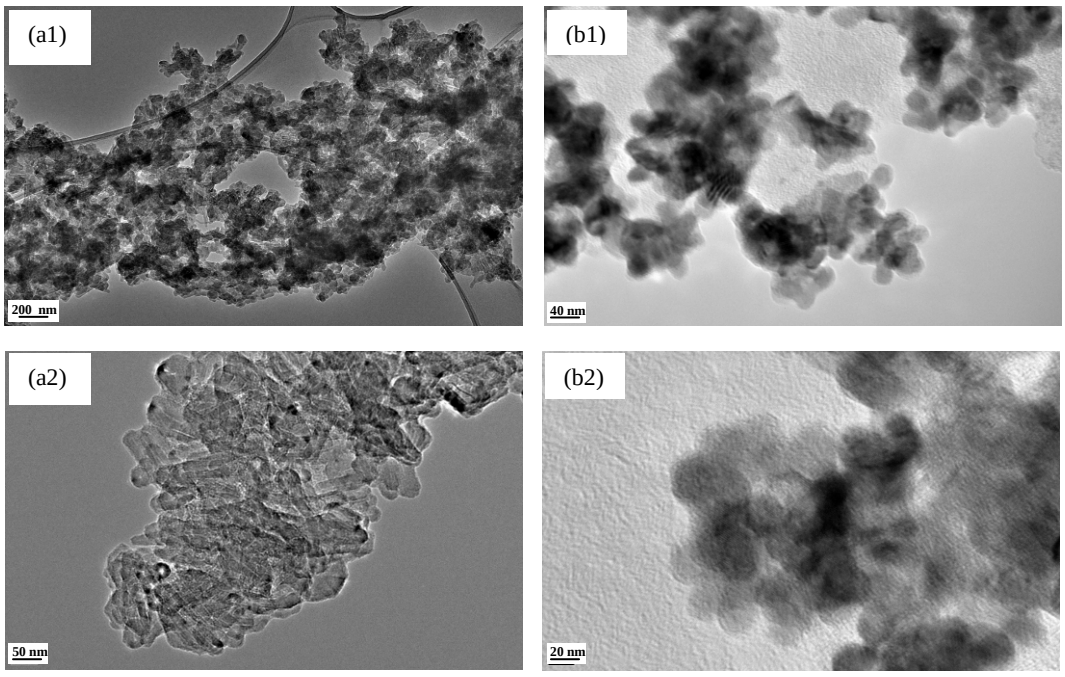

Figure 3.6 TEM images of selected CS $BiVO_4$ prepared from VCl_3 (a1 and a2) and from $VOSO_4$ (b1 and b2) using glycine as fuel.

Figure 3.7 contains Tauc plots[89] constructed from the UV visible diffuse reflectance data for the six CS samples as well as for the commercial benchmark sample. The band gap energies (E_g) for the various samples were calculated by plotting the values of $(\alpha h\nu)^n$ vs the photon energy ($h\nu$), [89,90] where α (also denoted as k) is the absorption coefficient.[89] The band gap values are estimated from a plot of $[f(R).h\nu]^n$ vs $h\nu$,[90] and were found to range from 2.17 eV to 2.44 eV while the commercial $BiVO_4$ sample shows an E_g of 2.36 eV. The E_g values are also listed in Table 3.1.

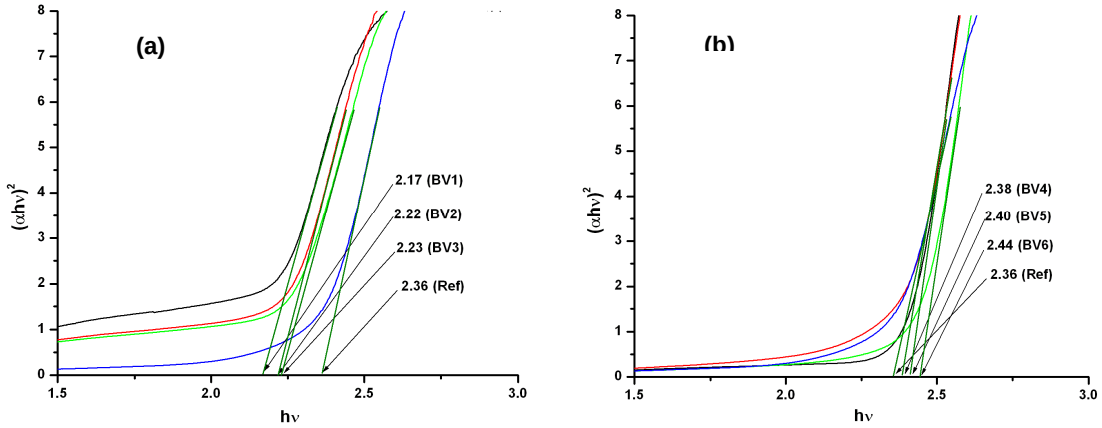

Figure 3.7 Tauc plots showing band gap (E_g) values for the CS samples and the reference.

To assess the effect of the precursor on the E_g values of $BiVO_4$ samples, statistical significance (null hypothesis) tests were carried out by performing replicates (at least 4) on each of the samples and the reference considered in Figure 3.7. Student t-tests [104] were performed to compare pairs of E_g values derived from Figures 3.7(a) and 3.7(b) respectively, using the average E_g values from replicates. The following conclusions could be drawn from the statistical data analyses, (95% confidence level): (a) E_g values for samples derived from VCl_3 were lower than those derived from $VOSO_4$. (b) E_g values for samples derived from VCl_3 are lower than that of the reference sample while the values for $VOSO_4$ are higher than that of the reference specimen. These trends can be mechanistically rationalized on the basis of the precursor thermal stability differences of the two precursors (Figure 3.8) and the corresponding morphological variations discussed earlier.

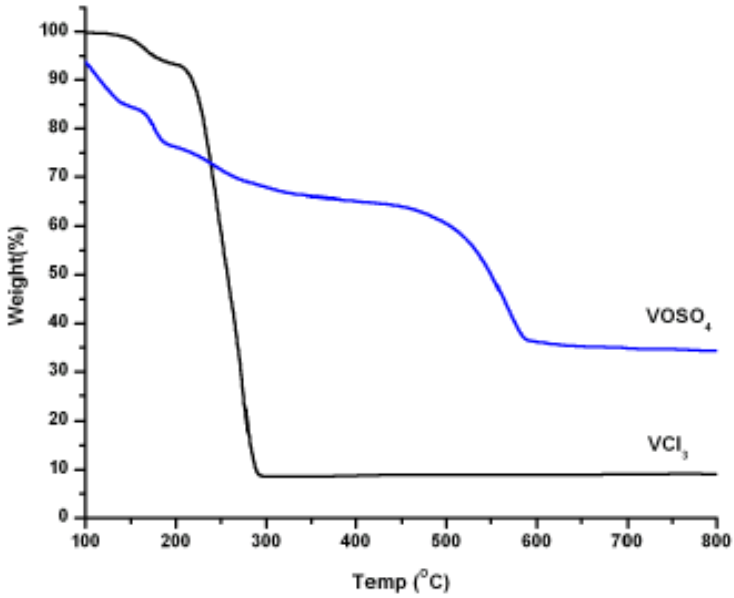

Figure 3.8 TGA profiles for the two vanadium precursors used in this study.

Tetragonal $BiVO_4$ has a much larger E_g value of 2.9 eV.[27] Even for monoclinic $BiVO_4$, the values of E_g varies from 2.4 eV,[27] 2.45 eV,[37] 2.34 eV,[43] 2.45 eV,[48] 2.43 eV,[51] 2.34 – 2.43 eV,[52] and 2.4 eV,[56] depending on the mode of synthesis, and this is reflected in the literature data as well. For example, variations in the pH from 1 to 9 in hydrothermal synthesis resulted in $BiVO_4$ samples ranging in E_g value from 2.39 eV to 2.47 eV respectively.[38] Similarly, monoclinic $BiVO_4$ obtained from hydrothermal synthesis in another study had E_g values of 2.39 eV, 2.40 eV, and 2.46 eV for cuboid-like, square plate-like and flower-like morphologies respectively.[58]

Further characterization of the CS samples was done using Raman spectroscopy. Spectra for the six CS $BiVO_4$ samples compared to the commercial benchmark sample of $BiVO_4$ are shown in Figure 3.9. Table 3.2 compiles their Raman band positions and assignments.[31] Initial observation of Figure 3.9 reveals a close resemblance between the benchmark sample and the six CS samples, although other minor peaks are seen in the CS samples synthesized from

VCl_3 [Figure 3.9 (a)], while the match between the benchmark and CS samples is perfect when $VOSO_4$ was used as precursor [Figure 3.9 (b)].

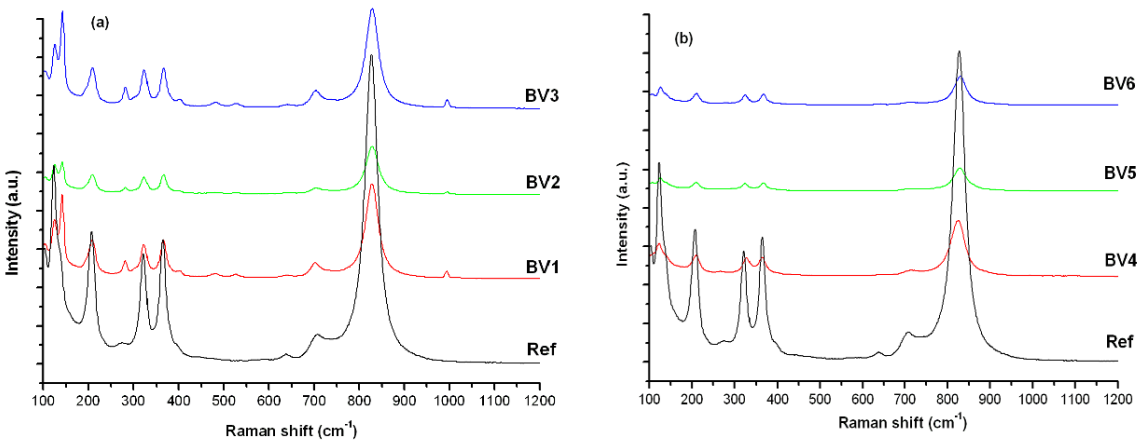

Figure 3.9 Raman spectra of the CS samples along with the reference.

Table 3.2 Raman Bands (cm^{-1}) of the CS samples and the benchmark $BiVO_4$.

BV1	BV2	BV3	BV4	BV5	BV6	Benchmark	Assignment
828	829	828	824	828	829	826	ν_s (V–O)
701	704	703	714	710	707	709	ν_{as} (V–O)
366	366	366	364	367	367	364	δ_s (VO_4^{3-})
323	323	323	328	324	325	322	δ_{as} (VO_4^{3-})
209	209	209	210	211	211	207	lattice mode
142	142	143	123	125	126	123	lattice mode

ν_s = symmetric stretching; ν_{as} = asymmetric stretching; δ_s = symmetric bending; δ_{as} = asymmetric bending

Vibrational spectra of minerals containing pentavalent vanadium show four vibrations for VO_4^{3-}, namely, an A_1 symmetric stretching signal, an E bending mode, an F_2 antisymmetric stretching peak and a F_2 bending mode.[105] The F_2 modes are both Raman and infrared active while the A_1 and E modes are Raman active only. Therefore, four vibrational modes are expected to be present in the Raman spectra of CS $BiVO_4$ samples.

Monoclinic $BiVO_4$ is reported to exhibit a strong V–O symmetric stretching band, ν_s(V–O), at ca. 824 cm^{-1},[31] which is the most prominent in all the CS samples in agreement with the monoclinic structure indicated by the XRD data. The band position varies from 824 cm^{-1} to 829 cm^{-1} in the CS samples. Depending on the method of preparation of $BiVO_4$, the band position was also reported to range from 812 cm^{-1} (aqueous process) [36] to 832 cm^{-1} (ammonia coprecipitation).[54] It was reported that the stretching frequency has a relation to the V–O bond length, wherein lower frequencies of the V–O stretching band correspond to longer bond lengths.[38]

A weak V–O antisymmetric/asymmetric stretching vibration band, ν_{as} (V–O), is reported in the range of 700 cm^{-1} to 723 cm^{-1}, while the medium intensity symmetric, δ_s (VO_4^{3-}), and asymmetric, δ_{as} (VO_4^{3-}), bending modes of VO_4^{3-} are reported around 365 cm^{-1} and 320 cm^{-1} respectively[106] and in full agreement with signature of the CS samples. Also, bands peaking at ca. 208 cm^{-1} and 140 cm^{-1} caused by lattice vibrations[31] are clearly seen in the spectra of our CS samples, corroborating again that the CS samples exhibit the requisite features corresponding to the vibration bands of monoclinic $BiVO_4$.

Considering the probability of bismuth and/or vanadium oxide formation during the combustion synthesis of $BiVO_4$, Raman spectra of Bi_2O_3, V_2O_5 and also of VCl_3 were also acquired (Figure 3.10). On comparing the spectra in Figures 3.9 (a) and 3.10, it is seen that that the extra peaks in the CS samples prepared from VCl_3 [Figure 3.9 (a)] arise from the formation of V_2O_5 which is characterized by nine bands in the 100–1200 cm^{-1} range located at 140, 193, 280, 302, 401, 478, 525, 699 and 992 cm^{-1} respectively. Seven out of these bands are seen in the spectra of Figure 3.9 (a) while those at 193 cm^{-1} and 302 cm^{-1} are hidden as shoulders of more intense bands from the parent $BiVO_4$ structure. The highest frequency band at 992 cm^{-1} is characteristic of V_2O_5 and it is assigned to the antisymmetric stretching vibration of the V–O–V group,[107] and is clearly present in CS samples BV1, BV2 and BV3.

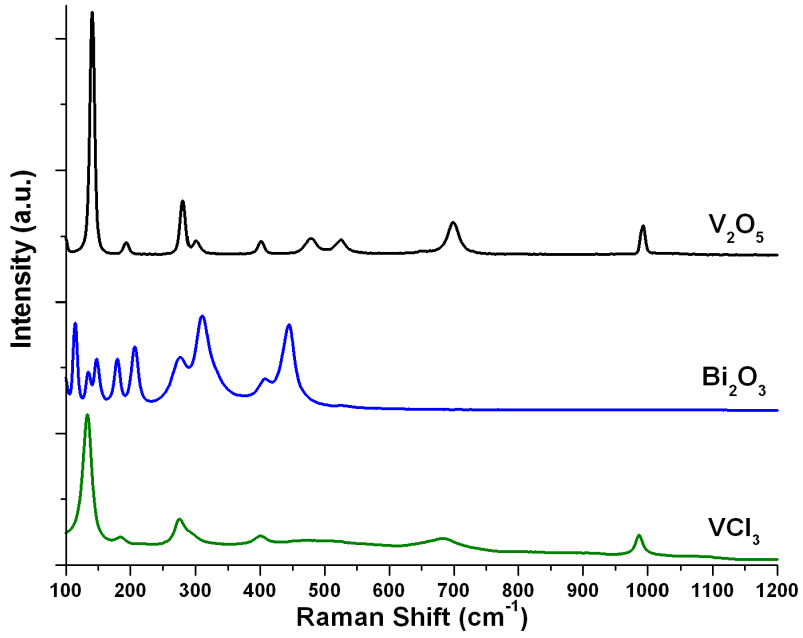

Figure 3.10 Raman spectra of relevant commercial samples.

3.2 Photocatalytic Behavior of $BiVO_4$

The photocatalytic behavior of the CS $BiVO_4$ samples was evaluated using methyl orange (MO) as a probe. Methyl orange has been used as a probe material in other studies on $BiVO_4$ photoactivity.[37,47,53,58] Various solution probes used by other researchers include alkylphenols,[30] N,N,N´,N´–tetramethylated rhodamine,[39] phenol,[40-42] Cr (VI),[42] methylene blue[43] and eosin Y.[60] Comparisons were made in these previous studies with other oxide photocatalysts (such as TiO_2) or with $BiVO_4$ prepared from solid state reaction. The illumination sources in previous studies on MO photodegradation ranged from high pressure Hg lamp,[37] 12W energy saving lamp,[47] 500W Xe lamp,[53] or even sunlight.[58]

Figure 3.11 contains the concentration – time profiles for methyl orange (MO) dye degradation as observed for the six CS samples under *visible light* illumination. The profiles for

the blank sample (without photocatalyst) and the commercial benchmark sample are also shown for comparison. The decrease in concentration was calculated using the equation

$$\% \text{ degradation} = \frac{C_t}{C_0} \times 100 \qquad (3.2)$$

where C_t is the concentration at time 't', C_0 is the concentration at time t=0.

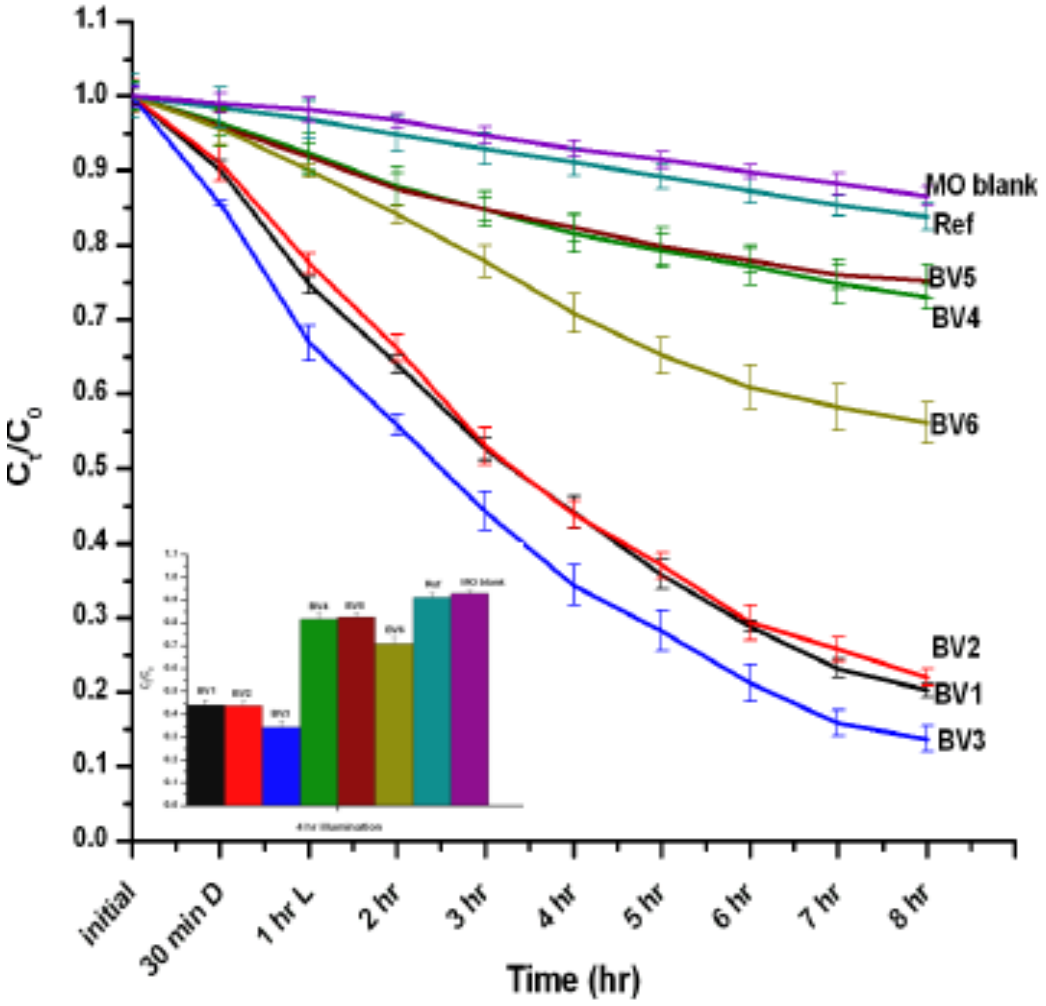

Figure 3.11 MO photodegradation profiles in suspensions containing CS samples and the benchmark sample (Ref). MO blank runs represent an experiment without the photocatalyst. Inset figure shows the degradation profile after 4 hr illumination.

From the above, it can be noted that (a) MO photodegradation is negligible in the absence of $BiVO_4$, even after several hours of illumination. (b) all the six CS samples showed superior photocatalytic activity than the commercial benchmark $BiVO_4$ (ref) counterpart. A bar diagram comparing the performance of all the samples after 4 h of irradiation is included as an inset in Figure 3.11.

MO degradation has been shown to occur by three possible mechanisms[47]; (a) photolysis of the dye, (b) photosensitization, wherein an electron from the dye is excited by light irradiation and injected onto the conduction band of the photocatalyst, and (c) heterogeneous photocatalysis mechanism where the light energy promotes an electron from the valence band of the photocatalyst to the conduction band, and the holes formed in the valence band oxidize the dye. Studies carried out by other researchers on the photodegradation of MO indicate that the degradation occurs via a combination of photosensitization and photocatalysis processes, where both the photogenerated electrons and the $OH^{\bullet}$ formed degrade the dye in parallel pathways. [47]

O_2 also plays an important role in the photooxidation reactions.[108] O_2 reacts with the conduction band electrons to form a $O_2^{-\bullet}$ radical, which in turn forms the $OH^{\bullet}$ radical. The organics are then degraded directly by the photogenerated holes from the valence band, or indirectly by the $OH^{\bullet}$ radical.[108]

Degradation of MO by the photolysis mechanism is not predominant in our case, since the degradation profile in the absence of the photocatalyst is negligible (MO blank in Figure 3.11 and inset figure). Therefore, it can be said that the degradation occurs via photosensitization and photocatalytic pathways.

The possible degradation reactions are given below, along with a schematic (Figure 3.12) describing the degradation mechanism. [47]

$$MO + h\nu \rightarrow MO^{*} \quad (3.3)$$

$$MO^{*} + BiVO_4 \rightarrow MO^{+\bullet} + BiVO_4(e^{-}) \quad (3.4)$$

$$BiVO_4(e^{-}) + O_2 \rightarrow O_2^{-\bullet} + BiVO_4 \quad (3.5)$$

$$BiVO_4(e^{-}) + O_2^{-\bullet} + H^{+} \rightarrow H_2O_2 \quad (3.6)$$

$$H_2O_2 + e^{-} \rightarrow OH^{\bullet} + OH^{-} \quad (3.7)$$

$$MO + OH^{\bullet} \rightarrow\rightarrow CO_2 + H_2O \quad (3.8)$$

$$BiVO_4 + h\nu \rightarrow BiVO_4(e^{-}) + BiVO_4(h^{+}) \quad (3.9)$$

$$MO + BiVO_4(h^{+}) \rightarrow MO^{+\bullet} + BiVO_4 \quad (3.10)$$

$$H_2O + BiVO_4(h^{+}) \rightarrow OH^{\bullet} + H^{+} + BiVO_4 \quad (3.11)$$

$$BiVO_4(e^{-}) + O_2 \rightarrow O_2^{-\bullet} + BiVO_4 \quad (3.12)$$

$$BiVO_4(e^{-}) + O_2^{-\bullet} + H^{+} \rightarrow H_2O_2 \quad (3.13)$$

$$H_2O_2 + e^{-} \rightarrow OH^{\bullet} + OH^{-} \quad (3.14)$$

$$MO + OH^{\bullet} \rightarrow\rightarrow CO_2 + H_2O \quad (3.15)$$

Equations 3.3 to 3.8 indicate the photosensitization pathway, and equations 3.8 to 3.15 depict the photocatalysis pathway for MO degradation.

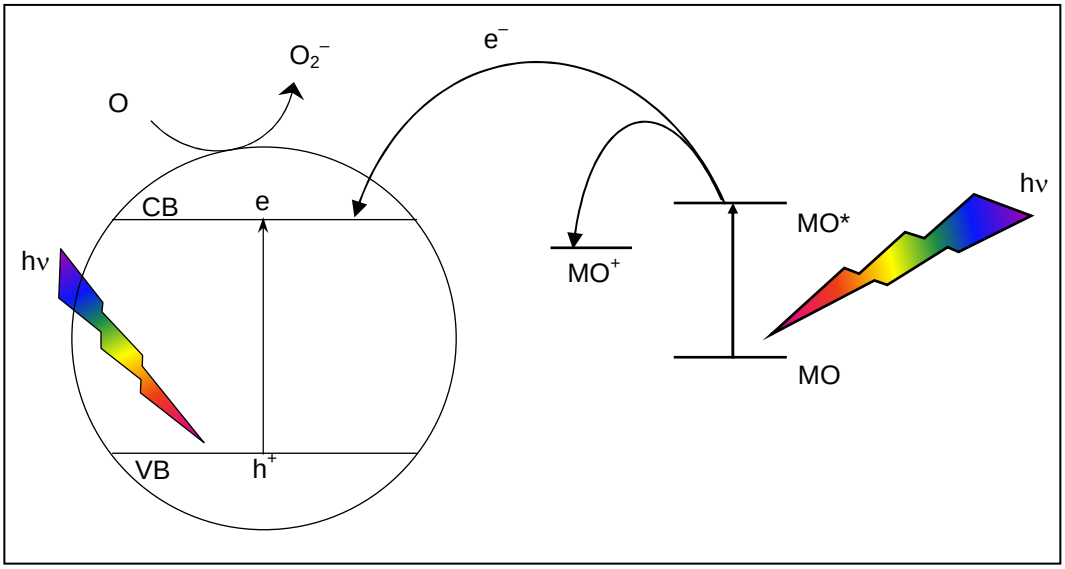

Figure 3.12 Schematic representation of MO photodegradation mechanism.

Similar to the studies on the band gap data, statistical significance tests (Student t-tests) were performed to assess the trends in PC activity of the six CS samples relative to one another

and with respect to the commercial benchmark ("Ref" in Figure 3.11). The following conclusions could be made (with 95% confidence and n = 4): (a) All the six CS samples have superior PC activity relative to the commercial sample. (b) The photocatalytic activity of BV1 and BV2 are comparable as are BV4 and BV5. (c) CS samples prepared from VCl_3 show superior PC activity relative to samples from $VOSO_4$.

The specific surface areas of the six CS samples ranged from 0.30 m^2/g to 1.35 m^2/g while the commercial sample had a value of 0.45 m^2/g. BV1, BV2, BV3 samples all had consistently lower surface areas than BV4, BV5, and BV6, yet were superior in their PC activity. In general, all these surface areas are low – a trend that is generally true for CS – derived samples.[74] The higher PC activity of BV1, BV2, and BV3 (relative to BV4, BV5, BV6 and also to the reference sample) is likely due to their lower E_g values, affording a higher light absorption cross-section. Also, the presence of trace amounts of V_2O_5 could result in enhanced activity. Studies have shown that composites of V_2O_5–$BiVO_4$ enhance the photocatalytic activity due to heterojunction formation between V_2O_5 and $BiVO_4$, wherein the heterojunction structure is said to increase the separation extent and lifetime of the photogenerated e^-–h^+ pairs. [72,109]

Notwithstanding spectral distribution and photon flux variations, some broad comparisons for MO degradation of our CS samples with $BiVO_4$ synthesized by other methods[37] are possible. $BiVO_4$ samples from a "facile" sonochemical method showed very high PC activity: ~ 90 % MO was photodegraded in 30 min compared with ~ 8 % for $BiVO_4$ prepared by solid state reaction and ~ 6 % for Degussa P25 TiO_2.[37] On the other hand, only ~ 10 % of MO was photodegraded after ~ 4 h irradiation of solution synthesized $BiVO_4$.[47] Platinum loading increased the PC activity to ~ 70 % MO photodegradation. Surfactant assisted hydrothermally synthesized $BiVO_4$ resulted in ~85 % MO photodegradation after 90 min irradiation.[53] Finally, 36–58 % of the initial MO present was photodegraded by hydrothermally synthesized $BiVO_4$ after 4 h in another study conducted in outdoor sunlight.[58] The variability was due to the pH employed for the suspensions in the hydrothermal procedure. In contrast, Degussa P–25 TiO_2 only showed ~ 12 % MO photodegradation.

In comparison, our CS samples (450W tungsten halogen lamp irradiation) resulted in MO photodegradation levels ~ 65 % after 4 h (BV3) depending on the precursor and the fuel; BV3 showed the highest PC activity (Figure 3.11). On the other hand, the commercial benchmark $BiVO_4$ caused only ~ 5 % MO photodegradation over the same time interval.

3.3 Photoelectrochemistry of $BiVO_4$

The optical absorption in monoclinic $BiVO_4$ results in the excitation of electrons from a Bi 6s – O 2p hybrid valence band to a V 3d derived conduction band.[27] However, the trap sites on the oxide surfaces act as recombination centers for the photogenerated e^-–h^+ pairs. Minimizing the extent of surface recombination enhances the performance of the material with respect to both its photocatalytic efficacy and practically useful photoelectrochemical processes such as water oxidation. To this end, *films* were prepared of the CS $BiVO_4$ powder and irradiated at a fixed bias potential in 0.1 M Na_2SO_4 supporting electrolyte. The results are shown for sample BV2 at the two bias potentials: 1.0 V (Figure 3.13) and 0.40 V (Figure 3.14) respectively.

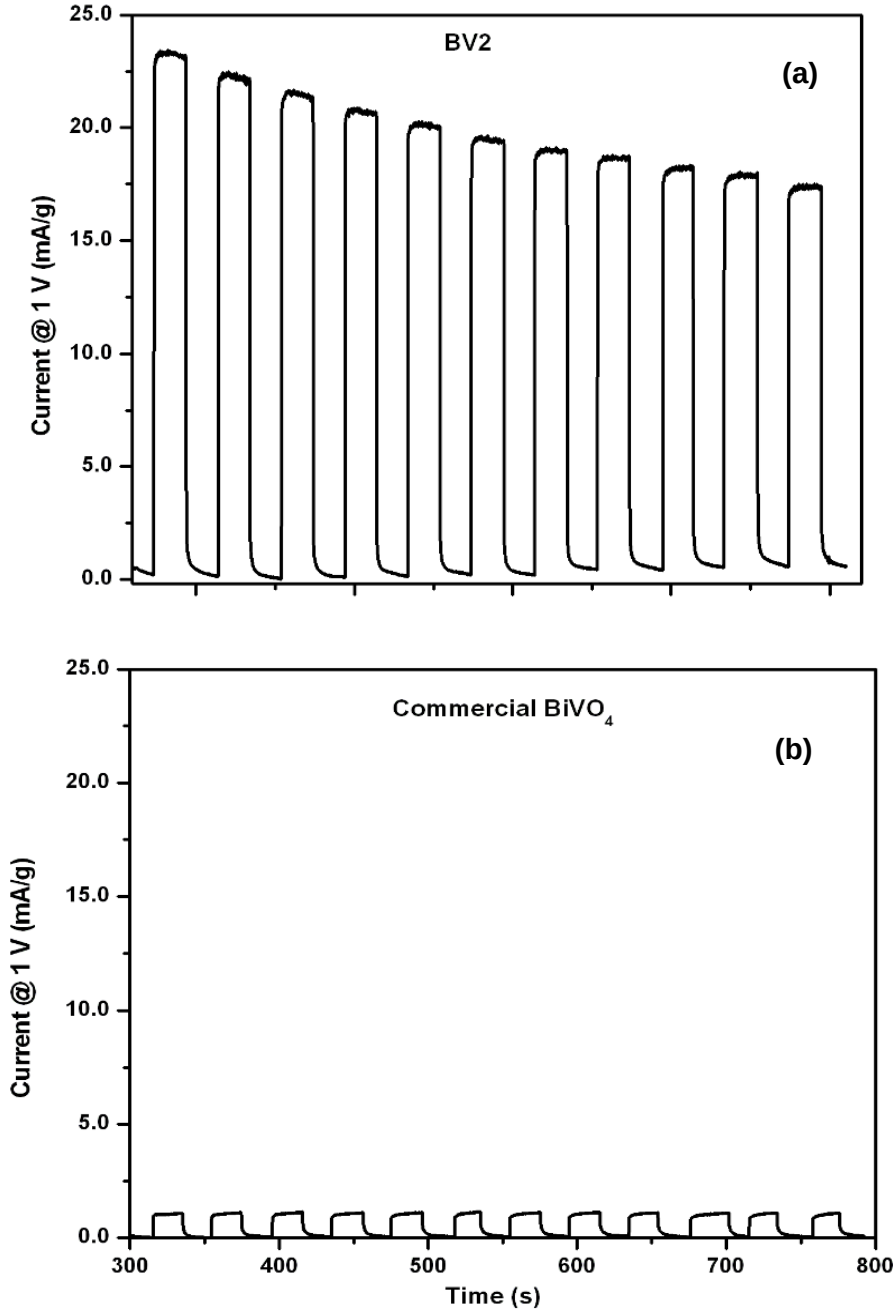

Figure 3.13 Photocurrent measurements of CS sample BV2 (a) compared with the reference (b). Photocurrents were measured at 1.0 V using a solar simulator (300 W) as the light source, and 0.1 M Na_2SO_4 as supporting electrolyte.

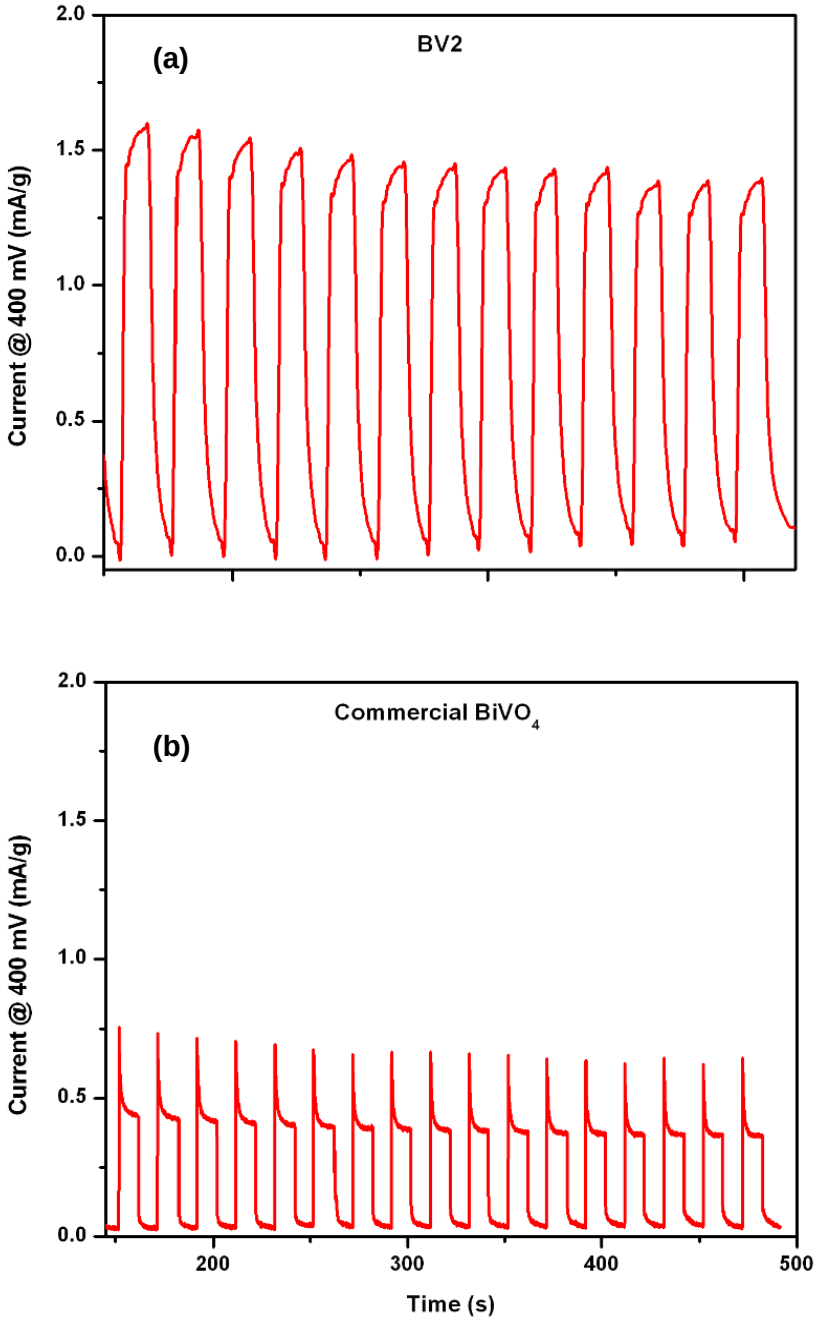

Figure 3.14 Photocurrent measurements of CS sample BV2 (a) compared with the reference (b). Photocurrents were measured at 0.40 V,using a solar simulator (300 W) as the light source, and 0.1 M Na_2SO_4 as supporting electrolyte.

By imposing a (reverse) bias potential, the minority carriers are driven to the film/solution interface and the majority carriers to the rear (ohmic) contact. In the case of $BiVO_4$ (*n* – type semiconductor),[110] the minority carriers are holes. The photogenerated holes oxidize solution species (adsorbed H_2O molecules or OH^- groups); the sulfate species are inert from a redox perspective (at least at the potentials considered in Figures 3.13 and 3.14). The photocurrents in Figures 3.13 and 3.14 are *anodic* consistent with the *n* – type semiconductor behavior of $BiVO_4$.

For each bias potential, the data are compared with those for the commercial benchmark sample. At the more positive bias potential, carrier recombination is minimized and the photoanodic currents are ~ 22 times higher for BV2 relative to the commercial benchmark attesting to the superior photoactivity of the CS sample. The gradual decay in the photocurrent envelope as a function of time in Figure 3.13(a) presumably arises from mass transport limitations. On the other hand, the photocurrents in Figure 3.13(b) for the commercial $BiVO_4$ sample have not reached high enough level to "feel" the mass transport limitation.

At a lower bias potential, trap – mediated recombination prevails, diagnosed by the "spiked" photocurrent – time profiles for the commercial $BiVO_4$ sample in Figure 3.14(b). In contrast, these spikes are absent for BV2 at the same bias potential (Figure 3.14(a)) reflecting the better surface quality of the CS method. The implications of the photoelectrochemical data in Figures 3.13 and 3.14 are that CS $BiVO_4$ would make good photo anode materials for solar water oxidation. Thus these materials are not only applicable for environmental photoremediation (Figure 3.11), but are also useful for solar water splitting.

3.4 Electrosynthesis of $BiVO_4$

In addition to the samples prepared by combustion synthesis, $BiVO_4$ was also prepared by an electrosynthesis procedure. $BiVO_4$ electrodes were prepared by first electrodepositing a Bi film on a Pt substrate, and then stripping the film anodically in a vanadium solution to generate Bi^{3+} and subsequent precipitation (in situ) to yield $BiVO_4$ on the substrate. The electrodeposition scheme is depicted in Figure 3.15.

3.4.1 Optimization and Miscellaneous Aspects

The rich vanadium solution chemistry, particularly for V^{5+} with the presence of at least VO_2^+, VO_3^- (metavanadate), and VO_4^{3-} (orthovanadate) species and not counting other numerous protonated complexes, prompted us to evaluate the salts: NH_4VO_3, V_2O_5, or Na_3VO_4 as the vanadium precursor. Initial experiments were carried out varying the solution pH (1 to 14) and the salt concentration (0.01 to 0.04 M), and keeping the Bi^{3+} concentration constant at 0.02 M in all the cases. Electrodeposition of bismuth films was performed potentiostatically (0.2 V, 50 s) in a solution containing 0.02 M $BiCl_3$ + 0.5 M KBr in 1 M HCl, according to a reported procedure,[111] and with a total charge in the 140–160 mC/cm^2 range. Previous studies on electrodeposition and stripping of Bi in aqueous media [112] are also noted. The Bi film stripping potential (see Figure 3.15b) was +1.7 V in all the cases considered below. The optimal conditions for $BiVO_4$ formation (with little contamination from Bi_2O_3) were found out to be as follows: 0.02 M NH_4VO_3 as the vanadium precursor and pH 7 for the reaction medium. All the experiments were carried out under these conditions. Under these conditions, the VO_3^- species hydrolyzes to VO_4^{3-}, according to equation 3.16, followed by in situ precipitation with Bi^{3+} to generate $BiVO_4$ at the substrate – electrolyte interface.

$$VO_3^- + H_2O \Leftrightarrow VO_4^{3-} + 2H^+ \qquad (3.16)$$

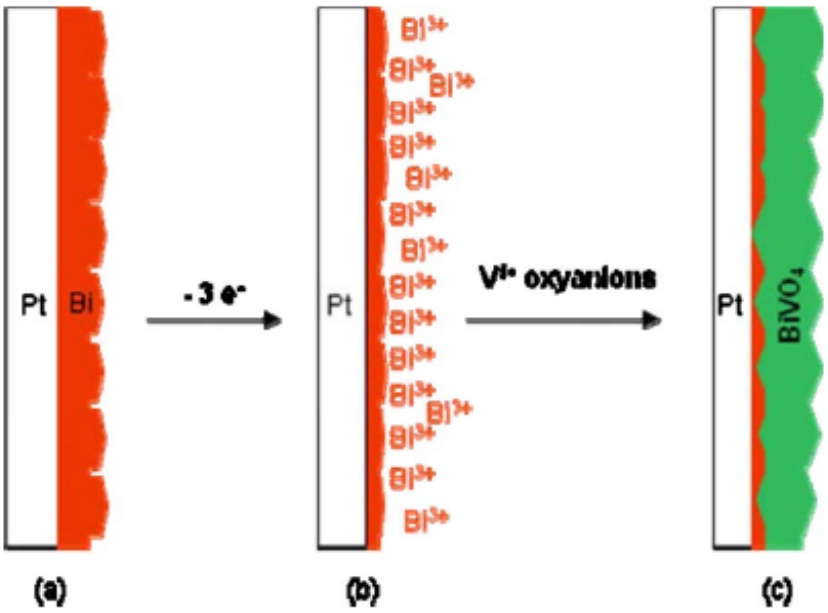

Figure 3.15 Two step electrosynthesis strategy for the electrosynthesis of $BiVO_4$ photoelectrodes.

Considering the presence of minor amounts of Bi_2O_3 in addition to $BiVO_4$ component, the terminology "Bi–V–O," was used for the electrodeposited films. The use of basic pH values promotes the formation of Bi_2O_3. (The formation of V_2O_5 can be ruled out on the basis of arguments presented later and the XPS data).

3.4.2 Sample Characterization

The morphological changes occurring on an electrodeposited Bi film leading to the formation of a Bi-V-O film are shown in Figure 3.15. The representative SEM images for the changes undergone for the NH_4VO_3 (pH 7 case) are shown in Figure 3.16. The characteristic nanostructure of the electrosynthesized Bi film consisting of flowerlike assemblies of platelets (Figure 3.16a) is converted to cotton-like entities (puffing up from the thin Bi platelets) after the bismuth oxidation in the NH_4VO_3 solution (Figure 3.16b). These cotton-like structures are interpreted to be diagnostic of a high hygroscopic property for the formed film, which is known for

$BiVO_4$.[113] Only after annealing at temperatures of 450℃ did the shrinkage of the cotton-like entities occur (inset in Figure 3.16b) as the adsorbed water is then released in the 250–450℃ range.[113]

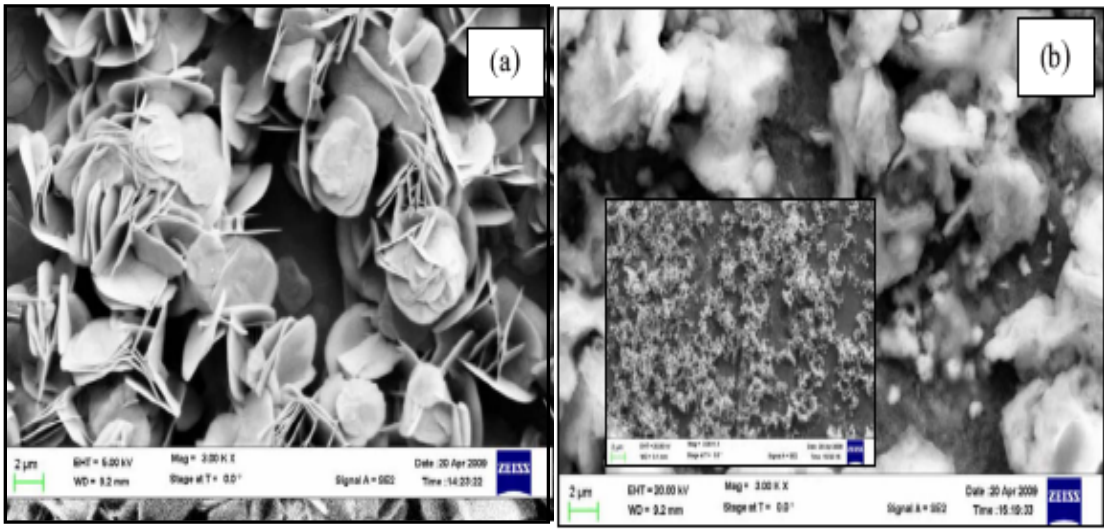

Figure 3.16 SEM images for an electrodeposited Bi film (a) before and (b) after oxidative stripping in the presence of a vanadium precursor. Inset in (b) contains an SEM image of a postannealed Bi–V–O film (450℃, 2 h. The "as prepared" Bi–V–O film was formed by electrogeneration of Bi^{3+} in 0.02 M NH_4VO_3, pH 7.

In the current study, the $BiVO_4$ films were used "as prepared," i.e., without a thermal treatment because their high affinity for water is beneficial to the photocatalytic activity and in the application of these films for water photoxidation.

Images of the SEM – EDX studies (not shown here) on the $BiVO_4$ film showed overlapping of the Bi and V signals throughout the film. This trend is consistent with $BiVO_4$ formation by the two step process, first by forming Bi^{3+} at the electrode surface and then its subsequent "quenching" by reaction with VO_4^{3-} solution species. Control experiments carried out by omitting the first step (i.e., if an oxidation potential was applied in the absence of a predeposited Bi film) indicated that no film was formed by the electrosynthesis technique.

Figure 3.17A contains high resolution XPS spectra for a representative $BiVO_4$ film in the Bi 4f [Figure 3.17A (a)], V 2p [Fig. 3.17A (b)], and O 1s [Figure 3.17A (c)] binding energy regions. The corresponding spectra for a film prepared from an authentic $BiVO_4$ powder sample (see the Experimental section) are included in Figure 3.17B for comparison.

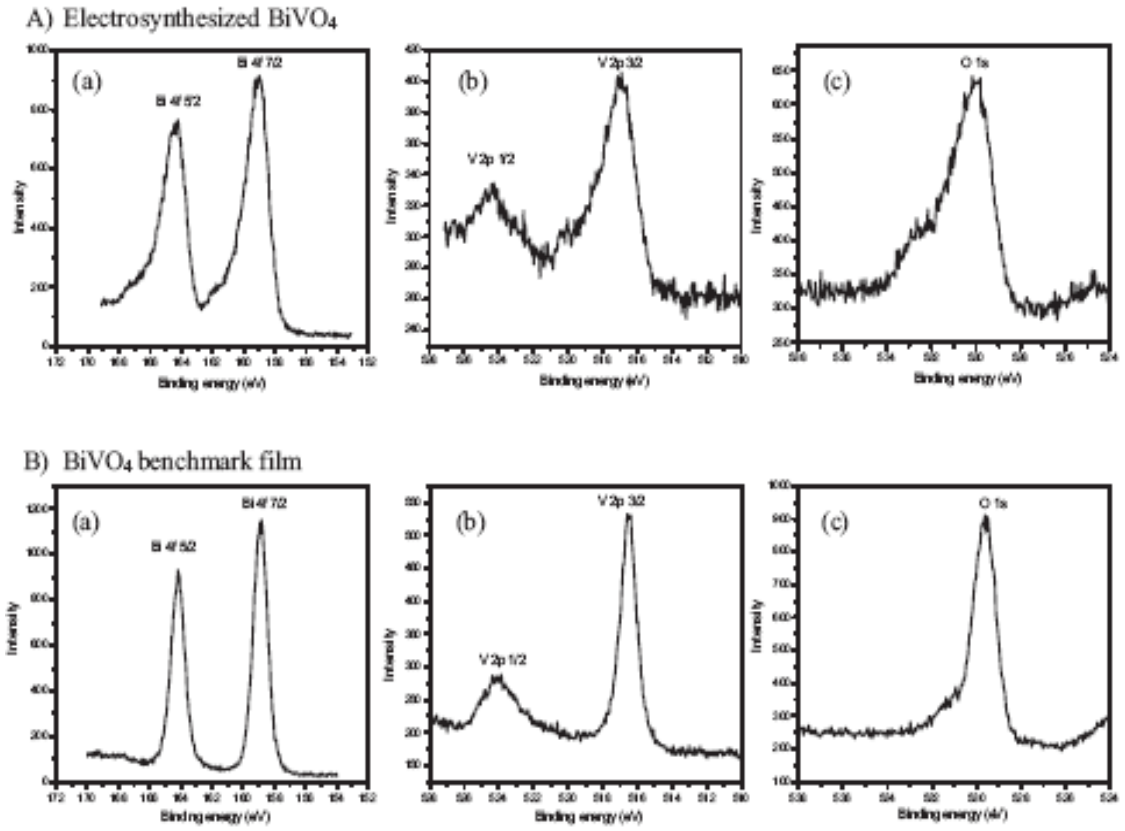

Figure 3.17 High resolution XPS analyses of (A) (a) Bi 4f, (b) V 2p, and (c) O 1s for $BiVO_4$ films prepared from $BiCl_3/NH_4VO_3$, pH 7 and (B) corresponding spectra for a film prepared from authentic $BiVO_4$ powder.

Both samples in Figure 3.17 show the spin orbit splitting for Bi $4f_{7/2}$ and Bi $4f_{5/2}$ and for V $2p_{1/2}$ and V $2p_{3/2}$. These spectral data are in good accord with those reported for $BiVO_4$ films prepared by other techniques.[39,41] Importantly, the Bi $4f_{7/2}$ and Bi $4f_{5/2}$ peaks appear at higher energies than those for the metallic Bi located at 156.8 and 162.2 eV, respectively.[114] The V $2p_{3/2}$

peak was found at 516.4 eV in the benchmark sample and slightly shifted to a higher energy for the electrodeposited $BiVO_4$ film [see Figure 3.17A(b) and 3.17B(b)]. As the reported position for vanadium as V_2O_5 is 516.6 eV,[115] considering the O 1s XPS data is necessary to ascertain the chemical identity of the surface composition in the electrodeposited films. In the oxygen binding energy region [(Figure 3.17A(c) and 3.17B(c)], the most dominant O 1s peak at 529.6 eV and assigned to oxygen in a $BiVO_4$ lattice environment[41] is clearly seen in all our XPS spectra. For the electrosynthesized samples, a shoulder at 531.7 eV, corresponding to OH^- groups,[114] is more pronounced than that in the benchmark film. Similarly, a peak at 533.0 eV is associated with oxygen in water[116] and is present in the electrosynthesized samples consistent with their aqueous preparative history and with the notion that these films contain adsorbed water. This is also expected from the high hydrophilicity of $BiVO_4$.

Coincidentally, the O 1s peak at 529.6 eV can also be assigned to oxygen in a V_2O_5 lattice environment;[117] thus, the presence of surface V_2O_5 "contaminant" cannot be ruled out yet. However, the XPS signals for the three element components (Bi, V, and O) are located at the correct energies for $BiVO_4$, and the surface atomic ratio of V to Bi is lower than the stoichiometric ratio in all the cases, including for the benchmark $BiVO_4$ where the V/Bi ratio is only 0.6. The V/Bi ratio in the electrodeposited $BiVO_4$ films was also close to this value for several films tested. These findings rule out V_2O_5 as a component in the surface composition of the films as otherwise they would have a V/Bi ratio > 1. If any oxide was formed during the stripping of Bi^0 to Bi^{3+} in the V^{5+} solution, it is Bi_2O_3. Bi_2O_3 formation is enhanced at basic pH values because of the competition of OH^- species present at high concentrations relative to the V^{5+} precursor species for reaction with the freshly electrogenerated Bi^{3+}. Therefore, our surface analysis data indicate a thin Bi-rich surface layer to be always present atop the $BiVO_4$ films. The commercial $BiVO_4$ powder also shares this surface compositional feature, presumably stemming from its preparative history. A Bi-rich surface layer was also reported by previous authors for $BiVO_4$ formed by a metallorganic decomposition route.[41] This layer serves as a useful film photocorrosion protection role in photoelectrochemical scenarios, as discussed in the next section.

3.5 Photoelectrochemical Behavior

Figure 3.18a contains a representative photocurrent/potential (i_{ph}/V) profile under chopped visible light irradiation (0.1 Hz) for a $BiVO_4$ film prepared in the NH_4VO_3 (pH 7) precursor solution. These photoelectrochemical data were obtained in neutral media with Na_2SO_4 as a supporting electrolyte to check the performance of the electrodeposited film for water photooxidation. At pH ≥ 7, anodic i_{ph}/V profiles diagnostic of the *n* – type $BiVO_4$ are seen in the potential range extending from ~ 0.1 to 1.4 V, which also agree well with the data reported earlier for $BiVO_4$ films prepared by other routes.[41,117] The i_{ph} onset potential at ~ 0.1 V is also as expected for the conduction band position of $BiVO_4$, corroborating its *n* – type semiconductor behavior.

The photoaction spectral data further confirmed the identity of the electrodeposited $BiVO_4$ films. One such spectrum is shown in Figure 3.18b. The medium was the same as in the experiment considered in Figure 3.18a, and therefore, the data pertain to the photooxidation of water. The good photoresponse from 350 to 580 nm yields a characteristic energy bandgap (E_g) of 2.14 eV for $BiVO_4$. The inset in Figure 3.18b contains the graphical analysis of the photoaction spectral data leading to the above E_g value.

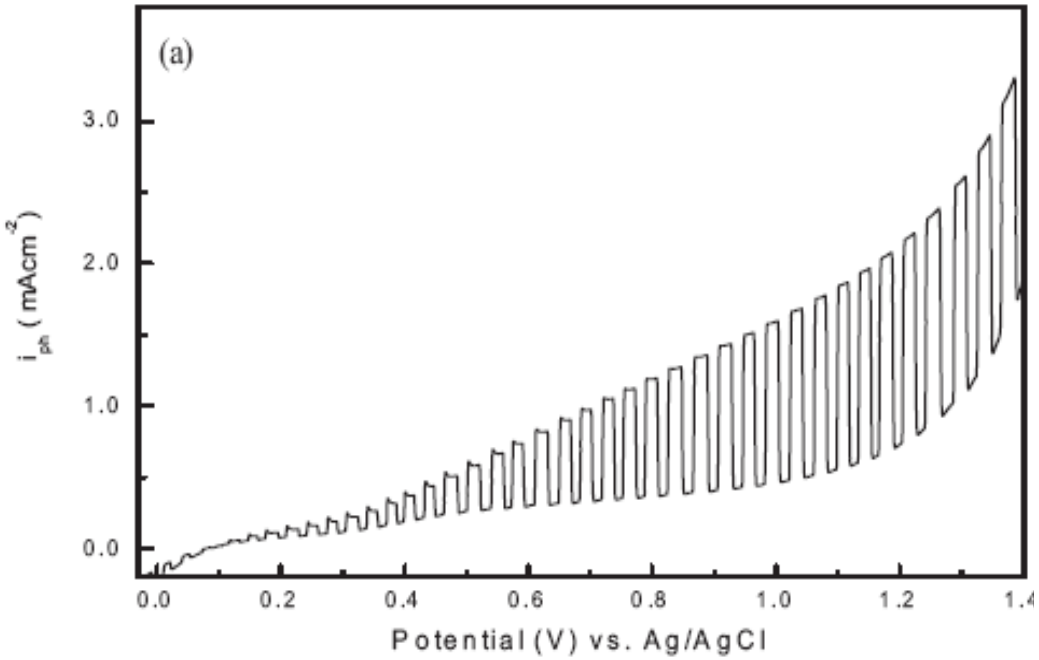

Figure 3.18(a) Photovoltammograms for a $BiVO_4$ photoelectrode film prepared from $BiCl_3/NH_4VO_3$ at pH 7 and measured in 0.1 M Na_2SO_4.

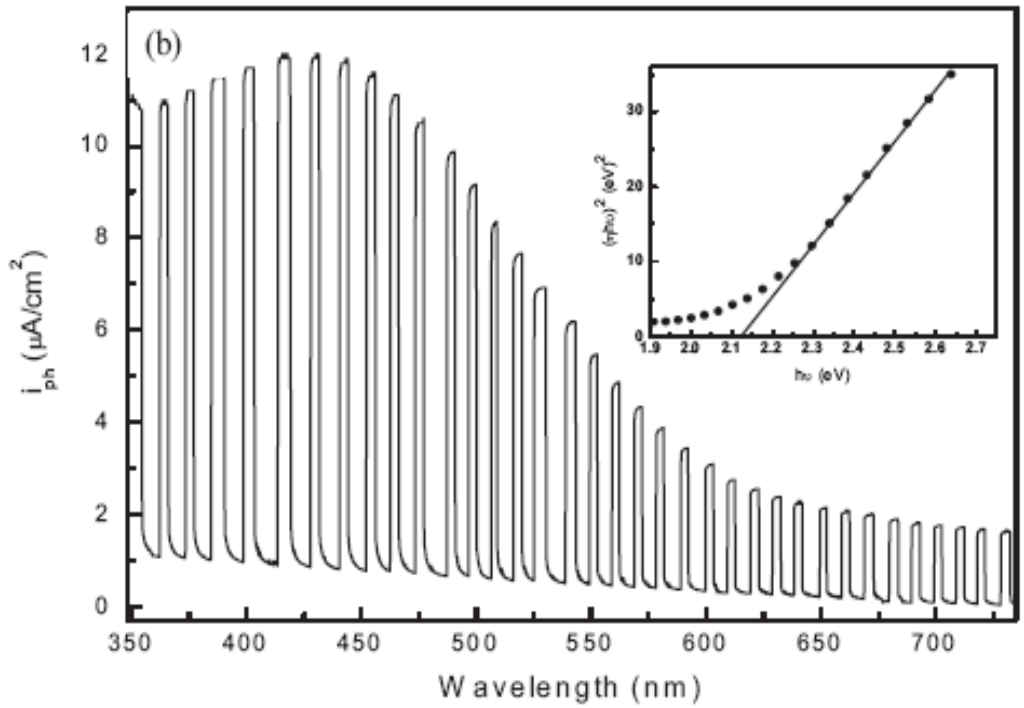

Figure 3.18(b) Corresponding photocurrent action spectrum recorded at 0.7 V. The inset contains analysis of these data according to the Butler method in Ref. 120. η is the quantum yield, and $h\nu$ is the photon energy (see also Ref. 120).

The analysis described by a previous author[118] on the basis of the Gärtner mode[119] was used here, and the assumption of a direct bandgap is inherent in the plot contained in Figure. 3.18b. A direct gap was also assumed by previous authors for their analysis of photoelectrochemical data on $BiVO_4$ thin films prepared by a chemical solution approach.[117] The rationalization for a direct gap is available from the first principles electronic structure (density functional theory or DFT) calculations for $BiVO_4$.[25] Incidentally, the E_g value obtained above is in good accord with the value (2.1 eV) obtained from the DFT calculations for $BiVO_4$ in the monoclinic (scheelite) form.[120] This structure modification and bandgap value are also generally found for $BiVO_4$ films and powders prepared by other methods.[28,34,37,40,41,49,55] The photoelectrochemical data were stable over several minutes, indicating that these films are reasonably stable toward anodic photocorrosion. This work was developed as a proof-of-concept study, and long term stability tests need to be carried out to assess the stability of the prepared films.

3.6 Solution Combustion Synthesis of $AgBiW_2O_8$

Silver bismuth tungstate ($AgBiW_2O_8$) was another oxide semiconductor prepared by combustion synthesis for the first time, and tested for its photocatalytic ability to degrade methyl orange (MO), similar to the studies with $BiVO_4$. The activity was compared to a sample of $AgBiW_2O_8$ prepared by a solid state reaction.[76] In addition to photodegradation of MO, another crucial aspect was to demonstrate a proof-of-concept for photogeneration of syngas using $AgBiW_2O_8$ particles.

3.6.1 Crystal Structure Modeling Considerations

To date, very little information is available on the exact crystal structure of $AgBiW_2O_8$. The only structure of $AgBiW_2O_8$ we are aware of so far is the predicted monoclinic structure from a previous study,[76] which was speculated based on studies on three different oxides Ag_2WO_4, $Bi_2W_2O_9$, and $AgBiW_2O_8$. As mentioned earlier, the electronic band structure calculations were

performed by Dr. Huda and his group (Section 2.5). The results and the following discussion on the crystal structure modeling and the band structure calculations have been included in the present work to facilitate a better understanding of the band structure of $AgBiW_2O_8$.

Since the monoclinic structure was identified in a previous study,[76] three possible monoclinic structures, wolframite, scheelite, and fergusonite, were considered for the crystal structure determination of $AgBiW_2O_8$. Figure 3.19 below shows the atomic arrangements for the three crystal systems of $AgBiW_2O_8$. The calculations considered several possible relative sites for Ag and Bi, and the lowest energy ones were chosen for the final calculations.

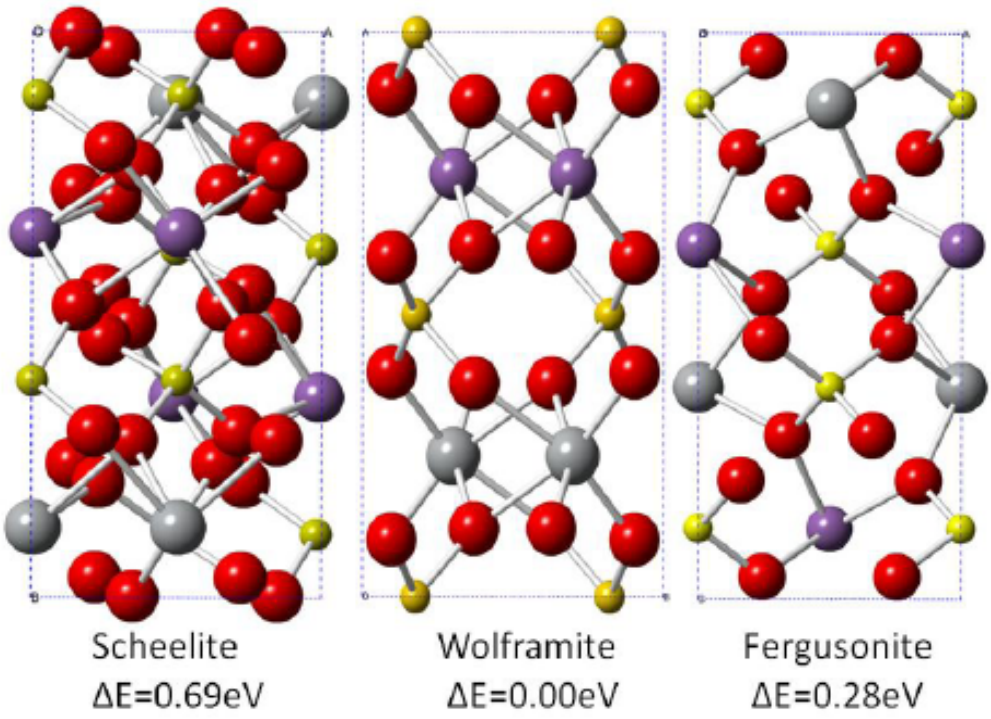

Figure 3.19 Structures of three possible lattices for $AgBiW_2O_8$ and their relative energy differences with respect to the wolframite structure. Purple, gray, yellow and red atoms are Bi, Ag, W and O, respectively.

The scheelite structure is usually characterized by a tetragonal unit cell, but the monoclinic $CaWO_4$-d structure which is distorted from tetragonal symmetry appears to be energetically favored. The wolframite and scheelite structures are closely related and transform into one another depending on the cationic (R^{3+}) radii.[121] The higher atomic density in scheelite structure is due to the fact that the supercell is double the size than in wolframite or fergusonite. On the other hand, fergusonite, another distorted scheelite structure,[122,123] also has a monoclinic unit cell lattice. Both the fergusonite and wolframite supercells contain 24 atoms (two formula units) each, whereas the scheelite supercell contains a total of 48 atoms (four formula units). From DFT calculations, the wolframite structure (space group *P 2/c*; No. 13) was found to be the most stable form with the lowest energy in terms of the possible relative sites for Ag and Bi atoms, while the scheelite and fergusonite structures were 0.69 eV and 0.28 eV higher in energy, respectively. This finding was in contrast to the earlier result which predicted a *I 2/m* space group (No. 12) for $AgBiW_2O_8$.[76] The rationalization for the wolframite structure was provided on the following basis: The mineral structure for *I 2/m* symmetry has a hollendite structure, which cannot accommodate a layered Ag-Bi-W-O network, and the bonding coordination also cannot accommodate a W atom in this structure. Aluminum tungstate (space group *C 2/m* No. 12) was also evaluated, but was found to be less stable than the wolframite structure. No other structure with *I 2/m* symmetry was found to support the Ag-Bi-W-O network.

Wolframite belongs to the monoclinic space group *P 2/c* (No.13, Z=2)[124] as in the AWO_4 (A = Cd, Mn, Fe) family. In this structure, each W atom is coordinated to six O atoms, forming octahedral WO_6 structural units (Figure 3.19). Two distinct oxygen atoms (O1 and O2) occupy two different sites in this structure: type O1 is connected to one tungsten atom with a shorter bond length and to two *A* atoms with larger bond lengths, and type O2 is bonded to two different W atoms and to one A atom. Thus the overall structure is made up of hexagonally close-packed oxygen with certain octahedral sites occupied by A and W cations.[125] For the present calculations, a double unit cell of wolframite was used where the A-sites were replaced by Ag^+ and Bi^{3+} selectively.

3.6.2 Electronic Structure Calculations

Figure 3.20 shows the band structure of the wolframite $AgBiW_2O_8$ structure (calculated by Dr. Huda's group) along the special symmetry points in the Brillouin zone. The calculations predicted a minimum energy band gap of 1.96 eV, which is an indirect gap, where the conduction band minimum occurs between the D and Z points. The existence of the long tails of absorption curves for both SCS and SSR samples (diffuse reflectance data) indicated an indirect band gap via (see diffuse reflectance data), in addition to the main optical transition. The minimum direct gap of 2.02 eV was shown to occur between Y and E points. Both of these gaps are smaller than the experimentally measured band gaps of 2.75 eV. However, this underestimation of energy band gaps is generally a typical feature of DFT calculations.

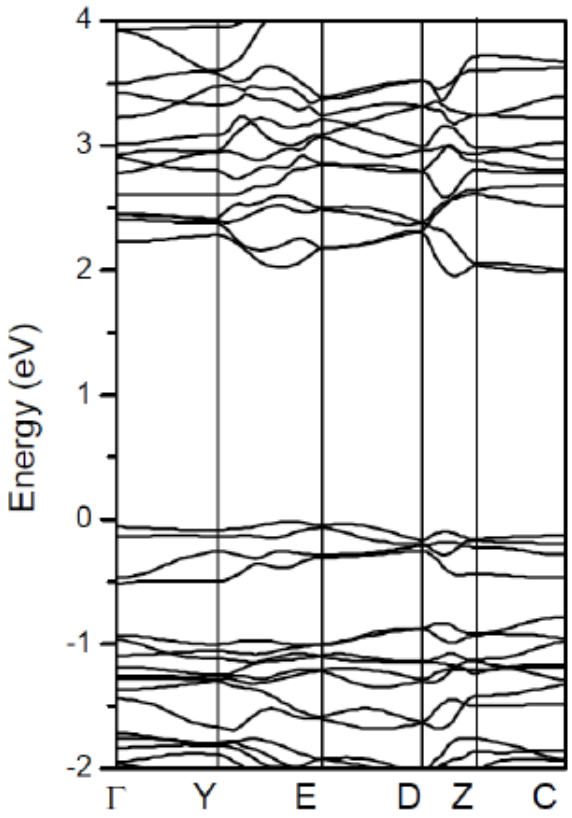

Figure 3.20 Calculated band structure of wolframite $AgBiW_2O_8$. Here 0 eV refers to the highest occupied band (Fermi energy).

From the band structure calculations, it was shown that the valence band is divided into two regions. The upper region was from the Fermi level (the highest occupied level) to – 0.5 eV, and the second region starts from – 0.8eV. A gap of around 0.3 eV exists between these two regions. The less dispersive bands along the Z to C points near the band gap indicated that electron or hole transport across the oxygen layers (along the vertical direction in Figure 3.20) was not very likely due to the higher electron effective mass in that direction. Hence, electronic conduction was more likely to happen along the 2-D horizontal planes. The two relatively higher dispersion regions (Y to E and D to Z in Figure 3.20) in the conduction band minima were due to the presence of Bi-p levels, which also facilitates higher electron mobility relative to that of the holes.

The contribution from Ag 4d to the upper part of the valence band could be clearly seen from the partial density-of-states (p-DOS) plot for $AgBiW_2O_8$ (Figure 3.21). Even at the topmost part of the valence band the contribution from O-p is not significant. No contribution from the Bi-s was observed, unlike the case of $BiVO_4$ where Bi-s had an anti-bonding contribution at the top of the valence band.[25] The contributions of O-p and W-d around the band edges are similar to that of the monoclinic WO_3 parent structure.[126]

However, in $AgBiW_2O_8$, the presence of the Ag-d level "modulates" the valence band, and is also responsible for the uplift of the valence band edge compared to the WO_3 case. Bi-p was found to contribute to the conduction band minimum, though the lower part of the conduction band is dominated by W-d levels. Even though the O 2p and Bi 6p orbital contributions are small around both the band edges, their presence would facilitate favorable p-d optical transitions.

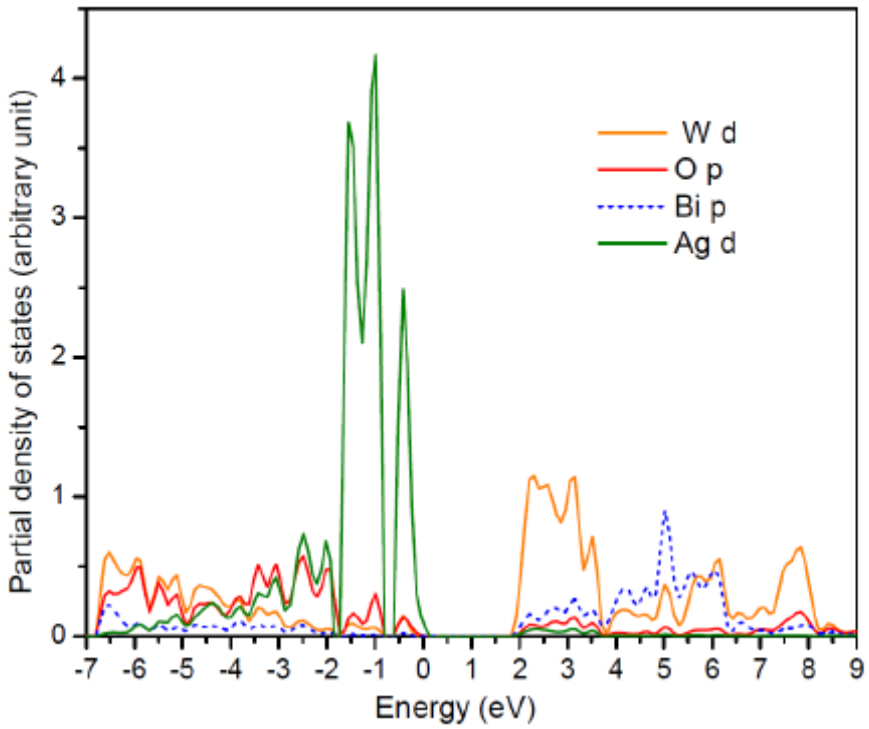

Figure 3.21 Calculated partial density of states for wolframite $AgBiW_2O_8$. Here 0 eV refers to the highest occupied band (Fermi energy).

3.6.3 Sample Characterization

The powder XRD patterns of the SCS and SSR samples are shown in Figure 3.22 and show a match between both the samples. Figure 3.22 also contains the designation of the peaks to the corresponding space groups analyzed from the software. A vast majority of XRD peaks are indexed to *P2/c* (group 13) in agreement with the theoretical prediction (Section 3.6.1), while only a few peaks are related to the monoclinic space groups *P2/m* and *P21/n*. The d-spacing corresponding to the most intense peak (at 2θ = 27.63°) was computed 3.1150 Å. The diffraction peaks for the SCS sample are appreciably broadened relative to the SSR counterpart. The peak broadening can only be attributed to the different particle size for the two samples, since both samples have comparable crystallinity. Accordingly, the average particle size was found to be ~6 nm for the SCS powder, and ~30 nm for the SSR powder, as calculated by the Scherrer equation.[88]

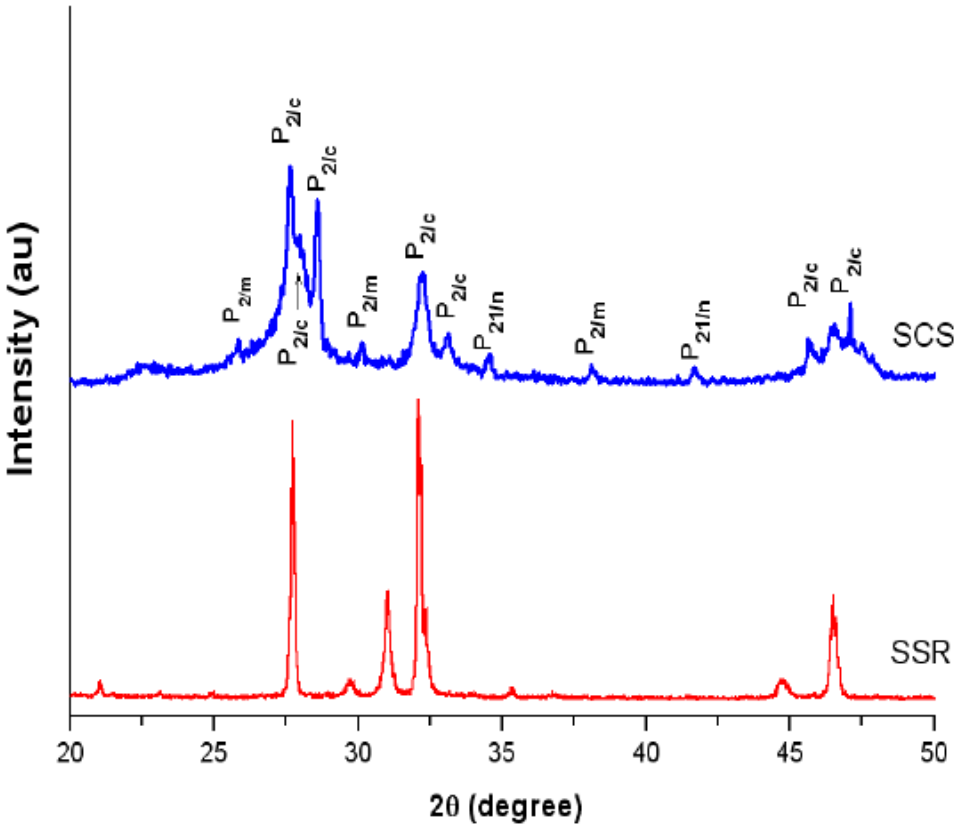

Figure 3.22 XRD spectra of the combustion synthesized (CS) and solid state (SSR) synthesized $AgBiW_2O_8$.

Consistent with the smaller particle size, the SCS samples also have a higher surface area (by an order of magnitude) relative to the SSR counterpart. Table 3.3 shows a comparison of the BET surface area values of the SCS and the SSR samples. It is also evident from these data that the SSR sample prepared in this work has a somewhat higher surface area than that quoted in a previous study. The superior dispersion of the SCS sample relative to the SSR counterpart, is entirely consistent with the feature that the high reaction temperatures attained in solution combustion synthesis,[2,14] result in a finely dispersed and porous morphology for the synthesized product. This is all the more desirable given that solution combustion synthesis yields the product in minutes as opposed to the several hours-long synthesis times spanned in solid-state reaction routes.

Table 3.3. Comparison of surface area of $AgBiW_2O_8$ nanoparticles prepared by solution combustion synthesis and solid-state reaction

Photocatalyst	Micropore Area cm^2	External Surface Area cm^2	BET Surface Area $m^2\ g^{-1}$	Comment
SCS-$AgBiW_2O_8$	5.488	28.938	34.436	This work
SSR-$AgBiW_2O_8$	0.136	0.406	0.542	This work
SSR-$AgBiW_2O_8$	-	-	0.29	Ref. 7

Representative TEM images of the SCS–$AgBiW_2O_8$ are shown in Figure 3.23. The images show mainly spherical nanocrystalline particles in 5 – 10 nm range, which are in accord with the particle size calculated by the Scherrer equation. It is worth mentioning that the samples were obtained by solution combustion synthesis even without a post annealing treatment step. This is yet another crucial advantage with this synthesis approach from an energy input perspective to add to its high time efficiency, as mentioned in the introduction section.

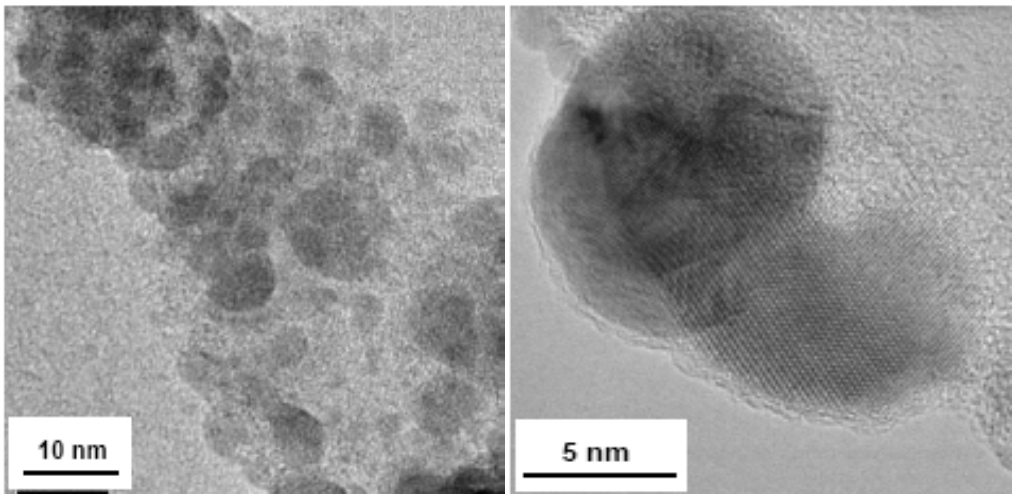

Figure 3.23 TEM images of solution combustion synthesized $AgBiW_2O_8$.

Figures 3.24 (a) and 3.24 (b) contain the UV-visible diffuse reflectance data on the SCS and SSR synthesized $AgBiW_2O_8$ samples, respectively. The absorption plots in the inset show an extension of the absorption edge into the visible region. The band gap (E_g) values of the powders, estimated from the Tauc plots of the square root of the Kubelka–Munk function versus the photon energy, [90] were found to be 2.74 eV for the SCS sample, and 2.77 eV for the SSR sample. These values are in very good agreement with a the value (2.75 eV) reported for this complex oxide in a previous study on solid state synthesis.[76] The long wavelength absorption tail (Figure 3.24 insets) is not attributed to the surface plasmon absorption of Ag metal (490 – 530 nm), since Ag^0 was not detected on the surface of the $AgBiW_2O_8$ nanoparticles, which is shown from the XPS analysis described in the following section.

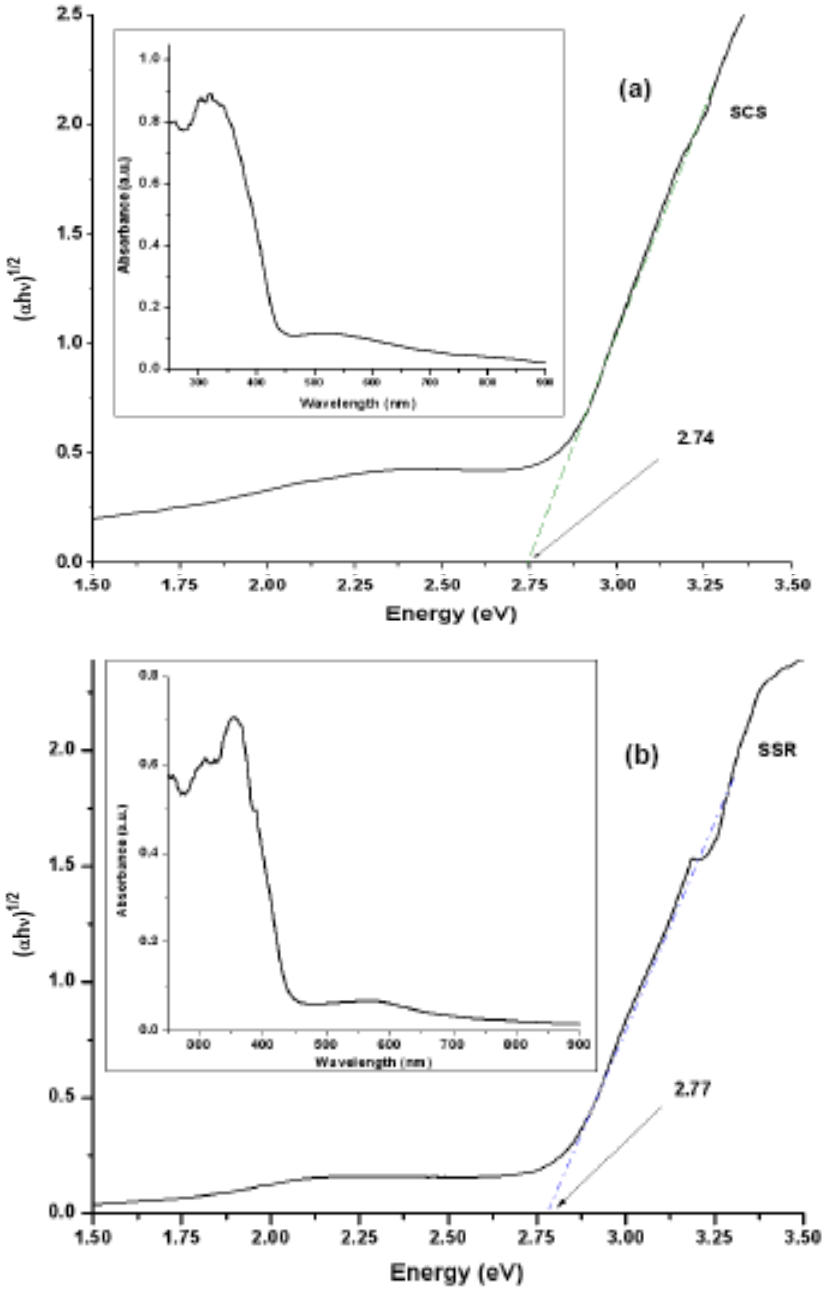

Figure 3.24 Tauc plots for (a) SCS-$AgBiW_2O_8$ and (b) SSR-$AgBiW_2O_8$. Insets contain the percent transmittance data for both samples.

Figure 3.25 contains the high-resolution XPS data for the SCS–$AgBiW_2O_8$ samples in the binding energy regimes (3d for Ag, 4f for Bi and W, and 1s for O) characteristic of the four elements in the compound. The Pt 4f signals for the Pt modified $AgBiW_2O_8$ are also shown in the figure.

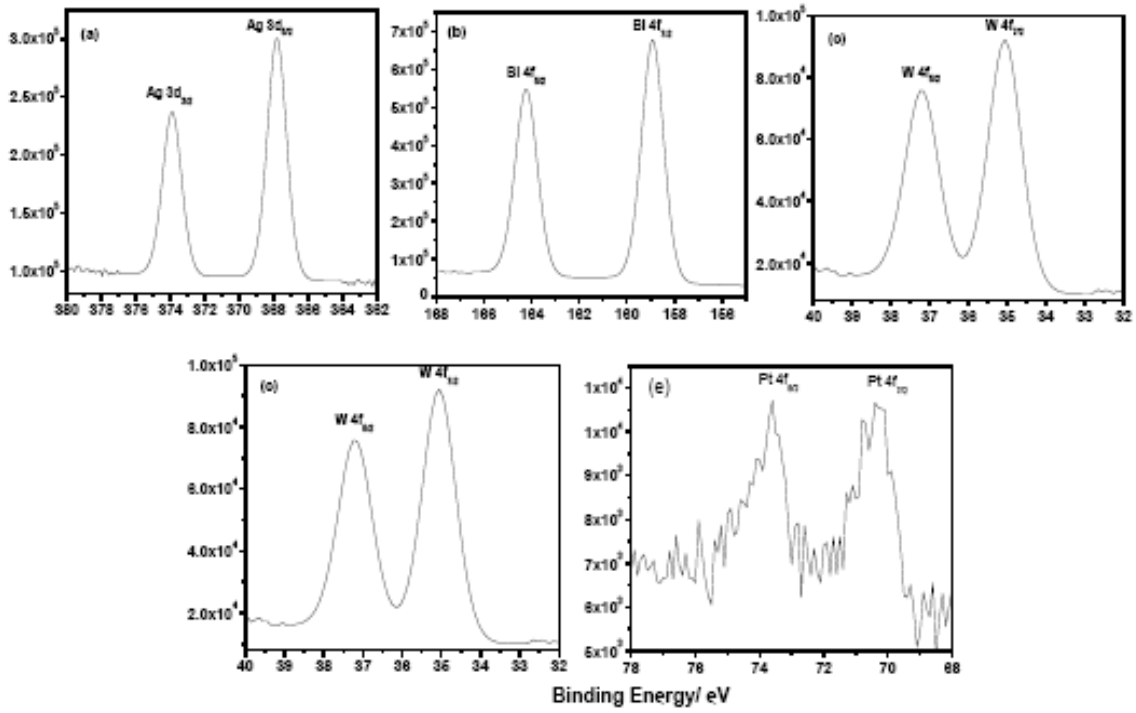

Figure 3.25 High-resolution core level X-ray photoelectron spectra (ordinates in the spectra in counts per second) in the (a) Ag 3d, (b) Bi 4f, (c) W 4f, (d) O 1s and (e) Pt 4f binding energy regimes for SCS-$AgBiW_2O_8$ (a-d) and Pt-modified SCS-$AgBiW_2O_8$.

.

The XPS signals for the metal components are split due to spin-orbit coupling. The signals are located at 387.9 eV for silver (Ag $3d_{5/2}$), at 158.9 eV for bismuth (Bi $4f_{5/2}$) and at 35.1 eV for tungsten (W $4f_{7/2}$) respectively.[114] These respective peaks for Ag, Bi and W are associated with Ag^+ or Ag^{2+} in an oxide structure, with Bi^{3+} also surrounded by oxygen neighbors (such as in Bi_2O_3, Bi_2O_4), and with W^{6+} in a hexagonal oxygen-bonded structure (such as WO_3, H_2WO_4).[127] The XPS data are in accord with a layered structure for $AgBiW_2O_8$ composed of WO_6 octahedral sheets interleaved with Bi-O-Bi layers and AgO_x polyhedra. Importantly, the XPS data also

confirm that there is no *free* metal formation (i.e., Ag^0, Bi^0) during SCS. For instance, in the Bi binding energy regime, it must be noted that the Bi $4f_{7/2}$ and Bi $4f_{5/2}$ signals in Figure 3.25b are located at 158.95 and 164.2 eV; far higher in energy than the characteristic peaks for *metallic* Bi located at 156.8 eV and 162.2 eV respectively.[127] Similar considerations apply for silver peaks as well.[127]

In the O 1s binding energy regime, the peak at 529.9 eV is in good agreement with that similarly reported for a bismuth tungstate structure[127] and at variance with that for WO_3 at 530.5 eV.[128] The other O 1s peak at 532.1 eV is assignable to residual water bound to the oxide particles and also to water molecules adsorbed on the sample surface.[129]

Furthermore, the XPS profiles of the powder samples after the dye degradation and syngas photogeneration reactions did not show any shift in the binding energy, which is an indication that the composition of the sample was stable after photocatalysis.

3.7 Photocatalytic Behavior of $AgBiW_2O_8$

3.7.1 Photodegradation of Methyl Orange

The photocatalytic activity of the CS and SSR powders was evaluated under visible light irradiation using methyl orange as a probe material. The results of MO photodegradation in the form of a concentration – time plot, are presented in Figure 3.26. The figure contains the degradation profiles as a function of time for the blank (no photocatalyst) case, and for the SCS– and SSR – $AgBiW_2O_8$ samples. The extent of photodegradation of MO was measured by the decrease in absorbance. The data were plotted taking the time at the start of light irradiation *i.e.,* after 30 min of adsorption in the dark, as the initial time.

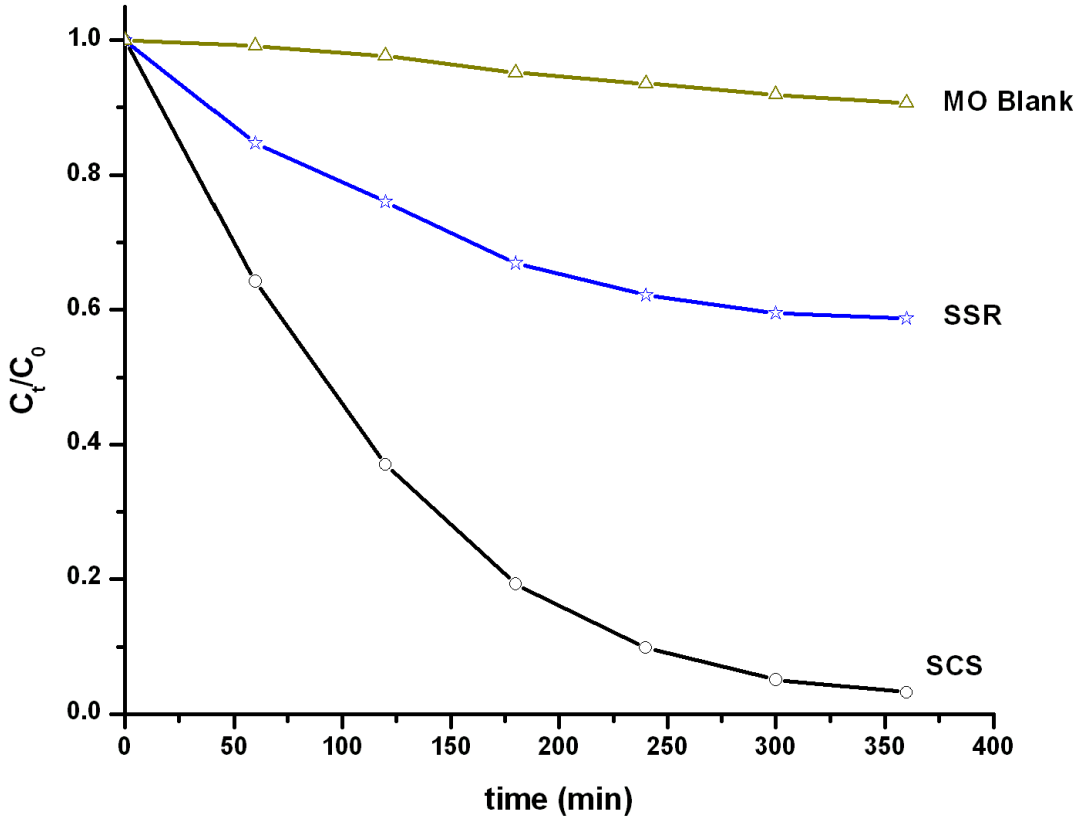

Figure 3.26 Comparison of methyl orange photodegradation profiles (fractional concentration vs irradiation time) for the blank case (no oxide photocatalyst) and for the two photocatalyst SCS– and SSR–$AgBiW_2O_8$ powders.

The results indicate the superior activity of the SCS sample over the SSR sample. For example, ~ 60% of the dye was degraded by the SCS sample in about 2 h, while the SSR sample showed a degradation of ~ 20 in the same time. The superior activity of the SCS sample is rooted in the morphological factors (Table 3.3), with a higher surface area for the SCS sample. It is known that smaller size and higher surface area increase the photocatalytic activity due to enhanced charge carrier photogeneration and separation.

The degradation profiles in Figure 3.26 indicate a pseudo first order kinetic rate for the photocatalysis reactions, and the data match well with the model of the pseudo first order kinetics

plotted in Figure 3.27. The solid line indicates the least squares linear fit for the kinetic data plotted as a dotted line with circles for data points.

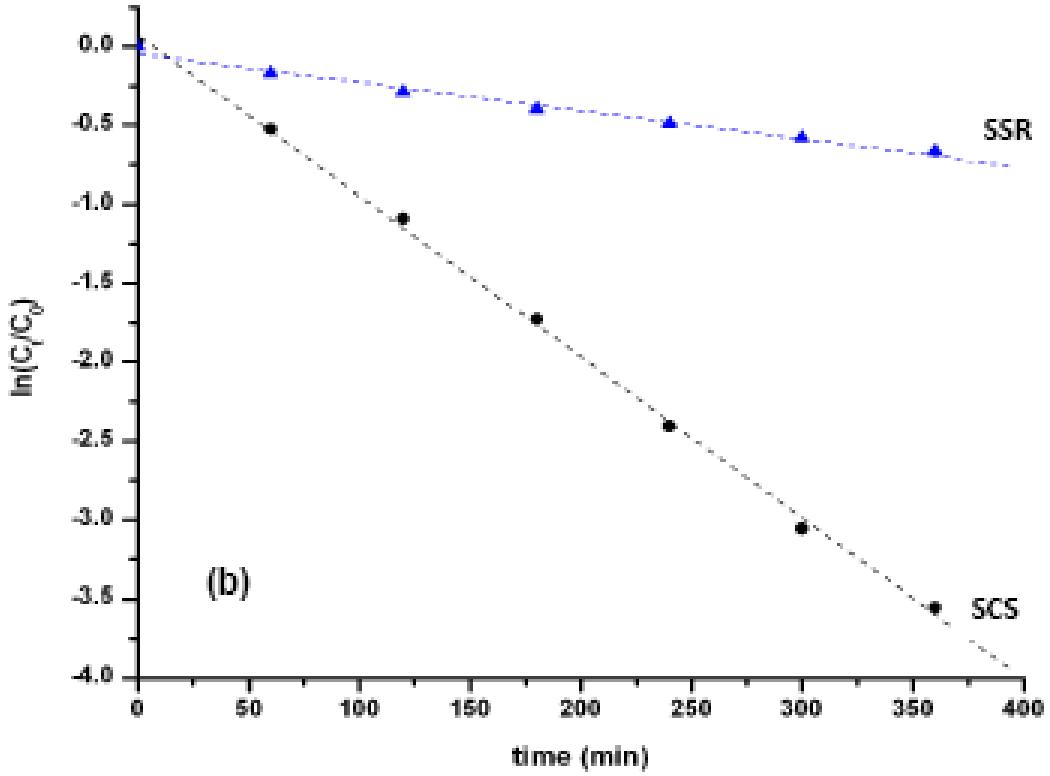

Figure 3.27 Kinetic data for the MO degradation profiles with the SCS– and SSR–$AgBiW_2O_8$.

The apparent rate constants calculated from the slopes of the lines were 0.0102 min^{-1} for the SCS sample and 0.0018 min^{-1} for the SSR sample. The rate was higher for the SCS nanoparticles when compared to the SSR reference, which is indicative of its better photocatalytic performance. This could be explained on the basis of the morphological differences between the two samples. The smaller size of the SCS particles leads to enhanced charge carrier generation and more effective separation of the photogenerated charge carriers, resulting in an enhanced degradation rate.

Similar to the case with $BiVO_4$, MO degradation is assumed to be by photocatalysis and photosensitization pathways.[47] Degradation by photolysis is negligible in this case, as evident from

the MO blank data in Figure 3.26. The possible degradation mechanism is outlined below by the following equations.

Photosensitization pathway

$$MO + h\nu \rightarrow MO^{*} \quad (3.18)$$
$$MO^{*} + ABW \rightarrow MO^{+\bullet} + ABW(e^{-}) \quad (3.19)$$
$$ABW(e^{-}) + O_2 \rightarrow O_2^{-\bullet} + ABW \quad (3.20)$$
$$ABW(e^{-}) + O_2^{-\bullet} + H^{+} \rightarrow H_2O_2 \quad (3.21)$$
$$H_2O_2 + e^{-} \rightarrow {}^{\bullet}OH + OH^{-} \quad (3.22)$$
$$MO + {}^{\bullet}OH \rightarrow\rightarrow CO_2 + H_2O \quad (3.23)$$

Photocatalysis pathway

$$ABW + h\nu \rightarrow ABW(e^{-}) + ABW(h^{+}) \quad (3.24)$$
$$MO + ABW(h^{+}) \rightarrow MO^{+\bullet} + ABW \quad (3.25)$$
$$H_2O + ABW(h^{+}) \rightarrow OH^{\bullet} + H^{+} + ABW \quad (3.26)$$
$$ABW(e^{-}) + O_2 \rightarrow O_2^{-\bullet} + ABW \quad (3.27)$$
$$ABW(e^{-}) + O_2^{-\bullet} + H^{+} \rightarrow H_2O_2 \quad (3.28)$$
$$H_2O_2 + e^{-} \rightarrow {}^{\bullet}OH + OH^{-} \quad (3.29)$$
$$MO + {}^{\bullet}OH \rightarrow\rightarrow CO_2 + H_2O \quad (3.30)$$

The role of O_2 is elucidated from equations (5) and (12). The conduction band electrons on the photocatalyst surface are scavenged by O_2 forming the superoxide radical ($O_2^{-\bullet}$). The superoxide radical forms $^{\bullet}OH$ species, which then causes the indirect degradation of MO.[47,108]

3.7.2. Photogeneration of syngas (CO +H_2) and Methane on Pt – modified $AgBiW_2O_8$

In addition to MO photodegradation, the SCS – $AgBiW_2O_8$ oxide was also studied for its ability to photogenerate syngas (CO + H_2) from formic acid (HCOOH) and methane (CH_4) from acetic acid (H_3CCOOH). This particular aspect was aimed towards developing a proof-of-concept study for generation of syngas from CO_2 reduction, CO_2 being generated in situ from formic acid degradation. For this purpose, the $AgBiW_2O_8$ nanoparticles were loaded with 1 mass percent Pt using a photodeposition procedure.[86] The color of the Pt – modified oxide particles changed

significantly from light yellow to a grayish hue as illustrated in Figure 3.28 below. The oxide powder was then loaded into a Pyrex photoreactor containing 200 ml of a deaerated solution (N_2 purged) of 0.1 M HCOOH or 0.1 M H_3CCOOH containing at a dose of 2 g/L. The UV lamp (400 W medium-pressure Hg arc) was turned on and the gaseous products evolved were analyzed by gas chromatography.

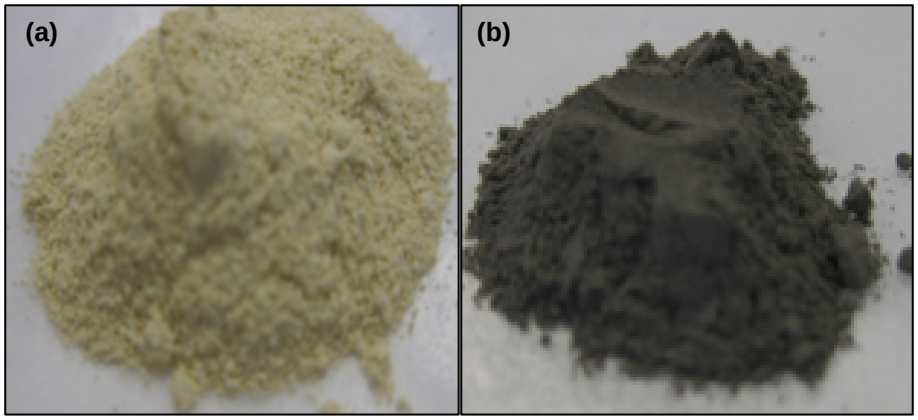

Figure 3.28 SCS–$AgBiW_2O_8$ powder (a) before and (b) after surface modification with 1 wt % Pt.

Figure 3.29 compares the temporal evolution of the gaseous products for formic acid (Figure 3.29a) and acetic acid (Figure 3.29b) as the electron donor. Control experiments carried out without photocatalyst powder did not yield any gaseous products indicating negligible acid photolysis. In addition, in the methane photogeneration experiments, another set of controls without initial Pt modification were also carried out, to assess the effect of Pt on H_2 and CH_4 photogeneration.

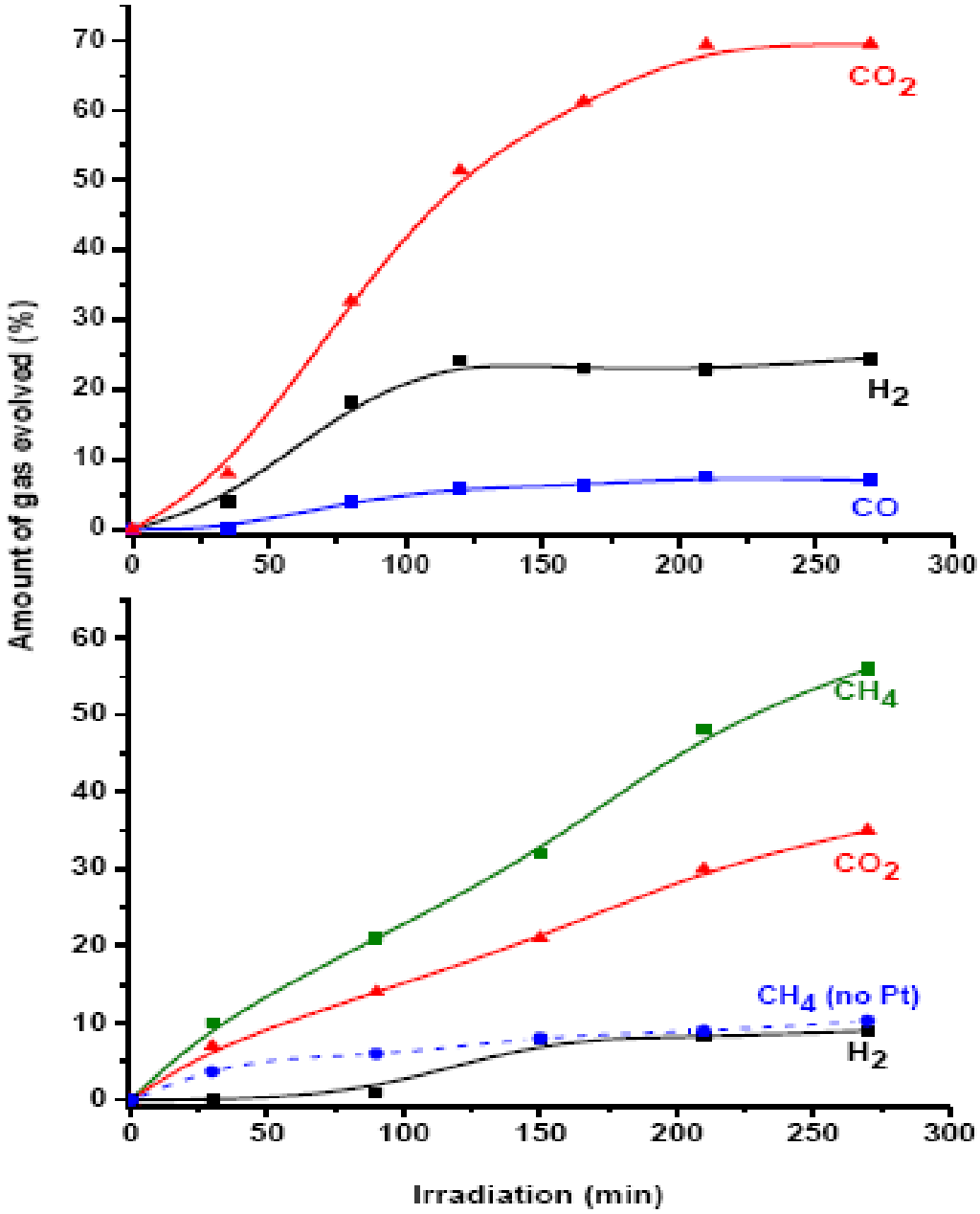

Figure 3.29 Temporal profiles of the gaseous products formed in the photocatalytic reaction of $AgBiW_2O_8$-Pt from (a) formic acid and (b) acetic acid as electron donors. Both systems were saturated with N_2.

A noticeable feature of this experiment is that HCOOH acts as an in situ precursor for CO_2 generation (Figure 3.29a). The advantages of using formate species is two fold. First, the direct electrochemical reduction of CO_2 in aqueous media is difficult due to the low partial pressure of CO_2 in the atmosphere (3.9×10^{-4} atm) and by its low solubility in water (1.5 g/L at 298 K), [130] and second, the formate species have high solubility in water (945 g/L at 298 K).[131] In addition, the formate species have high proclivity for being adsorbed on oxide semiconductor surfaces[132] and are easily oxidized by the photogenerated holes in the oxide.

In both cases (Figures 3.29a and b), the photoreaction is initiated by photooxidation of the respective carboxylic acid (photo-Kolbe reaction) on the oxide photocatalyst surface. The $^{\bullet}OH$ radicals photogenerated from the initial hole (h^{+}_{vb}) attack on the surface adsorbed water molecules cause carboxylic acid oxidation rather than O_2 generation from photooxidation of water. H_2 photogeneration on Pt sites occurs in both cases although initial Pt modification of the oxide surface has different consequences. In the case of formic acid as the electron donor, H_2 photogeneration is completely quenched in the absence of Pt while for acetic acid (Figure 3.29b), the extent of methane photogeneration is influenced by the presence of Pt islands on the oxide surface.

Rationalization of the above observations can be done by considering the radical intermediates that are generated on initial photo-oxidation of the organic acid. In the case of formic acid oxidation, the intermediate photogenerated $HCOO^{\bullet}$ radical injects an electron into the $AgBiW_2O_8$ conduction band via the well-established current–doubling mechanism (shown in Figure 3.30a).[133] The net result is formation of hydrogen atoms (on Pt sites followed by subsequent H_2 formation) and CO_2. No poisoning of the Pt sites was observed attesting to the site specificity visualized for CO_2 reduction and proton reduction on the bare semiconductor surface and Pt islands respectively.

In the second case for acetic acid, the corresponding $H3CCOO^{\bullet}$ photogenerated radical (formed from initial hole attack on acetate) rapidly decomposes to $H_3C^{\bullet} + CO_2$, and then the $H_3C^{\bullet}$ radicals react with the hydrogen atoms stored on Pt islands to ultimately get converted into CH_4

(Figure 3.30b). Absence of the Pt sites inhibits the surface reaction involving the methyl radicals and hydrogen atoms. Figure 3.30 summarizes the mechanistic paths for the photocatalytic Kolbe reaction plus other reactions occurring on irradiation of Pt-modified SCS-$AgBiW_2O_8$ nanoparticles in contact with HCOOH (Figure 3.30a) and H_3CCOOH (Figure 3.30b) respectively.

Rate constants of the reactions associated with the photogenerated electrons are indicated as k(x) (with x = 1 to 4). The reaction product profiles are consistent with an ordering of these rate constants: k(1) > k(2) ~ k(4) > k(3). The very low amount of H_2 formed in the case of acetic acid is consistent with k(1) > k(4) which means that the photoelectrons are mainly consumed in the generation of CH_4 from the methyl radical. Importantly no C_2H_6 was found in our experiments indicating that the conduction band electrons are transferred to $H_3C^{\bullet}$ thus cancelling out the radical-radical coupling. The uptake of e^-_{cb} from Pt-modified SCS-$AgBiW_2O_8$ is much higher by $H_3C^{\bullet}$ than by CO_2 (k(1) > k(3)) and therefore no CO is observed in the data for CH_3COOH (Figure 3.29b). Further, k(2) > k(3) which would be consistent with the ratio, H_2 : CO ~ 3 : 1, measured for formic acid as the electron donor.

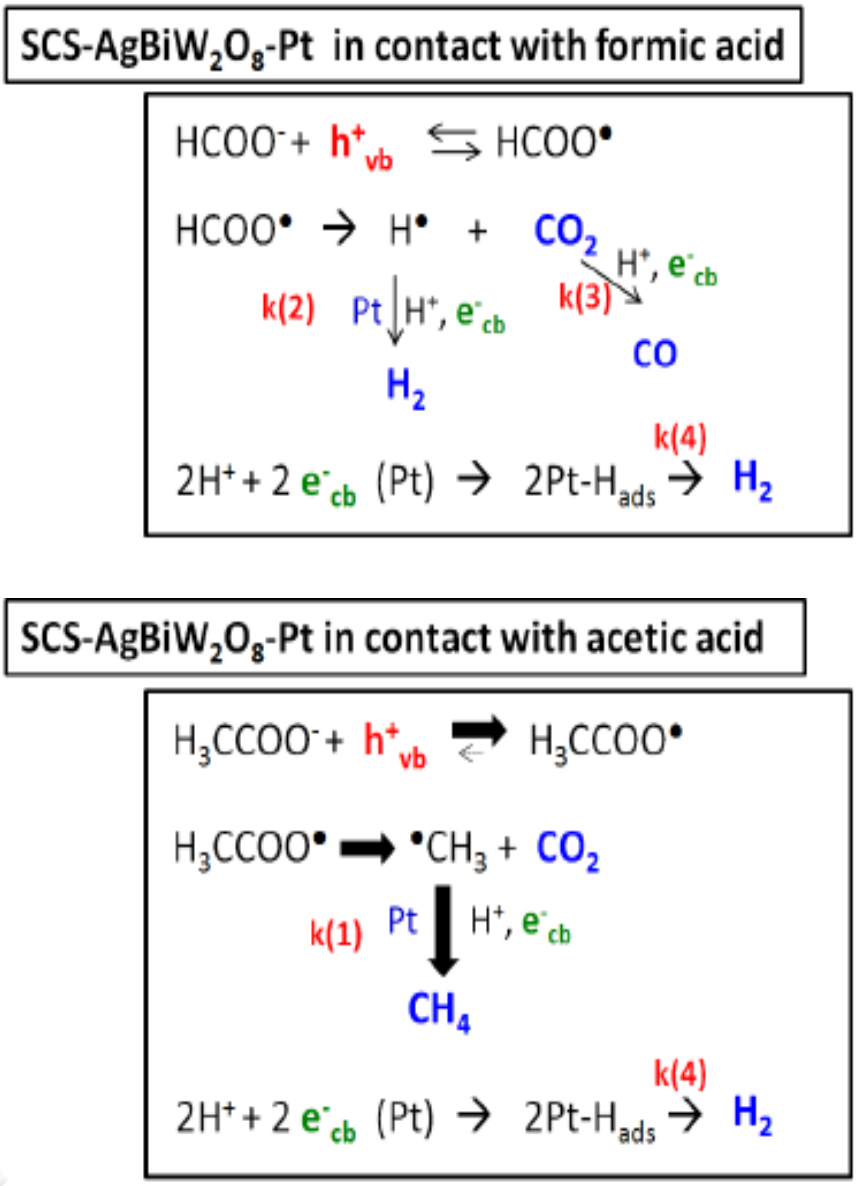

Figure 3.30 Mechanistic pathways for the photocatalytic Kolbe reaction along with other reactions occurring on irradiation of Pt-modified SCS-$AgBiW_2O_8$ nanoparticles in contact with (a) formic acid and (b) acetic acid respectively.

In the absence of irradiation, the products and pathways of electrochemical oxidation of the two carboxylic acids (Kolbe reaction) depend on the anode material.[134] On a platinum electrode and with simple carboxylic acids such as H_3CCOOH, the Kolbe reaction (performed by galvanostatic electrolysis) involves the formation of hydrocarbons through a free radical sequence as follows[134]: ($H_3CCOO^- \rightarrow H_3CCOO^\bullet \rightarrow H_3C^\bullet + CO_2$, $2\ H_3C^\bullet \rightarrow C_2H_6$). Thus, the *normal Kolbe reaction* involves radical-radical coupling ($H_3C^\bullet$ coupling) as the predominant mechanism at platinum anodes while an *abnormal Kolbe reaction* almost exclusively occurs at carbon electrodes either in organic or in aqueous media generating CH_3COOCH_3.[134] With α-substituted carboxylic acids, more complex mechanisms involving radicals and/or carbonium ion intermediates give rise to the formation of other products such as olefins, alcohols, ethers, and esters.[135]

Interesting contrasts have been reported in product evolution for similar electrode surfaces with and without illumination.[136-139] Ethane (C_2H_6) was observed as the dominant product on a TiO_2 *photoanode* in organic media (acetonitrile) with 0.1 M tetrabutyl ammonium perchlorate as supporting electrolyte and 0.08 M of tetrabutyl ammonium acetate as source of acetate ions.[136] On the other hand, methane (rather than ethane) was reported on photoirradiated TiO_2-Pt nanoparticles in contact with acetic acid very similar to the observations in this study (Figure 3.29b). Methyl radical coupling (leading to ethane) is clearly favored on the massive electrode surface because of the site proximity effect.

Quantum yields for the formation of syngas (H_2+CO) and CO_2 in the formic acid solution were as follows: H_2 = 3.0 %, CO = 0.8 % and CO_2 = 4.5 %. [Chemical actinometry using an aqueous solution of 6 mM $K_3Fe(C_2O_4)_3.3H_2O$ in 1.0 N H_2SO_4 [140] provided a calculated photon flux of 3.2×10^{-2} moles and thus the reported quantum yield was calculated as the percent ratio of the number of moles of product divided by the moles of photons.] The H_2:CO_2 ratio was seen to be ~ 1:1.5 for reaction times up to 1 hr, whereas it reached a ratio of 1:2.8 for reaction times higher than 3 h. Product amounts at the end of the photocatalytic runs were as follows: $H_2 = 1.0 \times 10^{-2}$ mol/g.L, CO = 3.0×10^{-3} mol/g.L and $CO_2 = 2.8 \times 10^{-2}$ mol/g.L. These data are

reported as the number of moles of product divided by the photocatalyst mass and liquid volume in the photoreactor. The turnover number (TON = molar amount of reacted electrons divided by molar amount of catalyst) for the photocatalytic formation of H_2 + CO (using a factor 2 to represent the number of electrons per H_2 and CO respectively) on the Pt-modified SCS–$AgBiW_2O_8$ nanoparticles reached a value of ca. 4.3 after 4 h irradiation, producing 1.0 mmol of H_2 and 0.3 mmol of CO.

For the photocatalytic synthesis of CH_4 from acetic acid on Pt-modified SCS–$AgBiW_2O_8$ nanoparticles, the amount of gases generated at the end of the runs was as follows: CH_4 = 1.45 x 10^{-2} mol/g.L, CO_2 = 0.92 x 10^{-2} mol/g.L and H_2 = 0.24 x 10^{-2} mol/g.L, with the quantum yields as follows: CH_4 = 1.7 %, CO_2 = 1.2 % and H_2 = 0.3 %. The experimental CH_4:CO_2 ratio was found to be ~ 1.5:1 at reaction times up to 1 h, increasing slightly afterwards to 1.6:1.

CHAPTER 4

SUMMARY AND CONCLUSIONS

There has been an exponential increase in the research for developing new oxide photocatalysts for solar energy and environmental remediation applications, especially during the past decade. Combined with the advances in nanotechnology, the activity and applications of oxide photocatalysts have increased substantially, ranging from air and water purification, solar induced hydrogen production, self cleaning devices to microbial disinfection etc.

As part of the search for new oxide photocatalysts, the present dissertation focused on preparing bismuth based oxide photocatalysts of the Bi-M-O (M = V or W) family using 'mild' synthesis routes (electrodeposition and combustion synthesis)[2,10-15,87] and evaluating their efficacy for solar energy and environmental remediation applications. These preparation methods are simple, less time consuming, and more importantly, reduce the energy payback time of the prepared materials. Two such oxides namely, bismuth vanadate ($BiVO_4$) and silver bismuth tungstate ($AgBiW_2O_8$), were prepared during the course of this research.

The photocatalytic activity of the oxide photocatalysts was assessed by studying the degradation of methyl orange (MO) dye under visible light irradiation. Both the compounds showed superior photocatalytic activity when compared to the respective benchmark samples. Another crucial aspect of this study was to test the ability of the oxides to photocatalytically generate fuels from aqueous solutions of carboxylic acids. The ability of photocatalysts to produce fuels from sources such as CO_2 is beneficial from an energy perspective. This aspect was the basis for studying the syngas photogeneration capacity of $AgBiW_2O_8$ in the present work.

Part I of the study focused on preparing $BiVO_4$ by solution combustion synthesis and its photocatalytic activity was assessed using MO degradation. The effect of the vanadium precursor on the photocatalytic activity was probed for the first time in this study, and it was found

that the choice of vanadium precursor influenced the photocatalytic performance of $BiVO_4$. In addition, $BiVO_4$ photoelectrodes were also prepared on a Pt substrate by electrodepostion.

Part II of the study comprised of preparing $AgBiW_2O_8$ photocatalyst by solution combustion synthesis. $AgBiW_2O_8$ was prepared for the first time using the combustion synthesis technique in this study. The combustion–synthesized sample showed superior MO photodegradation ability relative to a benchmark sample prepared by solid state reaction, which is explained based on the morphological differences in the samples.

Another important aspect of this work was to assess syngas (H_2 + CO) photogeneration capacity of SCS-$AgBiW_2O_8$ from an aqueous solution of formic acid, as well as methane (CH_4) photogeneration from an aqueous solution of acetic acid. Pt was photodeposited on the oxide surface and it was observed that H_2 and CH_4 photogeneration capacities were affected by the Pt loading. The reaction mechanisms were found to be different in both the cases.

Overall, the focus of the research was to prepare oxide semiconductors using ‘mild’ synthesis methods and to evaluate their potential for solar energy and environmental remediation applications. The results were promising in that the photocatalytic activity was superior to the respective benchmark samples. Further studies aimed at increasing the sensitivity of the materials towards visible light need to be carried out to enhance the use of these materials under solar irradiation.

REFERENCES

(1) Rajeshwar, K. *Journal of Applied Electrochemistry* **2007**, *37*, 765-787.

(2) Rajeshwar, K.; de Tacconi, N. R. *Chemical Society Reviews* **2009**, *38*, 1984-1998.

(3) Linsebigler, A. L.; Lu, G. Q.; Yates, J. T. *Chemical Reviews* **1995**, *95*, 735-758.

(4) http://www.lbl.gov/Science-Articles/Archive/MSD-full-spectrum-solar-cell.html.(accessed 07/2011).

(5) Bard, A. J., Faulkner, L. R. *Electrochemical methods: fundamentals and applications*; 2nd Ed ed.; John Wiley & Sons: NJ, 2001.

(6) Zhang, H. J.; Chen, G. H.; Bahnemann, D. W. *Journal of Materials Chemistry* **2009**, *19*, 5089-5121.

(7) Kudo, A.; Miseki, Y. *Chemical Society Reviews* **2009**, *38*, 253-278.

(8) Sohrabi, M.; Tavakoli, A.; Kargari, A. *Chemical Papers* **2007**, *61*, 151-170.

(9) Lincot, D. *Thin Solid Films* **2005**, *487*, 40-48.

(10) Schlesinger, T. E. R., K.; de Tacconi, N. R. *Electrodeposition of Semiconductors*; 5th ed.; Springer: New York, 2010.

(11) Kamath, P. V.; Therese, G. H. A. *Chemistry of Materials* **2000**, *12*, 1195-1204.

(12) Simka, W.; Puszczyk, D.; Nawrat, G. *Electrochimica Acta* **2009**, *54*, 5307-5319.

(13) Patil, K. C., Hegde, M.S., Rattan, Tanu, Aruna, S.T. *Chemistry of Nanocrystalline Oxide Materials: Combustion Synthesis, Properties and Applications*; World Scientific Publishing Pte. Ltd.: Singapore, 2008.

(14) Aruna, S. T.; Mukasyan, A. S. *Current Opinion in Solid State & Materials Science* **2008**, *12*, 44-50.

(15) Mukasyan, A. S.; Epstein, P.; Dinka, P. *Proceedings of the Combustion Institute* **2007**, *31*, 1789-1795.

(16) Moore, J. J.; Feng, H. J. *Progress in Materials Science* **1995**, *39*, 243-273.

(17) Merzhanov, A. G. *Journal of Materials Chemistry* **2004**, *14*, 1779-1786.

(18) Jain, S. R.; Adiga, K. C.; Verneker, V. R. P. *Combustion and Flame* **1981**, *40*, 71-79.

(19) Smith, H. M. *High Performance Pigments*; Wiley - VCH: Weinheim, Germany, 2002.

(20) Rajeshwar, K., McConnell, R., Licht, S. (Eds.) *Solar Hydrogen Generation*; Springer: New York, 2008.

(21) Rajeshwar, K., Ibanez, J.G. *Environmental Electrochemistry*; Academic Press: San Diego, 1997.

(22) Qurashi, M. M., Barnes, W.H. *Am.Mineralogist* **1952**, *37*, 423.

(23) Sleight, A. W.; Chen, H. Y.; Ferretti, A.; Cox, D. E. *Materials Research Bulletin* **1979**, *14*, 1571-1581.

(24) Bhattacharya, A. K.; Mallick, K. K.; Hartridge, A. *Materials Letters* **1997**, *30*, 7-13.

(25) Walsh, A.; Yan, Y.; Huda, M. N.; Al-Jassim, M. M.; Wei, S. H. *Chemistry of Materials* **2009**, *21*, 547-551.

(26) Tokunaga, S.; Kato, H.; Kudo, A. *Chemistry of Materials* **2001**, *13*, 4624-4628.

(27) Kudo, A.; Omori, K.; Kato, H. *Journal of the American Chemical Society* **1999**, *121*, 11459-11467.

(28) Kudo, A.; Ueda, K.; Kato, H.; Mikami, I. *Catalysis Letters* **1998**, *53*, 229-230.

(29) Oshikiri, M.; Boero, M.; Ye, J. H.; Zou, Z. G.; Kido, G. *Journal of Chemical Physics* **2002**, *117*, 7313-7318.

(30) Kohtani, S.; Makino, S.; Kudo, A.; Tokumura, K.; Ishigaki, Y.; Matsunaga, T.; Nikaido, O.; Hayakawa, K.; Nakagaki, R. *Chemistry Letters* **2002**, 660-661.

(31) Liu, J. B.; Wang, H.; Wang, S.; Yan, H. *Materials Science and Engineering B-Solid State Materials for Advanced Technology* **2003**, *104*, 36-39.

(32) Kohtani, S.; Koshiko, M.; Kudo, A.; Tokumura, K.; Ishigaki, Y.; Toriba, A.; Hayakawa, K.; Nakagaki, R. *Applied Catalysis B-Environmental* **2003**, *46*, 573-586.

(33) Kohtani, S.; Hiro, J.; Yamamoto, N.; Kudo, A.; Tokumura, K.; Nakagaki, R. *Catalysis Communications* **2005**, *6*, 185-189.

(34) Liu, H. M.; Nakamura, R.; Nakato, Y. *Journal of the Electrochemical Society* **2005**, *152*, G856-G861.

(35) Zhang, C.; Zhu, Y. F. *Chemistry of Materials* **2005**, *17*, 3537-3545.

(36) Gotic, M.; Music, S.; Ivanda, M.; Soufek, M.; Popovic, S. *Journal of Molecular Structure* **2005**, *744*, 535-540.

(37) Zhou, L.; Wang, W. Z.; Liu, S. W.; Zhang, L. S.; Xu, H. L.; Zhu, W. *Journal of Molecular Catalysis a-Chemical* **2006**, *252*, 120-124.

(38) Yu, J. Q.; Kudo, A. *Advanced Functional Materials* **2006**, *16*, 2163-2169.

(39) Zhang, L.; Chen, D. R.; Jiao, X. L. *Journal of Physical Chemistry B* **2006**, *110*, 2668-2673.

(40) Long, M.; Cai, W. M.; Cai, J.; Zhou, B. X.; Chai, X. Y.; Wu, Y. H. *Journal of Physical Chemistry B* **2006**, *110*, 20211-20216.

(41) Sayama, K.; Nomura, A.; Arai, T.; Sugita, T.; Abe, R.; Yanagida, M.; Oi, T.; Iwasaki, Y.; Abe, Y.; Sugihara, H. *Journal of Physical Chemistry B* **2006**, *110*, 11352-11360.

(42) Xie, B. P.; Zhang, H. X.; Cai, P. X.; Qiu, R. L.; Xiong, Y. *Chemosphere* **2006**, *63*, 956-963.

(43) Zhang, X.; Ai, Z. H.; Jia, F. L.; Zhang, L. Z.; Fan, X. X.; Zou, Z. G. *Materials Chemistry and Physics* **2007**, *103*, 162-167.

(44) Chen, X. Y.; Zhang, Z. J.; Lee, S. W. *Journal of Solid State Chemistry* **2008**, *181*, 166-174.

(45) Long, M. C.; Beranek, R.; Cai, W. M.; Kisch, H. *Electrochimica Acta* **2008**, *53*, 4621-4626.

(46) Chatchai, P.; Murakami, Y.; Kishioka, S. Y.; Nosaka, A. Y.; Nosaka, Y. *Electrochemical and Solid State Letters* **2008**, *11*, H160-H163.

(47) Ge, L. *Journal of Molecular Catalysis a-Chemical* **2008**, *282*, 62-66.

(48) Jiang, H. Q.; Endo, H.; Natori, H.; Nagai, M.; Kobayashi, K. *Journal of the European Ceramic Society* **2008**, *28*, 2955-2962.

(49) Strobel, R.; Metz, H. J.; Pratsinis, S. E. *Chemistry of Materials* **2008**, *20*, 6346-6351.

(50) Zhao, Y.; Xie, Y.; Zhu, X.; Yan, S.; Wang, S. X. *Chemistry-a European Journal* **2008**, *14*, 1601-1606.

(51) Zhang, X. F.; Chen, S.; Quan, X.; Zhao, H. M. *Separation and Purification Technology* **2009**, *64*, 309-313.

(52) Chatchai, P.; Murakami, Y.; Kishioka, S. Y.; Nosaka, A. Y.; Nosaka, Y. *Electrochimica Acta* **2009**, *54*, 1147-1152.

(53) Zhang, A. P.; Zhang, J. Z. *Spectrochimica Acta Part a-Molecular and Biomolecular Spectroscopy* **2009**, *73*, 336-341.

(54) Yu, J. Q.; Zhang, Y.; Kudo, A. *Journal of Solid State Chemistry* **2009**, *182*, 223-228.

(55) Yin, W. Z.; Wang, W. Z.; Shang, M.; Zhang, L.; Ren, J. *Chemistry Letters* **2009**, *38*, 422-423.

(56) Dunkle, S. S.; Helmich, R. J.; Suslick, K. S. *Journal of Physical Chemistry C* **2009**, *113*, 11980-11983.

(57) Sun, S. M.; Wang, W. Z.; Zhou, L.; Xu, H. L. *Industrial & Engineering Chemistry Research* **2009**, *48*, 1735-1739.

(58) Li, H. B.; Liu, G. C.; Duan, X. C. *Materials Chemistry and Physics* **2009**, *115*, 9-13.

(59) Ke, D. N.; Peng, T. Y.; Ma, L.; Cai, P.; Dai, K. *Inorganic Chemistry* **2009**, *48*, 4685-4691.

(60) Wang, F. X.; Shao, M. W.; Cheng, L.; Hua, J.; Wei, X. W. *Materials Research Bulletin* **2009**, *44*, 1687-1691.

(61) Sun, Y. F.; Wu, C. Z.; Long, R.; Cui, Y.; Zhang, S. D.; Xie, Y. *Chemical Communications* **2009**, 4542-4544.

(62) Shang, M.; Wang, W. Z.; Sun, S. M.; Ren, J.; Zhou, L.; Zhang, L. *Journal of Physical Chemistry C* **2009**, *113*, 20228-20233.

(63) Zhang, A. P.; Zhang, J. Z. *Materials Letters* **2009**, *63*, 1939-1942.

(64) Dong, F. Q.; Wu, Q. S.; Ma, J.; Chen, Y. J. *Physica Status Solidi a-Applications and Materials Science* **2009**, *206*, 59-63.

(65) Zhang, A. P.; Zhang, J. Z.; Cui, N. Y.; Tie, X. Y.; An, Y. W.; Li, L. J. *Journal of Molecular Catalysis a-Chemical* **2009**, *304*, 28-32.

(66) Ma, D. K.; Wang, S.; Cai, P.; Jiang, J. L.; Yang, D. P.; Huang, S. M. *Chemistry Letters* **2009**, *38*, 962-963.

(67) Zhang, X. F.; Zhang, Y. B.; Quan, X.; Chen, S. *Journal of Hazardous Materials* **2009**, *167*, 911-914.

(68) Yin, W. Z.; Wang, W. Z.; Zhou, L.; Sun, S. M.; Zhang, L. *Journal of Hazardous Materials* **2010**, *173*, 194-199.

(69) Yang, T.; Xia, D. G. *Journal of Crystal Growth* **2009**, *311*, 4505-4509.

(70) Sayama, K.; Wang, N. N.; Miseki, Y.; Kusama, H.; Onozawa-Komatsuzaki, N.; Sugihara, H. *Chemistry Letters* **2010**, *39*, 17-19.

(71) Dall'Antonia, L. H.; de Tacconi, N. R.; Chanmanee, W.; Timmaji, H.; Myung, N.; Rajeshwar, K. *Electrochemical and Solid State Letters* **2010**, *13*, D29-D32.

(72) Jiang, H. Q.; Nagai, M.; Kobayashi, K. *Journal of Alloys and Compounds* **2009**, *479*, 821-827.

(73) Lee, D. K.; Cho, I. S.; Lee, S.; Bae, S. T.; Noh, J. H.; Kim, D. W.; Hong, K. S. *Materials Chemistry and Physics* **2010**, *119*, 106-111.

(74) Roy, B.; Fuierer, P. A. *Journal of Materials Research* **2009**, *24*, 3078-3086.

(75) Timmaji, H. K., Chanmanee, W., de Tacconi, N.R., Rajeshwar, K *Journal of Advanced Oxidation Technologies* **2011**, *14*, 93-105.

(76) Tang, J. W.; Ye, J. H. *Journal of Materials Chemistry* **2005**, *15*, 4246-4251.

(77) Shi, H. F.; Li, Z. S.; Ye, J. H.; Zou, Z. G. *Journal of Physics D-Applied Physics* **2010**, *43*, 085402-1-085402-7.

(78) Shi, H. F.; Huang, X. L.; Tian, H. M.; Lv, J.; Li, Z. S.; Ye, J. H.; Zou, Z. G. *Journal of Physics D-Applied Physics* **2009**, *42*, -.

(79) Kato, H.; Matsudo, N.; Kudo, A. *Chemistry Letters* **2004**, *33*, 1216-1217.

(80) Tang, J. W.; Zou, Z. G.; Ye, J. H. *Angewandte Chemie-International Edition* **2004**, *43*, 4463-4466.

(81) Zhang, L. S.; Wong, K. H.; Chen, Z. G.; Yu, J. C.; Zhao, J. C.; Hu, C.; Chan, C. Y.; Wong, P. K. *Applied Catalysis a-General* **2009**, *363*, 221-229.

(82) Ouyang, S.; Li, Z.; Ouyang, Z.; Yu, T.; Ye, J.; Zou, Z. *The Journal of Physical Chemistry C* **2008**, *112*, 3134-3141.

(83) Chueh, W. C.; Falter, C.; Abbott, M.; Scipio, D.; Furler, P.; Haile, S. M.; Steinfeld, A. *Science* **2010**, *330*, 1797-1801.

(84) Lehn, J. M.; Ziessel, R. *Proceedings of the National Academy of Sciences of the United States of America-Physical Sciences* **1982**, *79*, 701-704.

(85) Ziessel, R.; Hawecker, J.; Lehn, J. M. *Helvetica Chimica Acta* **1986**, *69*, 1065-1084.

(86) de Tacconi, N. R.; Chenthamarakshan, C. R.; Rajeshwar, K.; Lin, W. Y.; Carlson, T. F.; Nikiel, L.; Wampler, W. A.; Sambandam, S.; Ramani, V. *Journal of the Electrochemical Society* **2008**, *155*, B1102-B1109.

(87) Dean, J. A. *Analytical Chemistry Handbook*; McGraw-Hill, Inc.: New York, 1995.

(88) Cullity, B. D. *Elements of X-Ray Diffraction*; Addison-Wesley: Reading, MA, 1967.

(89) Pankove, J. L. *Optical Processes in Semiconductors*; Prentice Hall: Englewood, Cliffs, New Jersey, 1971.

(90) Finlayson, A. P.; Tsaneva, V. N.; Lyons, L.; Clark, M.; Glowacki, B. A. *Physica Status Solidi a-Applications and Materials Science* **2006**, *203*, 327-335.

(91) Hawecker, J.; Lehn, J. M.; Ziessel, R. *Helvetica Chimica Acta* **1986**, *69*, 1990-2012.

(92) Lin, W. Y.; Wei, C.; Rajeshwar, K. *Journal of the Electrochemical Society* **1993**, *140*, 2477-2482.

(93) Chenthamarakshan, C. R.; Rajeshwar, K. *Langmuir* **2000**, *16*, 2715-2721.

(94) Perdew, J. P.; Chevary, J. A.; Vosko, S. H.; Jackson, K. A.; Pederson, M. R.; Singh, D. J.; Fiolhais, C. *Physical Review B* **1992**, *46*, 6671-6687.

(95) Perdew, J. P.; Burke, K.; Ernzerhof, M. *Physical Review Letters* **1996**, *77*, 3865-3868.

(96) Kresse, G.; Furthmuller, J. *Physical Review B* **1996**, *54*, 11169-11186.

(97) Kresse, G.; Furthmuller, J. *Computational Materials Science* **1996**, *6*, 15-50.

(98) Kresse, G.; Joubert, D. *Physical Review B* **1999**, *59*, 1758-1775.

(99) Blochl, P. E. *Physical Review B* **1994**, *50*, 17953-17979.

(100) Blochl, P. E.; Jepsen, O.; Andersen, O. K. *Physical Review B* **1994**, *49*, 16223-16233.

(101) de Tacconi, N. R.; Rajeshwar, K.; Chanmanee, W.; Valluri, V.; Wampler, W. A.; Lin, W. Y.; Nikiel, L. *Journal of the Electrochemical Society* **2010**, *157*, B147-B153.

(102) Shimodaira, Y.; Kato, H.; Kobayashi, H.; Kudo, A. *Journal of Physical Chemistry B* **2006**, *110*, 17790-17797.

(103) Jeong, H. Y.; Lee, J. H.; Hayes, K. F. *Geochimica Et Cosmochimica Acta* **2008**, *72*, 493-505.

(104) Harris, D. C. *Quantitative Chemical Analysis*; 7th ed.; W.H. Freeman and Co.: New York, 2007.

(105) Farmer, V. C. e. *Mineralogical Society Monograph 4: The Infrared Spectra of Minerals*; Mineralogical Society: London, England, 1974.

(106) Frost, R. L.; Henry, D. A.; Weier, M. L.; Martens, W. *Journal of Raman Spectroscopy* **2006**, *37*, 722-732.

(107) Fomichev, V. V.; Ukrainskaya, P. I.; Ilyin, T. M. *Spectrochimica Acta Part a-Molecular and Biomolecular Spectroscopy* **1997**, *53*, 1833-1837.

(108) Ouyang, S.; Ye, J. *Journal of the American Chemical Society* **2011**, *133*, 7757-7763.

(109) Su, J.; Zou, X.-X.; Li, G.-D.; Wei, X.; Yan, C.; Wang, Y.-N.; Zhao, J.; Zhou, L.-J.; Chen, J.-S. *The Journal of Physical Chemistry C* **2011**, *115*, 8064-8071.

(110) Vinke, I. C.; Diepgrond, J.; Boukamp, B. A.; Devries, K. J.; Burggraaf, A. J. *Solid State Ionics* **1992**, *57*, 83-89.

(111) deTorresi, S. I. C.; Carlos, I. A. *Journal of Electroanalytical Chemistry* **1996**, *414*, 11-16.

(112) Hepel, M.; Bruckenstein, S.; Kanige, K. *Journal of the Chemical Society, Faraday Transactions* **1993**, *89*, 251-254.

(113) Wood, P.; Glasser, F. R. *Ceramics International* **2004**, *30*, 875-882.

(114) Wagner, C. D., Riggs, W.M., Davis, L.E., Moulder, J.F., and Mullenberg, G.E. *Handbook of X-ray Photoelectron Spectroscopy*; Perkin-Elmer Corp: Eden Prairie, MN, 1979.

(115) Andersson, S. L. T. *Journal of the Chemical Society, Faraday Transactions 1: Physical Chemistry in Condensed Phases* **1979**, *75*, 1356-1370.

(116) Azimirad, R.; Naseri, N.; Akhavan, O.; Moshfegh, A. Z. *Journal of Physics D-Applied Physics* **2007**, *40*, 1134-1137.

(117) Luo, H. M.; Mueller, A. H.; McCleskey, T. M.; Burrell, A. K.; Bauer, E.; Jia, Q. X. *Journal of Physical Chemistry C* **2008**, *112*, 6099-6102.

(118) Butler, M. A. *Journal of Applied Physics* **1977**, *48*, 1914-1920.

(119) Gartner, W. W. *Physical Review* **1959**, *116*, 84.

(120) Stoltzfus, M. W.; Woodward, P. M.; Seshadri, R.; Klepeis, J. H.; Bursten, B. *Inorganic Chemistry* **2007**, *46*, 3839-3850.

(121) Klevtsov, P. V.; Klevtsova, R. F. *Journal of Structural Chemistry* **1977**, *18*, 339-355.

(122) Ishii, K.; Morita, N.; Nakayama, H.; Tsunekawa, S.; Fukuda, T. *Physica Status Solidi a-Applied Research* **1989**, *112*, 207-214.

(123) David, W. I. F. *Materials Research Bulletin* **1983**, *18*, 749-756.

(124) Abraham, Y.; Holzwarth, N. A. W.; Williams, R. T. *Physical Review B* **2000**, *62*, 1733-1741.

(125) Sleight, A. W. *Acta Crystallographica B* **1972**, *B 28*, 2899-2902.

(126) Huda, M. N.; Yan, Y. F.; Moon, C. Y.; Wei, S. H.; Al-Jassim, M. M. *Physical Review B* **2008**, *77*, 195102-1-195102-13.

(127) Li, G. S.; Zhang, D. Q.; Yu, J. C.; Leung, M. K. H. *Environmental Science & Technology* **2010**, *44*, 4276-4281.

(128) Cantalini, C.; Sun, H. T.; Faccio, M.; Pelino, M.; Santucci, S.; Lozzi, L.; Passacantando, M. *Sensors and Actuators B-Chemical* **1996**, *31*, 81-87.

(129) Leftheriotis, G.; Papaefthimiou, S.; Yianoulis, P.; Siokou, A. *Thin Solid Films* **2001**, *384*, 298-306.

(130) Palmer, D. A.; Vaneldik, R. *Chemical Reviews* **1983**, *83*, 651-731.

(131) *CRC Handbook of Chemistry and Physics*; 82nd Ed ed.; CRC Press: Boca Raton, FL, 2001-2002.

(132) Chenthamarakshan, C. R.; Rajeshwar, K. *Electrochemistry Communications* **2000**, *2*, 527-530.

(133) Morrison, S. R. *The Chemical Physics of Surfaces*; Plenum Press: New York and London, 1977.

(134) Koehl, W. J. *Journal of the American Chemical Society* **1964**, *86*, 4686-4690.

(135) Weedon, B. C. I. *Advances in Organic Chemistry*; Interscience Publishers Inc.: New York, 1960; Vol. 1.

(136) Kraeutler, B.; Bard, A. J. *Journal of the American Chemical Society* **1977**, *99*, 7729-7731.

(137) Kraeutler, B.; Jaeger, C. D.; Bard, A. J. *Journal of the American Chemical Society* **1978**, *100*, 4903-4905.

(138) Kraeutler, B.; Bard, A. J. *Journal of the American Chemical Society* **1978**, *100*, 2239-2240.

(139) Kraeutler, B.; Bard, A. J. *Journal of the American Chemical Society* **1978**, *100*, 5985-5992.

(140) Murov, S. L., Carmichael, Ian., Hug, Gordon L. *Handbook of Photochemistry*; 2nd Ed., ed.; Marcel Dekker Inc: New York, 1993.

BIOGRAPHICAL INFORMATION

Hari Krishna Timmaji received his Ph.D in Earth and Environmental Sciences from The University of Texas at Arlington in December 2011. He obtained his Master of Science and Technology (with specialization in Environmental Chemistry) degree from Jawaharlal Nehru Technological University, Hyderabad, India in August 1997, and Bachelor of Science degree from Osmania University, Hyderabad, India in April 1994.